College of Engineering, Mathematics and Physical Sciences

Novel Molten Salt Synthesis of ZrB_2 and ZrC powders and Molten Salt Synthesis of Novel TiC

Submitted by Matthana Khangkhamano to the University of Exeter as a thesis for the degree of Doctor of Philosophy in Engineering, October 2014

Supervised by: Prof. Shaowei Zhang and Dr. Yongde Xia

(Signature) .....

Preface

This thesis is submitted for the degree of Doctor of Philosophy at the University of Exeter. The purpose of this thesis is to introduce and illustrate an alternative approach on fabrication of novel boride and carbide materials in various morphologies using molten salt synthesis (MSS) technique under the supervision of Prof.Shaowei Zhang and Dr.Yongde Xia in the College of Engineering, Mathematics and Physical Sciences at the University of Exeter. I certify that this work has not been submitted in whole or any part for other degrees at this or any other institutes.

MatthanaKhangkhamano
University of Exeter
September 2014

Publication

S. Zhang, M. Khangkhamano, H. Zhang, and H. A. Yeprem, "Novel synthesis of ZrB_2 powder via molten-salt-mediated magnesiothermic reduction", *Journal of the American Ceramic Society*, vol. 97, no. 6, pp. 1686-1688, 2014.

Abstract

Pure submicron-sized zirconium diboride (ZrB_2) powder was synthesised via a molten salt mediated reduction route using ZrO_2, $Na_2B_4O_7$, and Mg powders as the starting raw materials and $MgCl_2$ as the reaction medium. By using appropriately excessive amounts of Mg and $Na_2B_4O_7$ to compensate for their evaporation losses, ZrO_2 can be completely converted into ZrB_2 after 3 h of firing at 1200 °C. This synthesis temperature is 100-500 °C lower than that of other conventional synthesis techniques. In addition, the formation of undesirable $Mg_3B_2O_6$ can be effectively suppressed. To a large extent, the prepared ZrB_2 particles preserved the shapes and sizes of the original ZrO_2 particles, indicating a template growth mechanism for their formation in which ZrO_2 functions as the reaction template. Using this developed synthesis method, submicron-sized and nanosized zirconium carbide (ZrC) powders were synthesised in the reaction system of ZrO_2-Mg-carbon black using NaCl-KCl as the reaction medium. The synthesis temperatures were 950 and 850 °C for the former and the latter powder size, respectively, which are much lower temperatures than those used in most of the reported methods. Compared with the submicron-sized ZrO_2 powders, the finer ZrO_2 particles considerably enhanced the reaction rate and thus the completion of the reaction at a lower temperature. The resulting ZrC particles exhibited two different morphologies: one retained the shapes and sizes of the original ZrO_2, and the other retained those of the starting carbon black, suggesting that both ZrO_2 and carbon black had acted as reaction templates. In addition, the 2D-nanostructure of a non-layered structure material, titanium carbide (TiC), was fabricated. The novel TiC nanosheets (TNS) and TiC-coated graphite nanosheets (TCNS) were produced at 950 °C for 8 h and 900 °C for 5 h, respectively, in KCl molten salt using graphite nanosheets (GNS) as both a

carbon source and reaction templates. The produced TNS and TCNS retained the shapes, sizes and thickness of the original GNS to a high degree, indicating that the GNS had acted as the reaction template. For TCNS, a lower molar ratio of Ti/C required a lower synthesis temperature and/or a shorter holding time. This effective processing technique was also employed to produce TiC foams at 1050 °C for 4 h using carbon foam as the reaction template. This synthesis temperature is significantly lower than that (>1450 °C) used in most of the other techniques. The resultant pores were clear of any undesired phases such as impurities and/or membranes, and the cell-networks were free of surface cracks and holes. The cell-networks, pore sizes, and cell sizes of the synthesised foams were well defined by those of the original carbon foam, suggesting a template growth mechanism of the formation of the TiC foam.

Acknowledgements

I would like to express my sincere gratitude to the people who offered me greatly valuable assistance during my PhD study.

First of all, I am sincerely grateful to my supervisor Prof. Shaowei Zhang for his kind support, encouragement, advice and guidance throughout my research work to develop my confidence of being an academic. His valuable suggestions on both academic and personal levels have been priceless. I would also like to thank Prof. Yanqiu Zhu and the people in his research group for their kind support and assistance in all matters throughout my PhD time in Exeter. A special thanks to the people in my research group:Wei Xie, Jianke Ye, Yan Wen, Liangxu Lin, Juntong Huang, and Bao Ke for sharing the knowledge and experience in the experiment. Special thanks to Ian Watts, Dean Haylock, and Bev Lane for the technical support and help on my synthesis work. I also appreciate Ben G Palmer, Nik Reeves, Lesley Wears, Hong Chang, and Peng Zeng for their help on TGA/DTA, Raman spectroscopy, XRD, HRTEM and SEM training respectively.

I would especially like to thank Prof. Mark Rainforth, head of materials science and engineering department at the University of Sheffield for his kind assistance allowing me to use some facilities in his department to complete my experimental works.

A special thanks to my family, especially my parents and grandmother for their pure love, support, and encouragements all the time. I would also like to thank

all of my friends: Owen, Jinny, Putza, Kim, Tui, Pee Es, Pee Boom and Pom who always stood by my side and motivated me to strive towards my goal.

At the end, I would like to express appreciation to Royal Thai Government Scholarship, Thailand, for financial support and giving me this priceless experience in a particular of learning and living abroad.

Abbreviations

GNS	Graphite Nanosheets
TNS	TiCNanosheets
CB	Carbon Black
CF	Carbon Foam
MSS	Molten Salt Synthesis
SHS	Self-propagating High-temperature Synthesis
TGA	Thermogravimetric Analysis
DTA	Differential Thermal Analysis
XRD	X-Ray Diffraction
SEM	Scanning Electron Microscope
FESEM	Field Emission Gun Scanning Electron Microscope
TEM	Transmission Electron Microscopy
HRTEM	High Resolution Transmission Electron Microscopy
EDS	Energy Dispersive X-Ray Spectroscopy
CVD	Chemical Vapour Deposition

Table of Contents

List of Tables

List of Figures

Chapter One

Introduction

Transition metal diboride and carbide materials such as ZrB_2, ZrC and TiC, are currently under extensive investigation as structural and functional ceramics for a wide range of applications. Their potential applications can be attributed to their various remarkable properties. Zirconium diboride (ZrB_2) possesses, for example, high melting point, high hardness, high mechanical strength at room temperature and at high temperature, good electrical and thermal conductivities, excellent thermal shock resistance and oxidation resistance (at a temperature up to 2000 °C) and chemical resistance even in extreme environments [1-3]. These outstanding properties make ZrB_2 attractive in the fields involving ultra-high temperature and extreme environments, for instance, thermal protection materials used for hypersonic flights, atmospheric re-entry vehicles, rocket propulsion, furnace elements and refractory crucibles [4-6].

Zirconium carbide (ZrC) also possesses a range of excellent properties, e.g., high melting point, high solid-state phase stability, good wear and corrosion resistances, super resistance to fission-product attack, and good thermal and mechanical properties at elevated temperatures. Thanks to these excellent properties, ZrC could be potentially used as a structural and fission-product barrier coating material for high temperature gas-cooled reactor (HTGR) fuel particles to replace the currently used silicon carbide (SiC) [7-11]. Furthermore, ZrC is also used to make cutting tools and oxidation-resistant coatings on carbon substrates for aerospace applications such as nose tips and rocket nozzles in which the materials used are subjected to very severe environments and ultra-high temperatures (up to 3000 °C).

In addition to ZrC, another carbide, titanium carbide (TiC), also has outstanding properties, including high hardness and high resistance to corrosion and wear. Because of these good properties, it is extensively used as a high temperature ceramic, a coating material to improve hardness and the oxidation resistance of the substrate material, cutting tools and abrasives [12]. Furthermore, carbide materials are extensively applied as reinforcements in composites and a hardening phase of superalloys [13]. Their high thermal stability would retain the properties of the composites even at high temperature which is an important requirement for many important applications such as in aerospace industry.

To synthesise transition metal boride and carbide materials, a number of approaches have been reported and are still being investigated by many researchers, aiming to seek a more feasible one for commercial productions. Carbothermal reduction method is currently employed to commercially produce these materials. The resulting products, however, are coarse grains due to high synthesis temperature and long reaction time. To lower the synthesis

temperature, a mechanochemical alloying route is employed by the assistance of a high-energy ball mill, prior to heat treatment. Using this method, the product phase can be produced at a much lowered temperature or even at room temperature. The process, nevertheless, requires a prolonged milling time leading to energy and time consuming and increased contamination on the final products from the grinding/milling media (vial, balls and grinding medium). Another commonly used method applied to produced ceramic powders is self-propagating high temperature synthesis (SHS) with which the materials can be fabricated within a short time [14]. However, the final products are generally coarse grains having high concentration of defects due to rapid cooling rates. Sol-gel technique is also used to produce fine (nanosized) , however, it requires expensive precursors and prolonged reaction time.

Investigating of and searching for an alternative method is therefore essential to improve those drawbacks suffered by the curent techniques. In this thesis, a low cost, low temperature and straightforward technique, molten salt synthesis (MSS), has been developed to fabricate boride and carbide materials in various forms (submicronsized and nanosized powders, nanosheets, coatings on 2D-nanostructure, and foams with 3D-interconnected networks), aiming to largely reduce the processing temperature, well control the morphologies, and achieve high purity and good dispersion of the final products.

One of the important mechanisms of MSS, the so-called template growth mechanism, was used to produce a novel 2D-nanostructured TiC. Transition metal carbides are non-layered structure materials. Graphite, on the other hand, is composed of graphene layers bonded together by a weak van der Waals force. Graphene layers in graphite can be exfoliated readily via, for instance, mechanical cleavage and chemical techniques [15-17] so as to produce graphene.

However, the work on carbide materials in the form of 2D-nanosheet is very limited due to the difficulty in exfoliating non-layered carbide materials, although other forms of carbides (such as powders, fibres, whiskers and rods) are widely available. In the present work, TiC nanosheets (TNS) and TiC coatings on graphite nanosheets were synthesised via MSS using graphite nanosheets (GNS) as reaction templates. The achievement of this study can be extended to further synthesise other 2D-nanostructured carbide materials.

With MSS technique, those advanced ceramic materials could be prepared at much lowered temperatures. Furthermore, their morphologies could be well controlable or tailored by choosing appropriate template materials, thanks to the template growth mechanism. In this work, apart from the fabrications of powders and nanosheets, 3D-interconnected networks (foam) of TiC were synthesised. The successful MSS of TiC foams at a temperature much lower than that used by most of the reported techniques, indicated that MSS could be a very promising alternative route to the production of a range of porous ceramic materials. This is because the currently available techniques used for fabricating such materials suffer from several disadvantages. For instance, the porous products produced by replica method normally contain a hole in the centre of the struts and cracking in them after burning-out of the polymer substrate, limiting their structural applications [18, 19]. On the other hand, when using an additive-gas forming agent technique, pore sizes of the products are difficult to be controlled, resulting in a wide pore size distribution [20]. Although this drawback could be overcome by starch consolidation casting technique which is generally employed for producing porous ceramics with a narrow pore size distribution, a high processing temperature still has to be used. The major problem suffered by the previously reported methods in the fabrication of porous ceramics is that a high firing temperature (>1450 °C) has to be used .

1.1 Objectives of Study

There are three main objectives of this work. The first is to optimise the synthesis conditions in order to prepare high purity ZrB_2 and ZrC powders, TiC nanosheets and TiC coated graphite nanosheets, and TiC foams. The second objective involves the application of modern techniques such as XRD, Raman spectroscopy, SEM, EDS, and TEM to characterise the resultant products, and, based on the results, understand the relevant reaction mechanisms. The final objective is to demonstrate the outstanding merits of using the MSS method, in comparison with other processing techniques, with foucs on the lowered synthesis temperature and outstandingly controllable shapes and sizes of the as-prepared products.

1.2 Thesis Outline

This thesis consists of eight chapters totally. Chapter one gives an overall introduction of the thesis, including the brief history of the materials studied and the objectives of the research. Chapter two is an comprehensive literature review, focused mainly on the materials studied and the processing techniques used to prepare them as well as the recent research on MSS. In chapter three, the facilities utilised for characterisation are described. Chapter four and five illustrate the experimental results obtained from the fabrications of ZrB_2 and ZrC powders, respectively, and the discussions on the reaction mechanisms and the effects of processing parameters on the product formations. Chapter six and seven demonstrate the results gained from fabrications of TiC nanosheets (TNS) and TiC-coated graphite nanosheets (TCNS), and TiC foams along with the discussions on the effects of processing parameters on the formations. Chapter eight ends with final conclusions and suggestions for future works.

Chapter Two

Literature Review

In this chapter, four main subdivisions: (i) transition metal carbides (ZrC and TiC) and zirconium diboride (ZrB_2); (ii) porous ceramics and typical synthesis methods; (iii) common techniques used for synthesising ceramic materials; and (iv) molten salt synthesis (MSS) are reviewed as follows.

2.1 Transition metal carbides and zirconium diboride

In this section, the works on zirconium carbide, titanium carbide and zirconium diboride are reviewed, with a focus on their crystal structures, remarkable properties, and potential applications.

2.1.1 Zirconium carbide (ZrC)

Zirconium carbide (ZrC) is one of the refractory transition metal carbides from groups IV to V of the periodic table possessing a cubic rock-salt (NaCl-type), as shown in Fig. 2.1. This material has recently received much interest due to its great combination of numerous attractive properties, such as its high melting point and hardness, good thermal conductivity and thermal shock resistance, high strength even at elevated temperatures, high solid-state phase stability, good wear and corrosion resistances, and relatively lower density (6.73 g/cm^3) compared to other carbides like WC (15.8 g/cm^3), TaC (14.5 g/cm^3) and HfC (12.67 g/cm^3) [7-9]. The remarkable properties of ZrC are listed in table 2.1 (data taken from [7, 8, 21]). Its superior properties make this material a potential candidate for a number of applications in ultra-high temperature and severe environments in particular, such as field emitters, coating of nuclear particle fuels and cutting tools. Furthermore, ZrC possesses a fairly low function of 3.3-3.5 eV, enhancing field emission stability and beam confinement when used as a coating on field emitter cathodes [8]. In addition, its super-resistance to attack by fission products and its high thermal and mechanical properties at elevated temperatures; thus, ZrC is being considered for use as a structural and fission product barrier coating high temperature gas-cooled reactor (HTGR) fuel particles, which would replace the currently used silicon carbide (SiC) [10, 11]. The ZrC coating layer exhibits higher temperature stability and better resistance to chemical attack by palladium, a fission product, than does the original SiC coating layer [22]. ZrC is also used as oxidation-resistant coatings on carbon substrates made for aeronautical materials such as nose tips and rocket nozzles. Such materials are employed in very severe environments and ultra-high temperatures up to 3000 °C. In oxidising atmospheres, a zirconia (ZrO_2) film is formed on the surface of the ZrC coating layer. The oxide film possesses a high melting point of 2677 °C and effectively inhibits the diffusion of oxygen into the

interior of the carbon substrate, resulting in the great protection of the carbon substrate from oxidation at ultra-high temperatures [23].

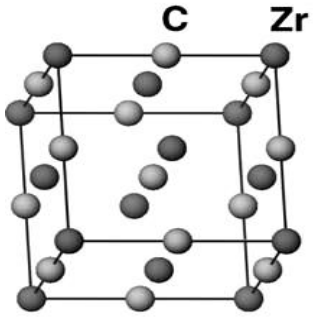

Figure 2.1 Crystal structure of ZrC (image taken from [24]).

Table 2.1:Remarkable properties of ZrC

Properties	**Zirconium Carbide (ZrC)**
Density (g/cm^3)	6.73
Lattice parameters (A)	a=b=c= 4.693
Crystal structure	Cubic (NaC1 Type)
Space group	Fm3m
Modulus of elasticity (GPa)	440
Hardness (GPa)	25.5-28.7
Melting point (°C)	3532
Electrical resistivity ($x10^{-6}\Omega$ cm)	~43
Thermal conductivity (W/mK)	20.5 W/m·K

2.1.2 Titanium Carbide

Titanium carbide (TiC) has recently attracted increasing interest and has become one of the most common and widely used carbides. This is due to a great combination of its ceramic and metallic properties, which leads this material to

possessing a high melting point, low density, extreme hardness, high mechanical stiffness, and good thermal and relative electrical conductivity [12]. TiC has a cubic rock-salt (NaCl-type) crystal structure (Fig. 2.2) with a space group of Fm3m and displays a wide range of C:Ti atomic ratios (from $TiC_{0.49}$ to $TiC_{1.0}$) without transformation of its crystal structure [25]. An overview of the most important properties of TiC is listed in Table 2.2 (data obtained from [26]).

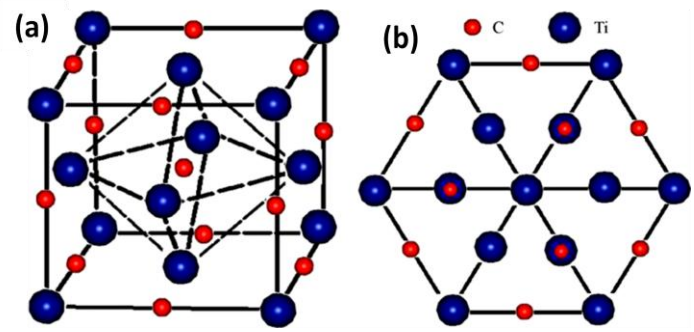

Figure 2.2 (a) The crystal structure of TiC; (b) the projection of Ti and C atom layers on a (111) plane (image taken from [25]).

Titanium carbide has found a wide range of technological applications as a potential advanced engineering structural material. Its refractory properties cause this material to be used in industry as a high-temperature ceramic, in cutting tools and abrasives, in field emitters, catalytic supporters, and reinforcements in composites, and finally as a hardening phase for superalloys [13]. TiC is also extensively utilised in pumps for transporting molten substances and is applied widely as a coating phase on the surface of engineering components to increase their hardness and/or to protect the substrate from oxidation. Moreover, TiC has recently received much interest as a material for catalytical and electrochemical applications. Such functions, however, require materials that have a fine particle size and a high specific surface area.

Table 2.2: Remarkable properties of TiC

Properties	*Titanium Carbide (TiC)*
Density (g/cm^3)	4.93
Lattice parameters (A)	a=b=c=4.306
Crystal structure	Cubic (NaCl Type)
Modulus of elasticity (GPa)	410–450
Vickers Hardness (GPa)	28-35
Melting point (°C)	3067
Electrical conductivity (x10^6 S/cm)	30
Thermal conductivity (W mK^{-1})	16.7

Apart from powders, one-dimensional TiC nanostructures such as nanotubes, nanowires, and nanowhiskers have attracted considerable attention since the discovery of carbon nanotubes by Iijima [27] in 1991. Titanium carbide structures with these morphologies have become potential candidates for use in electronics and optical technologies. For example, TiC is applied as a potential material for electromagnetic wave absorption due to its extreme melting temperature, low density, superior environmental stability and relative electrical conductivity [28]. As a promising field emitter material [29-32], TiC exhibits the desirable property of having a lower work function, leading to strong field emission. Furthermore, TiC/C nanofibres have been utilised in building excellent scaffolds for high performance silicon anode batteries due to the highly conductive, mechanically robust and electrochemically inactive properties of the material [33]. Similarly, 2D-nanostructured materials have received great attention from researchers since the discovery of a novel material named graphene in 2004 by scientists at the University of Manchester. Graphene is a two dimensional crystalline material that composes of a single atomic layer of carbon bonded together in a flat honeycomb structure. Graphite consists of graphene layers stacked together by

weak van der Waals forces. Each graphene layer, therefore, can be produced easily via mechanical cleavage and chemical techniques [15-17].

Because the 2D nanostructure of graphene exhibits much better mechanical, physical, electrical and electronic properties than graphite, layer-structured materials are currently fabricated in the form of graphene-like materials (also known as white graphene). Graphene-like materials exhibit the 2D structure of mono-atom-thick graphene-like sheets, such as single-layer BN, MoS_2 and WS_2 [34-39]. To produce graphene-like forms, layer-structure materials can be exfoliated using similar fabrication techniques as those used in graphene production [40, 41]. However, it is challenging work to fabricate either graphene-like forms or 2D nanostructures of non-layered carbide materials since transition metal monocarbides possess a 3D-cubic structure of strong directional bonds and exhibit metallic-like phases. Such structures provide outstanding properties to the materials, such as extreme hardness, high melting points, high electrical conductivity, good chemical stability and high resistance to wear and corrosion [12]. The combinations of these properties make the materials promising candidates for cutting tools, wear-resistant parts, high-temperature structural applications and reinforcements in composites [42].

Interestingly, the fabrication of graphene-like or 2D-nanostructured carbides has been very limited until now due to their non-layered structure. It is thus difficult to exfoliate such materials into the necessary morphology. By consequence, this has led to the extensive research and development of alternative processing routes for fabricating the corresponding 2D-nanostructured carbides.

Quasi-2D transition metal carbides as well as nitrides and their complex compounds have been synthesised by the utilisation of recently discovered

ternary MAX phases [43-50]. The general formula of a MAX phase is $M_{n+1}AX_n$, (n = 1–3), where M represents a transition metal, A is an element predominantly from the transition metal groups (IIIA or VIA), and X can be either C or N. The elemental layers (A) in a MAX phase structure can be exfoliated to leave behind a nanolaminate structure of $M_{n+1}X_n$, which can be further exfoliated into $M_{n+1}X_n$ nano-blocks by an external force such as ultrasonication. For example, 2D-Ti_3C_2 layers have been extracted from the Ti_3AlC_2 phase (Fig. 2.3) by the extraction of Al-sheets from the structure using HF acid treatment for 2 hours via reaction (2.1), followed by ultrasonication to exfoliate nano-blocks of the reacted product phase (Ti_3C_2). The obtained Ti_3C_2 nano-blocks from this fabrication technique have been termed MXene by the authors [51]. The processing scheme for MXene exfoliation is illustrated in Fig. 2.4.

$$2Ti_3AlC_2 + 6HF = 2AlF_3 + 3H_2 + 2Ti_3C_2 \qquad (2.1)$$

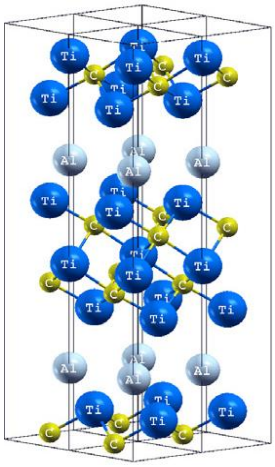

Figure 2.3 Fragments of the atomic structure of $Ti_{n+1}AlC_n$MAX phase (image taken from [52]).

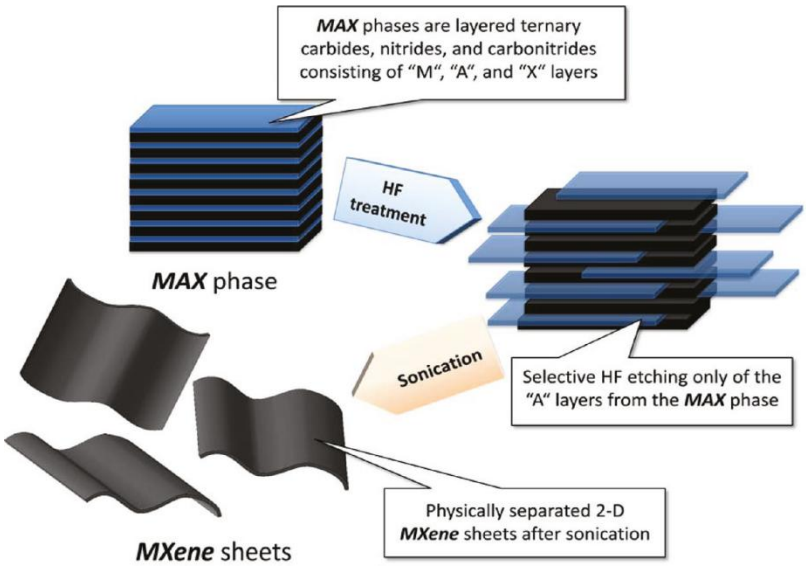

Figure 2.4 Schematic image showing the exfoliation process of a MAX phase and the production of MXenes (the image is taken from [51]).

2.1.3 Zirconium diboride (ZrB_2)

Zirconium diboride (ZrB_2) is a transition metal boride possessing a hexagonal crystal structure of the AlB_2 type, as shown in Fig. 2.5. This crystal structure consists of alternating layers of hexagonal zirconium (Z) and boron (B) atoms stacked together in a ZBZBZB sequence [2]. This structure provides strong covalent bonding of the B-B and Z-B atoms as well as metallic bonding that results from the metal layers. The great combination of covalent and metallic bonding leads materials with this structure to possess a remarkable combination of properties. The highly covalent nature gives rise to a high melting point, extreme hardness, and high four-point flexural bending strength [1]. Meanwhile, the metallic bonding causes relative electrical and thermal conductivities. This material also exhibits extreme thermal shock resistance, a low coefficient of thermal expansion, well-preserved strength at elevated temperatures, good oxidation resistance at temperatures up to 2000 °C, and high resistance to

chemical attack and extreme environments [2]. The notable properties of ZrB_2 are listed in table 2.3 (data taken from [1-3]).

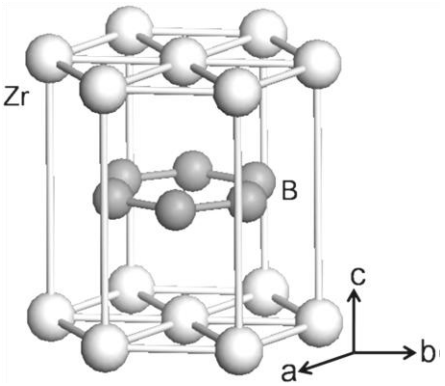

Figure 2.5 Crystal structure of ZrB_2 (image taken from [53]).

ZrB_2 is classified in the division of ultra-high temperature ceramics (UHTCs), which are applied in a wide range of high-temperature applications. The excellent thermal shock and oxidation resistances at elevated temperatures as well as the extreme hardness and strong mechanical properties make this material a great choice for thermal protection materials on hypersonic flights, atmospheric re-entry vehicles with sharp leading edges and nose caps, and in rocket propulsion [6]. Furthermore, ZrB_2 has a high resistance to molten metals and slags, which makes the material a good candidate for use as a protective sleeve in submerged entry nozzles in steel making industries, furnace elements and refractory crucibles [53]. The material is also used in high-temperature electrodes in plasma fields due to its extreme resistance to plasma sparks and arcs [22, 54]. Moreover, ZrB_2 possesses high electrical conductivity, which leads to its potential use in Hall-Heroult cell cathodes and electrical discharge machining [55, 56].

Table 2.3: Remarkable properties of ZrB_2

Properties	*Zirconium Diboride (ZrB_2)*
Density (g/cm^3)	6.09
Lattice parameters (A)	a = b = 3.168, c =3.527
Crystal structure	Hexagonal
Modulus of elasticity (GPa)	440–460
Four-point flexural bending strength (MPa)	565
Hardness (GPa)	12-22
Melting point (°C)	3246
Electrical resistivity (x10^{-6} Ω^{-1} cm)	9.2
Thermal conductivity (W/mK)	23-25
Coefficient of thermal expansion (x10^{-6} °C^{-1})	5.9
Oxidation resistance up to temperature (°C)	2000

Because the mechanical properties and oxidation resistance are adversely affected by porosity levels of a material, careful control of the densification and the microstructure is therefore required to obtain favourable properties of the material after sintering. Sintering pure ZrB_2 and other transition metal boride powders with relatively high densities is rather difficult due to their extremely high melting point and the high vapour pressure of the constituents [4]. In most cases, ZrB_2-based materials are fabricated by hot pressing at high temperatures (above 1900 °C) and applied pressure of 20-30 MPa and higher to achieve a relatively high density of ZrB_2 [5]. This processing method, however, limits the production of the materials to those with relatively simple geometric figures. Surface finishing processes are therefore required to further fabricate complex components, but these processes involve the application of diamond machining, which is expensive and time-consuming. Pressureless sintering processes can enable near net shape of the final products, which would be far more economical

than the conventional hot pressing and machining methods. This has been confirmed by Chamberlain et al. [57], who found that ZrB_2 ceramics with a relatively high density of 98% were effectively sintered at a temperature range of 1900-2150 °C without the assistance of external pressure.

Due to its brittle nature, however, monolithic ZrB_2 is susceptible to brittle fracture like other ceramic materials [58, 59]. Thus, there are limited applications of monolithic ZrB_2 based UHTCs. An effective way to toughen brittle ceramic materials is to reinforce them with a ductile metallic phase because the ductile phase can minimise and/or prohibit the formation of cracks within the matrix by dispersing the energy of crack initiation and propagation through plastic deformation, resulting in significantly tougher ceramic materials [60]. For example, Sun et al. [61] successfully prepared ZrB_2-Nb (ZN) composites using the hot pressing technique. With the introduction of metallic Nb by 25 vol% into the ZrB_2 matrix, the flexural strength and fracture toughness of the composites are 773 MPa $m^{1/2}$ and 7.1 MPa $m^{1/2}$, respectively, which are much higher values than those of monolithic ZrB_2.

2.2 Processing techniques for fabricating ceramic powders

The sinterability of ceramic powders is significantly influenced by the powder characteristics of purity, shape, particle size, surface area and defect concentration. It has been claimed that using a finer particle size of the starting materials could increase the driving force for densification and decrease the grain size of the sintered ceramics [62]. For example, ZrB_2 ceramic with a relatively high density of 97.6% was achieved after pressureless sintering at 2000 °C by using ZrB_2 powder with a particle size of ~200 nm [63]. The powder characteristics, however, are governed strongly by the synthesis conditions,

including the processing method, reaction temperature and time. Therefore, the selection of the synthesis method and processing conditions are important in achieving the required quality of the product and the right application of the synthesised powder.

A number of synthesis techniques commonly used for fabricating ceramic materials are reviewed and categorised into three groups based on the reaction states (solid, liquid and vapour) during synthesis, as described below.

2.2.1 Solid phase reaction techniques

2.2.1.1 Carbothermal reduction process

Carbothermal reduction is an inexpensive and simple operation and is therefore the most common industrial technique used for commercially fabricating ceramic powders. The process involves the reduction of ZrO_2 with boron and carbon sources for ZrB_2 fabrication, as shown in reaction (2.2). A reduction of ZrO_2 or TiO_2 with carbon at elevated temperatures in an inert atmosphere or a vacuum system is required for ZrC or TiC fabrication, as indicated by reactions (2.3) and (2.4), respectively [64-66].

$$ZrO_2 + B_2O_3 + 5C = ZrB_2 + 5CO \qquad (2.2)$$

$$ZrO_2 + 3C = ZrC + 2CO \qquad (2.3)$$

$$TiO_2 + 3C = TiC + 2CO \qquad (2.4)$$

Reactions (2.2)-(2.4) are highly endothermic and thus require intensive processing temperatures (1700-2500 °C) and time (16-24 hours) [67] to completely process the reactions. For example, reaction (2.2) is only thermodynamically favourable at temperatures above 1500 °C [2], whereas reaction (2.4) is

favourable at temperatures above 1289 °C [26]. However, product powders are normally formed at processing temperatures much higher than the favourable temperature predicted by the thermodynamic calculations. This is due to the kinetic barriers caused by solid-solid state reactions, such as poor mass transportation and contact areas between the solid reactants as well as the non-homogeneous distribution of carbon particles in the mixture [26]. Therefore, the completion of the reactions requires high processing temperatures and prolonged dwell time. These requirements lead to undesired phenomena such as grain growth, particle agglomeration, non-uniform particle shape and significant quantities of impurity phases, limiting the further applications of the synthesised powders. An example is that the poor sinterability of the coarse powders leads to high porosity levels in the sintered bodies. Therefore, an additional process of crushing and grinding is required to reduce the particle size of the products produced by this method prior to their further application. This could lead to the contamination of the product powders which could be introduced during the grinding process. In addition, products with low purity are normally obtained during the first heating cycle of the carbothermal reduction process due to the presence of intermediate oxycarbide phases and residual phases of the starting precursors [68, 69]. Furthermore, the degree of carbonisation for a solid state reaction depends not only on reaction temperature and time but also on the homogeneous mixing and surface chemistry of the reactant powders. Finally, the reaction atmosphere must be strictly controlled by either a vacuum or inert gas to protect the carbon powders from oxidisation.

Numerous literature sources have reported the fabrication of ZrB_2, ZrC and TiC powders via the carbothermal reduction technique. For example, Jung et al. [70] synthesised ZrB_2 powder with a large particle size of 2-4 μm, though the product powders contained high concentrations of impurity phases at the reaction

temperature of 1250 °C. Maitre et al. [67] fabricated ZrC powder at 1460 °C for 12 hours with the contamination of oxycarbide impurities. Sen et al. [71] prepared TiC powder via the carbothermal reduction of TiO_2 with charcoal at 1550 °C for 4 hours in vacuum after ball-milling the starting mixture for 10 hours. From this reaction, coarse TiC powder (~ 1 μm) was obtained.

A number of efforts to improve the drawbacks of this processing route have been reported. Ali and Basu [72] prepared TiC powder at a much lower temperature than that required in the traditional carbothermal synthesis by employing high-energy ball-milling to activate the formation of TiC from a carbothermal reaction of TiO_2 with graphite. The carbothermal reduction took place at 1200-1300 °C after a prolonged-milling time (30-90 hours) of the mixture. This was due to the mechanical activation process, which enhanced the reactivity of the solid reactants. However, although the synthesis temperature was considerably reduced in this method, intermediate oxide phases such as Ti_3O_5 and Ti_2O_3 were formed during synthesis and remained as impurities in the final product powder.

2.2.1.2 Self-propagating high temperature synthesis (SHS)

Self-propagating high temperature synthesis (SHS), or combustion synthesis, is a method used for synthesising inorganic materials (typically refractory ceramics). This method takes advantage of the release of highly exothermic energy during chemical reactions to generate high temperatures and rapid combustion reactions to form the desired materials. The typical characteristic of this processing route is that the heat required for processing the chemical reaction is provided by the reaction itself.

Compared to other conventional solid state synthesis techniques, this process offers a number of advantages, including high purity of the products, a shorter

processing time, low energy consumption (including the ignition stage), and simple operation [14]. However, the product produced via this route usually contains high concentrations of defects due to rapid cooling rates. High concentrations of defects in the product powders promote the sinterability of the resultant powders during the hot pressing process [3, 73].

Nevertheless, it should be noted that the high purity of the product powders can be achieved via this technique only when elemental powders are used as starting materials. Otherwise, a large amount of impurities always remains in the resulting products because the rapid cooling rate leads to incomplete chemical conversions [74]. Furthermore, it is difficult to gain fine particles of product powders using this technique because of its high reaction temperatures. This limitation, however, can be overcome by the addition of NaCl to the starting mixture [14, 74, 75]. Khanra et al. [14] synthesised nanocrystalline ZrB_2 through the reaction of ZrO_2, Mg, and H_3BO_3 with the addition of NaCl as an inert diluent to control the particle size of the product. The introduction of NaCl does not adversely affect the SHS mechanism but is believed to absorb excess heat energy and maintain the fine particle size of the synthesised powders. The product powders produced using this improved process exhibited a particle size of 25-40 nm, which is much finer than the powders prepared in the original SHS process without NaCl addition, which possessed a particle size of 75-125 nm. The synthesised ZrB_2, however, contains some residual ZrO_2 as a main impurity, indicating an incomplete synthesis reaction. Camurlu and Maglia [74] produced nanosized ZrB_2 powders (less than 200 nm) from the direct reaction of Zr and B elemental powders by varying the addition amounts of NaCl. Their findings demonstrated that the presence of NaCl strongly influences the crystal size (calculated from Scherrer formula) of the synthesised powders. The averaged crystal size of the resultant powders decreased from 303 nm to 32 nm when up to

40 wt.% NaCl was added. The particle sizes of the product powders decreased from 2-4 μm without the addition of NaCl to less than 200 nm with the addition 30 wt.% of NaCl, as shown in Fig. 2.6. In this case, no impurities were detected, leading to the conclusion that the reaction was completed.

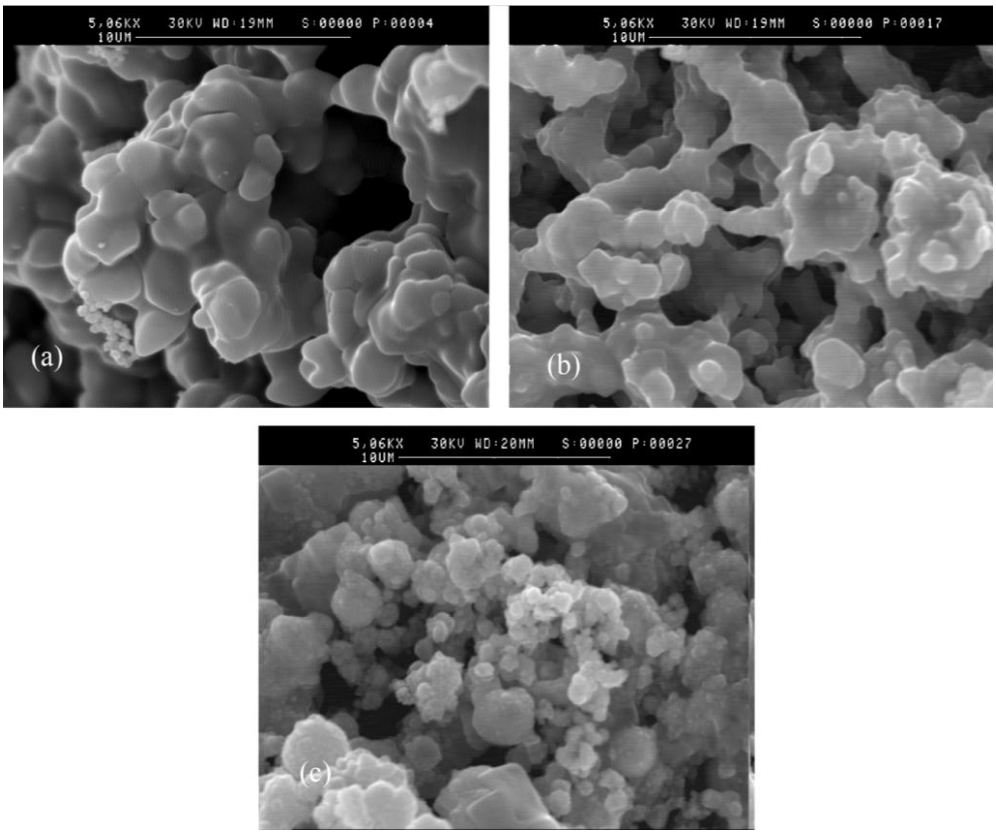

Figure 2.6 SEM images of the fracture surfaces of the products obtained from Zr-B samples containing (a) 0, (b) 10 and (c) 30 wt.% NaCl (images reprinted from [74]).

Similarly, Zhang et al. [76] prepared ZrC particles using elemental Fe, Zr, and C powders via the SHS technique at 1400 °C. It was found that the addition of Fe into a Zr-C mixture not only enhanced the formation of the ZrC phase but also significantly reduced the grain size of the produced powders, as illustrated in Fig. 2.7. These observations were attributed to the dissolution of carbon into the

melted Fe-Zr and its subsequent reaction with Zr, forming ZrC as a final product. However, a number of impurity phases such as ZrO_2, Fe, and Fe_2Zr were present in the final product, even when heated to temperatures as high as 1250 °C and with the addition of 30 wt.% Fe.

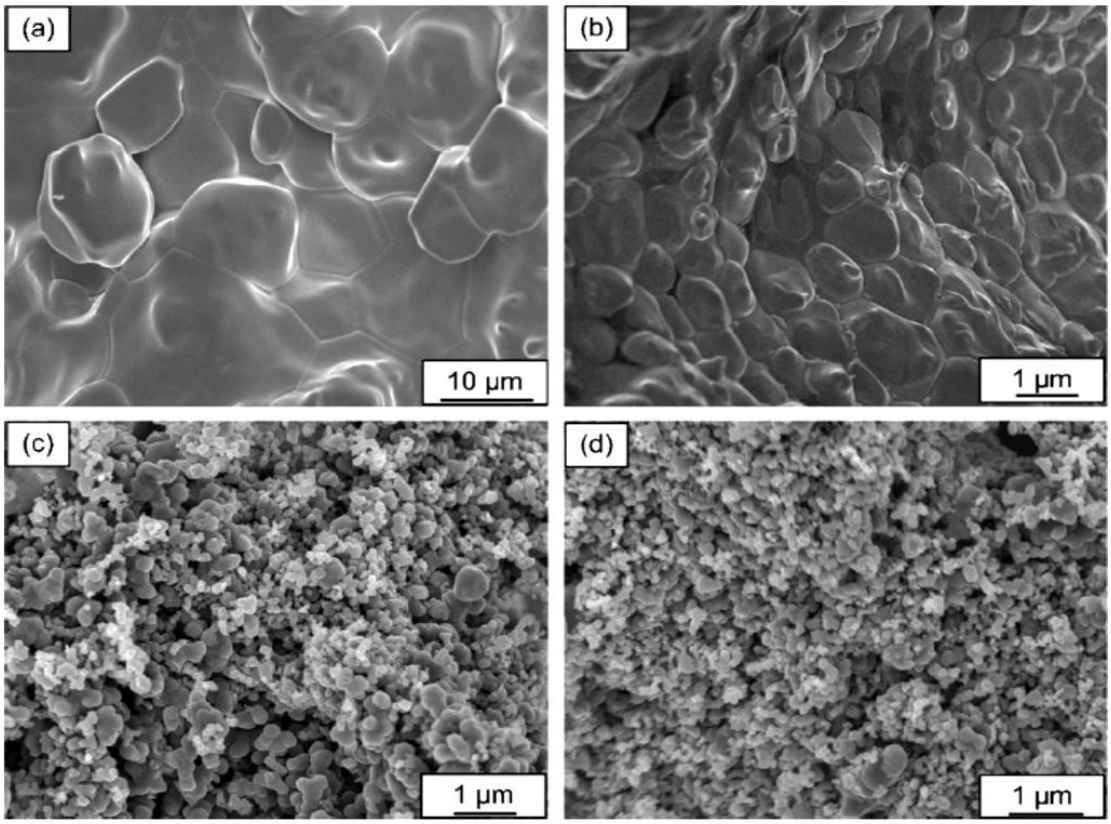

Figure 2.7 Micrographs of the SHS products containing (a) 0, (b) 10, (c) 20, and (d) 30 wt.% Fe (images reprinted from [76]).

Further, Song et al. [77] synthesised nanocrystalline ZrC particles using the SHS process via the reaction system of Al-Zr-C. The formation of ZrC was attributed to the dissolution of C in the Al-Zr melt at an elevated temperature. However, the reaction was relatively slow even though the synthesis temperature was raised to 1953 °C. The final product produced via the reaction system of Al-Zr-C usually contains impurity phases of Al and $ZrAl_3$. In a titanium carbon-black

reaction system containing a 30 wt.% addition of NaCl, nanosized TiC particles (20-100 nm) were prepared by Nersisyan et al. [78]. They claimed that NaCl not only reduces the combustion temperature but also maintains the ultrafine structure of the product until the completion of combustion by forming protective shells around the primary carbide crystals, resulting in limited grain growth. Apart from NaCl, the addition of metallic powders such as Al, Fe, and Cu can also decrease the combustion temperature, prohibiting the grain growth. For instance, Song et al. [13] found that the grain size of TiC_x powder decreased from 3 μm to 400 nm with increasing amounts of added Al from 10 to 40 wt.%, as demonstrated in Fig. 2.8. With more Al content present in the system, the combustion temperature is lower and the dwell time is shorter, resulting in a sharp reduction of TiC particle size because higher combustion temperatures and longer dwell times favor grain growth. Additionally, the increased amount of liquid Al surrounding the TiC grains gives rise to the increase in the diffusion paths, leading to the reduction in the driving force for TiC grain growth and thus preventing TiC grains from coarsening within a limited time [13]. Similar observations were found by Jin et al. [79] in the reaction system of metallic titanium powders and carbon nanotubes. With the addition of increasing amounts of metal (Cu, Al, or Fe), the metallic powders not only promoted the ignition of the SHS reaction but also effectively decreased the synthesised TiC_x particle sizes.

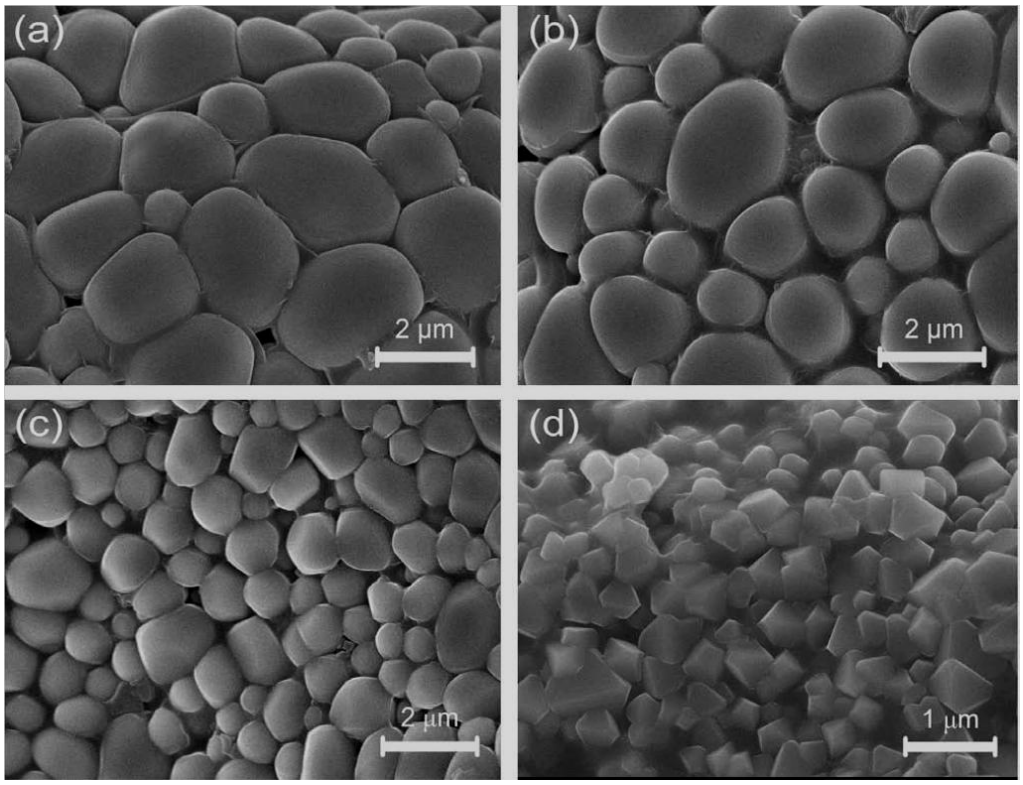

Figure 2.8 Microstructures of the SHS products containing (a) 0, (b) 10, (c) 20, and (d) 30 wt.%Al (images reprinted from [13]).

2.2.1.3 Mechanochemical process

Mechanochemical synthesis, which is well known as mechanical activation (MA), is a solid-state powder processing method that occurs in a high-energy ball mill. The process involves repeated welding, cracking and rewelding of the starting powders. Chemical reactions may take place at room temperature, under prolonged milling times, and/or during heat treatment after the milling process. Currently, this technique has been applied widely to fabricating a number of advanced ceramic materials such as carbides, nitrides and borides. The application of high-energy ball milling is aimed at reducing the particle size of the starting mixture and thus increasing the surface areas between the reactants. This leads to the enhanced reactivity and mixing homogeneity of the reactants, leading to markedly lower synthesis temperatures. Nevertheless, contamination

of the product powders caused by milling equipment (including the vial, balls and grinding medium) during the grinding process is a major concern. Akgün et al. [80] synthesised ZrB_2 powders via the magnesiothermic reduction of a ZrO_2-B_2O_3-Mg reaction system with the assistance of wet ball milling for 30 hours. Side products MgO and $Mg_3B_2O_6$ were observed along with ZrB_2 and unreacted ZrO_2 phases. The presence of residual ZrO_2 indicated an incomplete synthesis reaction. Rahaei et al. [81] fabricated nanosized TiC powders through the mechanochemical reaction of metallic titanium and graphite for 16 hours, finding that the particle size of the product powders decreased significantly under prolonged milling times. However, it was noted that the purity level of the product powders decreased with the milling time due to contamination of Fe impurities that was caused by abrasion of the balls and vial during the grinding process. Lee et al. [82] produced nanosized ZrC powders using $ZrCl_4$ as a zirconium source and carbon black as a carbon source with $NaHCO_3$ as a reductant. The reactants were initially mixed by ball-milling for 4 hours prior to heat treatment at a high temperature. After heat treatment at 1400 °C, ZrC powders with a particle size of 150 nm were fabricated along with a small amount of residual ZrO_2. Mahday et al. [64] fabricated nanocrystalline $Zr_{56}C_{44}$ via the MA process using elemental powders of zirconium and carbon as the starting materials. The product phase formed at room temperature when the mixture was subjected to high-energy ball-milling for 72 hours in an argon environment.

2.2.1.4 Magnesiothermic reduction

Magnesiothermic reduction is a method using metallic magnesium powder (Mg) as a reducing agent for the synthesis of ceramic materials and is normally performed by volume combustion synthesis (VCS) or self-propagating high temperature synthesis (SHS). A number of research studies on the preparation of metal borides and carbides using this technique have been reported. The raw

materials used in this processing route generally include Mg powder (reducing agent), B_2O_3 (boron source), and either TiO_2 (titanium source) or ZrO_2 (zirconium source) to fabricate TiB_2 or ZrB_2, respectively. The overall chemical reactions for TiB_2 and ZrB_2 synthesises via this route are shown in Reactions (2.5) and (2.6), respectively.

$$TiO_2 + B_2O_3 + 5Mg = TiB_2 + 5MgO \quad (2.5)$$

$$ZrO_2 + B_2O_3 + 5Mg = ZrB_2 + 5MgO \quad (2.6)$$

Some examples for preparing metal borides via the magnesiothermic reduction method are described here. Sundaram et al. [83] synthesised TiB_2 using a chemical reaction system of TiO_2–Mg–B_2O_3. The formation of an unwanted $Mg_3B_2O_6$ phase was noticed in this study along with the expected phases of TiB_2 and MgO. Akgün et al. [80] used volume combustion synthesis (VCS) and mechanochemical processes to fabricate ZrB_2 from a ZrO_2–Mg–B_2O_3 reaction system. The results showed incomplete conversion of ZrO_2 to ZrB_2, although excessive amounts of Mg and B_2O_3 were introduced into the reaction system to compensate for their evaporated losses at elevated temperatures during the synthesis. Furthermore, the unwanted $Mg_3B_2O_6$ phase was observed and remained as an impurity. Likewise, Bilgi et al. [84] reported that an intermediate $Mg_3B_2O_6$ phase was formed when TiO_2, Mg and B_2O_3 were used as starting materials for preparing TiB_2 powders. Setoudeh and Welham [85] synthesised ZrB_2 through the MA process via the magnesiothermic reduction of a ZrO_2-Mg-B_2O_3 reaction system. Although the mixture was milled using high-energy ball milling for 15 hours prior to the heat treatment process, the reaction was incomplete at 1200 °C. In this case, however, the formation of the undesired $Mg_3B_2O_6$ phase did not occur. Similarly, Khanra [86] prepared ZrB_2 powder through the magnesiothermic reduction of a ZrO_2–Mg–H_3BO_3 system without

the formation of the $Mg_3B_2O_6$ side product. The product powder, however, contained some unreacted ZrO_2 as a major impurity phase. Using a reaction system of ZrO_2-Mg-CH_4 at 750 °C, Kobayashi et al. [87] synthesised ZrC powders that had high purity but were extremely agglomerated (Fig. 2.9).

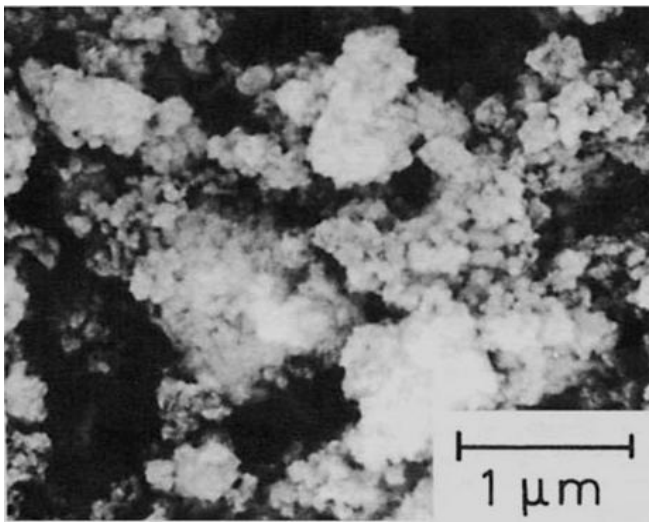

Figure 2.9 SEM image of ZrC powders fabricated in the reaction system of ZrO_2-Mg-CH_4 (image reprinted from [87]).

With references to the literature, several drawbacks of the magnesiothermic reduction process are listed here. First, the by-product MgO always exists in the resultant powder, leading to an additional processing step of acid treatment to eliminate the by-product phase. Second, undesirable intermediate-phases such as $Mg_3B_2O_6$, and $Mg_3(BO_3)_2$ are often present in the final product. Such phases are difficult to remove in dilute acid solutions. Finally, an excessive amount of Mg is normally added to the reaction system to compensate for the lost amount due to evaporation at elevated temperatures, thus allowing for the complete reduction of oxide phases in the system.

2.2.2 Solution based synthesis

Sol-gel, or solution-based synthesis, is a method operating by mixing a solution of reactants at the atomic or molecular scale and heating the solution to a certain temperature (~1500 °C) to obtain the desired products. The use of solution precursors instead of a physical mixture of the solid compounds strongly enhances the mixing of the reactants at a molecular level, giving rise to a more efficient diffusion reaction and reduction in the synthesis temperature and reaction time compared with solid phase reactions. Moreover, with the advantage of mixing at the molecular level, the product phase could be formed from seeded gel precursors, resulting in a fine grain size of the final product [88]. This method, however, requires an extra step of drying the mixture, which takes ~24 hours of time prior to further processing by carbothermal reduction. In this case, the carbothermal reduction process normally requires a shorter reaction time (~6 hours) than the conventional carbothermal reduction synthesis due to mixing of the reactants at the molecular level [89]. This method is therefore beneficial for producing high-quality and ultrafine ceramic powders. Nonetheless, the processing route suffers from various disadvantages, such as expensive precursors, complex and time-consuming procedures, toxicity, and residual oxygen impurity in the resultant powders, leading to a limited use of this method in commercial production [90, 91].

A number of research studies on the fabrication of ceramic powders via the sol-gel technique have been reported. For example, Li et al. [92] prepared nanosized ZrB_2 powders at 1550 °C for 2 hours using zirconium n-propoxide ($Zr(OPr)_4$), boric acid (H_3BO_3) and sucrose ($C_{12}H_{22}O_{11}$) as precursors. Wang et al. [93] used a novel precursor-derived process involving $Cp_2Zr(CHCH_2)_2$ and H_3B at 1600 °C for 2 hours to synthesise ZrC/ZrB_2 powders. Xie et al. [94] fabricated ZrB_2

powders at temperatures above 1500 °C for 2 hours by polymeric precursor pyrolysis using $[(C_4H_8O)Zr(acac)_2]$ and $(NHCH_3)_3B_3N_3H_3$ as the raw materials. Recently, it has been proposed that the key parameter in the sol-gel processing route for the synthesis of ZrB_2 is the Zr-O-Zr network structure formed by zirconium hydrolysis and condensation reactions [92, 95]. However, because boric acid did not participate (but was only dissolved) in building up the network structure of sol-gel, boron was not homogenously distributed throughout the sol. This limitation strongly influenced the synthesis temperature and morphologies of the product particles. Ji et al. [96] solved this problem by introducing a modifier called sorbitol to enhance the formation of the Zr-O-C-B network. Sorbitol functions as a bridge bond allowing boron to participate in the building up of the network, leading to increased stability and uniformity of the sol. This resulted in a lower synthesis temperature (1450 °C), a shorter holding time (1 hour), and a finer particle size of the product (Fig. 2.10).

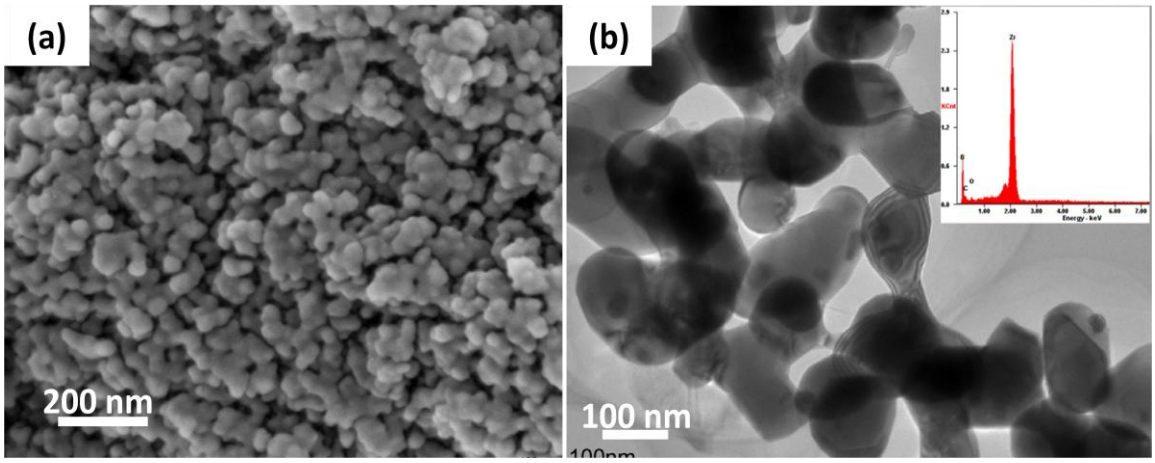

Figure 2.10 SEM (a) and TEM (b) images of ZrB_2 powder heated at 1450 °C for 1 hour (images reprinted from [96]).

Yan et al. [97] prepared ZrC powder via the sol-gel technique using zirconium oxychloride octahydrate ($ZrOCl_2 \cdot 8H_2O$, ZOC), acetylacetone (acac) and phenolic

resin. The complete formation of ZrC was achieved at 1550 °C in the environment of flowing argon. Ang et al. [98] synthesised fine ZrC powder of less than 100 nm from zirconium *n*-propoxide and carbon as the starting materials via the sol-gel technique with the assistance of a polymer surfactant for homogeneously mixing the mixture. The ZrC phase product was evident at 1250 °C and the reaction was completed at 1450 °C. Doll et al. [99] prepared nanocrystalline ZrC using zirconium *n*-propoxide as a zirconium source, saccharose as a carbon source, and acetic acid as a chemical modifier. Although ZrC was apparent at temperatures above 1200 °C, a high oxygen content remained, and as a result, the sample was further purified to minimise oxygen content by heating at 1600 °C. Sevastyanov et al. [100] synthesised nanosized ZrC, TiC and HfC powders from their metal oxides (MO_2, where M represents Zr, Ti and Hf) via a two-step process of sol-gel and carbothermal reduction techniques. The application of the sol-gel technique is to enhance the mixing of the starting mixture (MO_2-C) prior to carbothermal reactions at a designed temperature range. Likewise, Yan et al. [91] synthesised ultra-fine ZrC powder via carbothermal reduction and sol-gel processes using $ZrOCl_2 \cdot 8H_2O$ and phenolic resin as zirconium and carbon sources, respectively. With the assistance of sol-gel technology, the reactions were completed at ~1400 °C. In addition, Chandra et al. [101] synthesised nanocrystalline TiC through a carburisation reaction of a titanium precursor gel and nanosized carbon particles obtained by burning clarified butter at a temperature range of 1300–1580 °C for 2 hours in an argon environment. It was found that nanosized TiC particles were formed at temperatures below 1500 °C after 2 hours of holding time. Zhong et al. [102] fabricated mesoporous TiC microspheres using titanium tetraisopropoxide (TTIP, $Ti(OCH(CH_3)_2)_4$ and furfuryl alcohol (FA, $C_5H_6O_2$) as titania (TiO_2) and carbon sources, respectively, to prepare the TiO_2/C precursor. This was followed by a

carbothermal reduction process at 1450 °C for 5 hours in argon to obtain a single TiC phase as the final product.

2.2.3 Vapour phase fabrication

It is difficult to achieve a fully dense ceramic after sintering high melting-point materials such as refractory carbides, though high-processing temperatures (up to 2300 °C) are applied [103]. A dense and uniform characteristic of such materials, however, can be accomplished by coating technology. The vapour phase fabrication method is primarily focused on the production of coatings in which low porosity and impurities in the final products are crucial. These processing techniques include, for instance, chemical vapour deposition (CVD), evaporation, and physical sputtering. For example, to coat ZrC onto high temperature gas-cooled reactor (HTGR) fuel particles, vapour deposition techniques are involved due to the high melting temperature and low diffusivity of ZrC [103]. Among the vapour phase deposition techniques, CVD is the most widely employed to prepare coatings [8, 104-108]. The CVD method typically offers pure and uniform coatings on surfaces of the substrates, especially spherical ones. TiC and SiC coatings on graphite specimens were fabricated through the CVD method using $TiCl_4$, $SiCl_4$, and CH_4 as the Ti, Si, and C sources, respectively [109]. It was claimed that the surface morphologies of both SiC and TiC were coarser when the input ratio of H_2 was increased. This phenomenon was attributed to the more rapid grain growth of the deposited SiC and TiC films due to the increase in the deposition rate when the input ratio of H_2 was increased. TiC coatings were successfully deposited on Ti substrates via an ion-enhanced triode plasma CVD method using the gas mixture of $TiCl_4$, CH_4, H_2 for application as abrasion-resistant materials [110]. The Vickers hardness of the coating layer was approximately 15 times higher than that of the Ti substrate. In

addition, ZrC-C coating films were produced by Ogawa et al. [107] via the CVD route using a gas mixture of $ZrBr_4$, CH_4, H_2 and Ar as the starting precursors. The deposition process was performed over a wide temperature range of 600-1800 °C. In this case, it was noted that the availability of CH_4 is the key parameter controlling the extent of decomposition. Ogawa et al. [104] also deposited ZrC films onto ThO_2, UO_2 and Al_2O_3 particles at 1350-1600 °C via the CVD method using a gas mixture of $ZrBr_4$, CH_4, H_2 and Ar. The findings showed that the synthesised ZrC films obtained above 1500 °C exhibited a blistered surface and lower density compared to those samples prepared at the temperatures below 1500 °C. Ikawa [106] prepared ZrC-C coatings via the CVD process, in which $ZrCl_4$ was supplied from the chemical reaction of a zirconium sponge and methylene dichloride over a temperature range of 400-600 °C. An appreciable deposition of the composite films occurred at temperatures above 1000 °C. Furthermore, the author noted that H_2 is essential in the process involving methylene dichloride. Randich [111] achieved the fabrication of ZrB_2 and TiB_2 coatings for photothermal solar absorber applications via the CVD method. Motojima et al. [112] prepared ZrB_2 coatings on a copper plate from a gas mixture of $ZrCl_3$, BCl_3, H_2 and Ar at a temperature range of 700-900 °C to protect the copper substrate from acidic attack. Peirson et al. [113] used remote plasma-enhanced chemical vapour deposition to investigate the influence of post-discharge compositions (Ar-H_2, Ar-H_2-BCl_3, and Ar-BCl_3) on the deposition of ZrB_2 films on Zircaloy-4 substrates. It was found that, among Ar-H_2, Ar-H_2-BCl_3, and Ar-BCl_3 post-discharges, dense and uniform ZrB_2 films (Fig. 2.11) could only be synthesised in Ar-BCl_3 post-discharge.

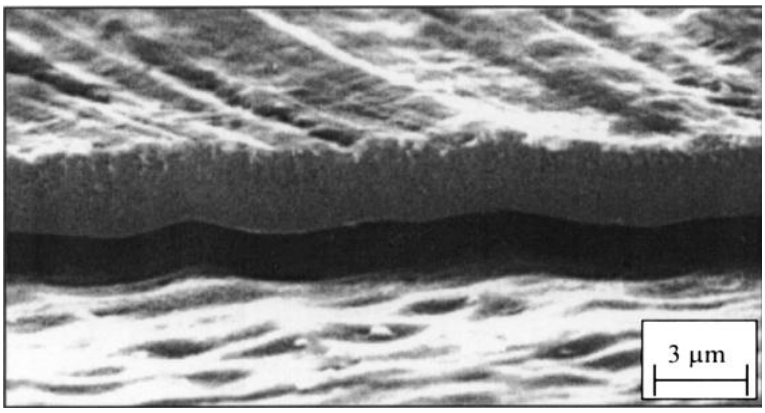

Figure 2.11 SEM image showing cross-section of the synthesised ZrB_2 film deposited on Zircaloy-4 in an Ar-BCl_3 post-discharge (image reprinted from [113]).

2.3 Porous ceramics

Porous ceramics are currently desirable for a wide range of applications due to their excellent properties of low bulk density, low specific heat, low thermal conductivity, high thermal shock resistance, high surface area, excellent permeability and good chemical stability at high temperatures [114]. These remarkable properties make the materials as potential candidates for many technological applications, including catalyst supports, filters for molten metals and/or hot gases, thermal insulation, gas combustion burners, light weight structural materials and biomaterials [115, 116].

The word "pore" normally refers to the three characteristics of pores, or their morphology, porosity, and pore size [117]. Pore morphology is subdivided into open and closed pores. Open pores refer to those pores which fluid and/or gas can penetrate through, whereas closed pores are those with non-penetrating properties. The total volume fraction of open and closed pores is indicated as the "porosity level" of a porous material [118].

The pore features present in a porous ceramic material, which include the total porosity, pore types, pore sizes, pore shapes and pore size distribution, are crucial parameters for defining the materials' properties such as its mechanical strength, modulus of elasticity, thermal conductivity, and chemical and thermal shock resistances. Furthermore, the pore types (closed and open pores) in the material determine some related properties of the material. Open pore ceramics are potential candidates for use in fluid transport and as molten metal filters in separation-filtration industries. Conversely, a high volume fraction of closed pores in the ceramic structure is beneficial for thermal insulation [119]. Pore size is also an important characteristic that defines the permeability of fluid through the pores. The bigger the pore is, the more easily the fluid flows [120]. However, the requirement in pore size of porous ceramics highly depends on the desired applications. For example, micro-porous ceramics (pore sizes < 2 nm [121, 122]) are mainly required for sewage purification [123], while macro-porous ceramics (pore sizes > 50 nm [114, 122]) are suitable for bone implantation [124]. Apart from these pore characteristics, the pore size distribution and pore shapes are relatively dependent on the desired functions of the ceramic in the particular applications of the end users.

The pore characteristics of porous materials not only define the materials' functions but also strongly dominate their properties. For example, the flexural strength of a porous ceramic material decreases with increasing porosity [125], whereas macroporous ceramics with smaller pore sizes normally exhibit better flexural strength than those with larger ones at a corresponding porosity [126]. In addition, other properties of porous ceramic materials such as thermal and electrical conductivities, thermal shock resistance, and gas permeability are significantly affected by the range of porosity. For example, porous ceramics with low porosity commonly provide better thermal conductivity than those

with high porosity [127] because those pores in the materials retain air leading to decreased thermal conductivity of the materials. Furthermore, the permeability of porous materials increases with increasing amounts of open pores in a structure [128]. It is, therefore, obvious that the properties of porous ceramics are influenced by their pore characteristics and microstructures. Because the pore features and microstructures of such materials are significantly induced by their processing techniques, the selection of a processing route significantly depends on the required porosity and microstructure of the ceramics for a particular application.

Until the present, a number of processing methods such as replica [120, 129, 130], templating [130-135], use of a pore-forming agent or additive [136, 137], starch consolidation casting [138, 139], sol-gel [140-142], and coating [143] have been employed to fabricate porous ceramics. Replica, use of a pore forming agent, and starch consolidation casting are the three well-known methods that are reviewed here.

2.3.1 Replica technique

The replica process is the most common approach for fabricating macroporous ceramics with pore sizes varying from 100 mm to 5 mm [144]. The method is a process that uses a polymeric sponge (typically polyurethane) as a cellular template to fabricate porous ceramic structures of variable pore sizes, porosities and chemical compositions. The macro-photograph and scanning electron photomicrograph of polyurethane (PU) are demonstrated in Fig. 2.12.

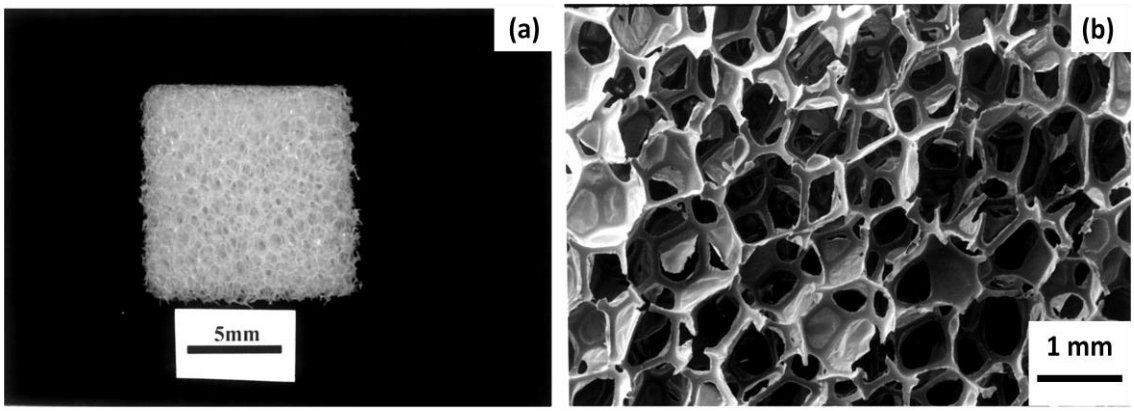

Figure 2.12 Macro-photograph (a) and scanning electron photomicrograph (b) of the polyurethane template (images reprinted from [130]).

This technique involves the impregnation of the sponge template with a ceramic slurry or precursor solutions, followed by a pyrolysing process to remove the template. Further heat treatment at a high temperature is used to sinter the ceramic. The process is shown in Fig. 2.13.

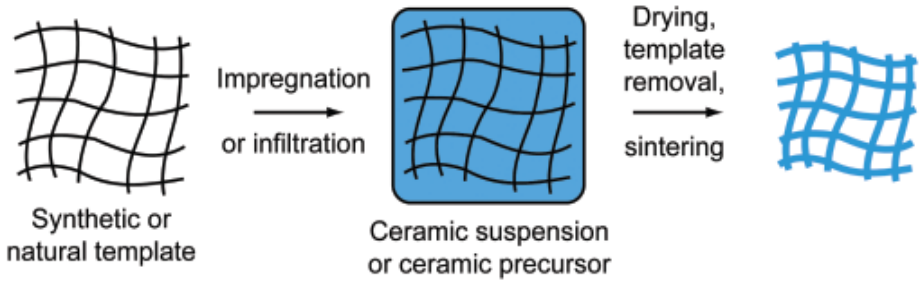

Figure 2.13 Scheme of the replica processing technique used for preparing macroporous ceramics (image taken from [122]).

The templates used for fabricating macroporous ceramics via this method can be either synthetic (i.e., polymer) or natural (i.e., wood) porous structures. The final product normally exhibits the same morphology as the starting porous template (Fig. 2.14a-b). However, macroporous ceramics produced by this method have

low strength and fracture toughness due to the presence of a hole in the centre of the struts (Fig. 2.14c), and cracking in these ceramics after the burning-out of the polymer substrate and thus limits their structural applications [18, 19]. Moreover, high processing temperatures (>1450 °C) are normally involved in this processing technique to sinter the ceramic products.

A number of macroporous ceramics have been produced via this route. For instance, Gao et al. [129] prepared TiC-Ti open-cell foams by repeatedly coating polyurethane (PU) foam with a mixed solution of TiH_2 and phenolic resin, followed by thermal pyrolysis at 800 °C for 2 hours and high frequency induction heating at 1650 °C. Nangrejo et al. [130] fabricated SiC-TiC composite foams using polyurethane (PU) foams as cellular templates. The PU foams were dipped into a polysilane solution (used as a SiC precursor) mixed with TiC powder, followed by pyrolysis at 900 °C in a nitrogen atmosphere and further heated at 1600 °C to obtain SiC-TiC composite foams. Porous TiC ceramics with wood-like structures were synthesised at 1400 °C via tetrabutyl titanate vacuum-infiltration using wood as a template and carbon source [133]. The final product produced by this technique, however, contained oxide impurities.

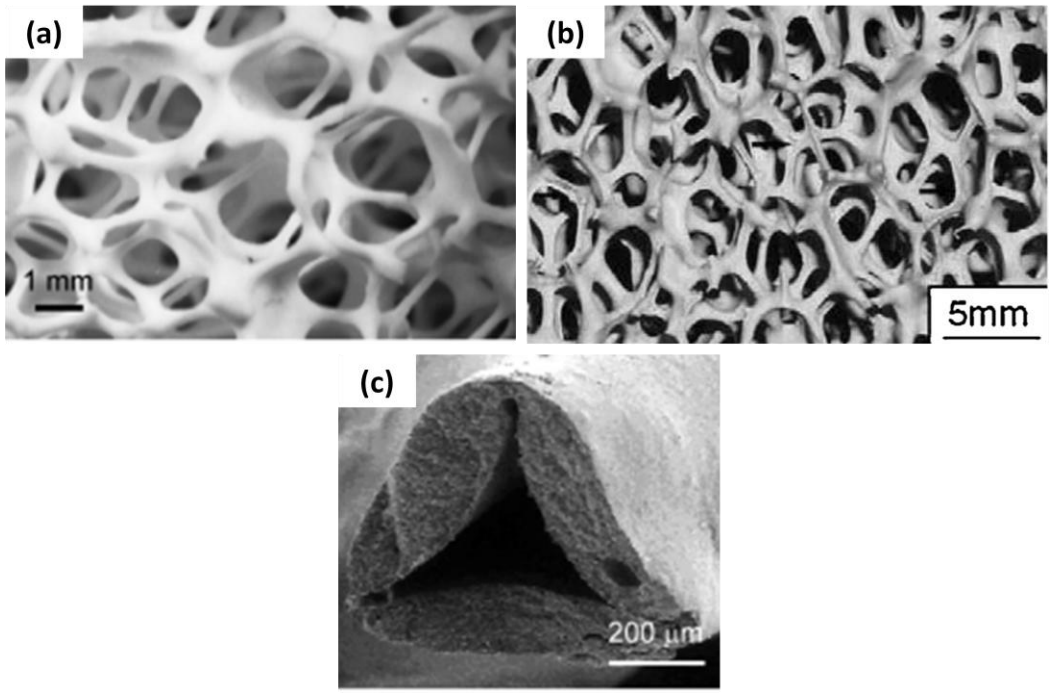

Figure 2.14 SEM images of macroporous ceramics produced using the replica technique with PU sponge templates. (a) Alumina-based open-cell structure [145], (b) SiC foams [117] and (c) detail of a strut of a cellular ceramic fabricated from a polymeric sponge, demonstrating the typical hole at its centre formed upon pyrolysis of the organic template [146] (images reprinted from [117, 145, 146]).

2.3.2 Additive-gas forming agent

The direct-foaming method is a process by which porous ceramic materials are fabricated through the incorporation of air or a gaseous phase into a ceramic suspension. The suspension normally consists of ceramic powder, solvent, dispersants, surfactants, a polymeric binder, and gelling agents, which is subsequently set to maintain the structure of the air or gaseous phase generated, as shown in Fig. 2.15. The formed foams are then sintered at elevated temperatures to obtain high-strength porous ceramic structures. The introduction of the gaseous phase can be performed by either mechanical

frothing, injection of a gas stream, gas-releasing chemical reactions, or solvent evaporation. Because this process is a direct introduction of a gaseous phase into the liquid medium, the total porosity of the final product produced by this technique is proportional to the amount of the gas incorporated into the suspension during the foaming process. The pore size formed by this route is strongly influenced by the stability of the wet foam before setting. This method, however, suffers from the phenomenon of rapid bubble growth before the setting takes place, resulting not only in large bubble diameters ranging from 30 μm to 1 mm but also in a wide distribution of the bubble sizes. This processing route is therefore particularly suitable for producing porous materials with porosities ranging from 45 to 97 vol% and pore sizes between 30 μm and 1 mm [20]. To overcome the rapid bubble growth during foaming process, additives are often added to the liquid medium to activate the setting reaction of the foam structure right after gas incorporation [122].

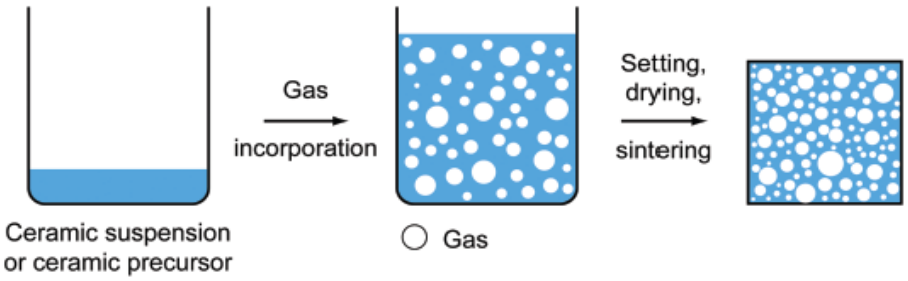

Figure 2.15 Scheme of the direct foaming technique used for preparing macroporous ceramics (image taken from [122]).

Sepulveda and Binner [147] synthesised highly porous ceramics via the direct-foaming technique using surfactants as stabilisers of the wet foams. The cell sizes were strongly influenced by both the density of the prepared specimen and the onset time of the polymerisation process. The obtained cell sizes were within the

range of 30 to 600 μm. Gonzenbach et al. [20] fabricated macroporous ceramics (Fig. 2.16) via the direct-foaming method by using particles instead of surfactants to stabilise the wet foams and prevent coarsening of the bubbles during the drying and sintering processes. The cell sizes produced by this method were in the range of 10 to 300 μm.

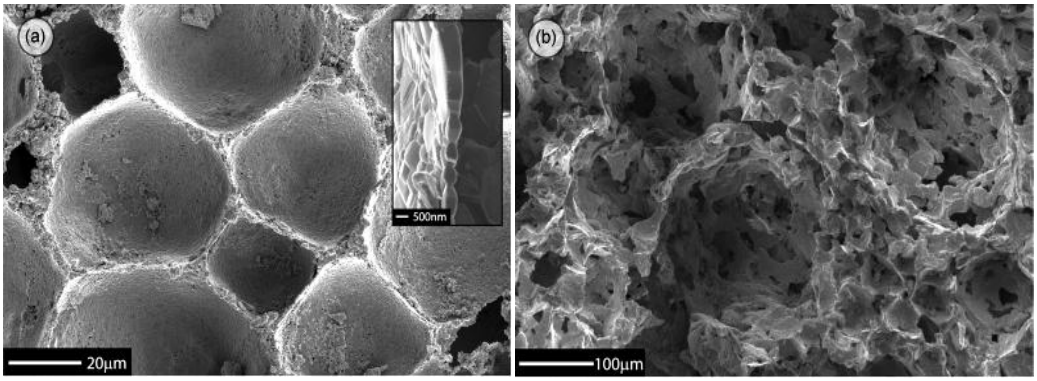

Figure 2.16 Microstructures of (a) a closed-cell particle stabilised foam and (b) an open-cell particle stabilised foam synthesised via the in-situ polymerisation of monomers shortly after air incorporation (images reprinted from [20]).

2.3.3 Starch consolidation casting

Starch consolidation is a process in which starch is used as a pore-forming agent in an aqueous suspension by swelling and gelatinising during casting in impermeable molds (normally metal molds). The molds are dried at a temperature range of 60-80 °C to generate ceramic green bodies prior to subsequent sintering of the green specimens at a high temperature to obtain porous ceramic materials. The major advantage of this method is that the pore size can be controlled without modifying either the sintering additives or the conditions but by selecting a suitable starch type [139]. Gregorová and Pabst [139] used corn starch in the concentration range of 20-50 vol% to produce porous alumina ceramics with porosities in the range of 22-53% via the starch

consolidation casting method. Khattab [138] also prepared porous alumina ceramics (Fig. 2.17) via this technique using different concentrations of corn starch. After drying, the green bodies were sintered at a high temperature range of 1400-1700 °C. The porosities of the sintered samples were between 46 and 64% and strongly depended on both the starch contents loaded into the precursor suspensions and the sintering temperature. At 1700 °C, the pore sizes of the samples increased with increasing concentrations of corn starch.

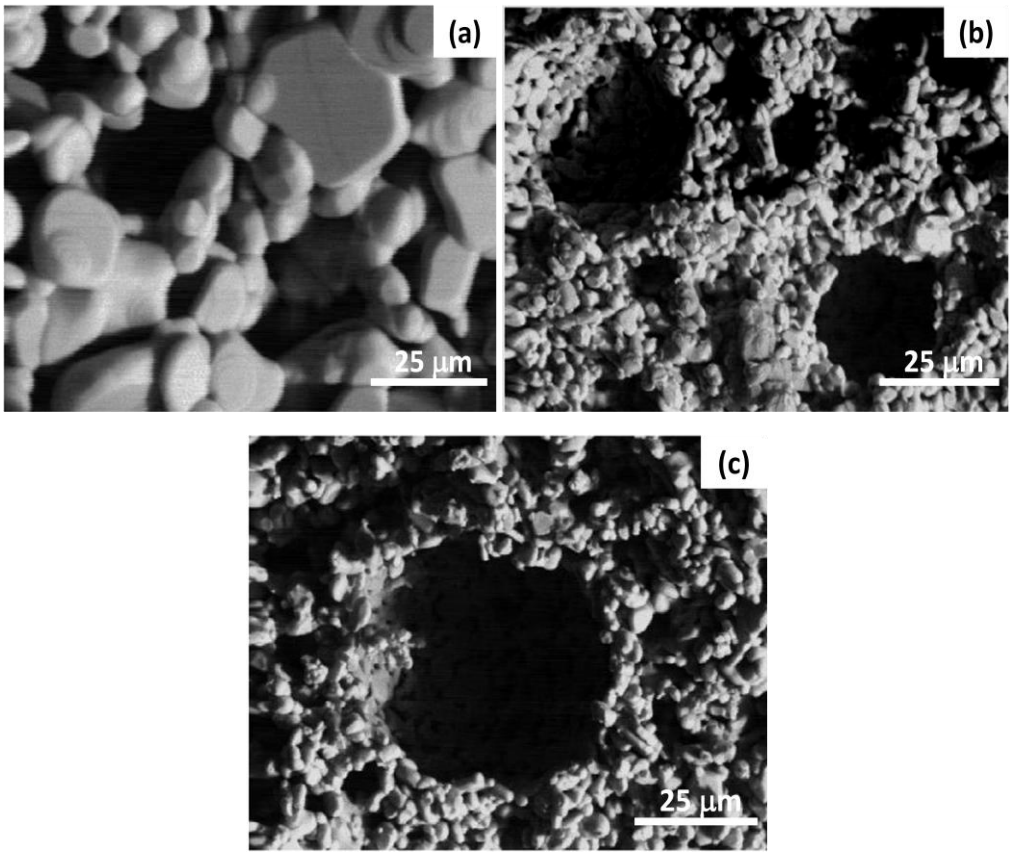

Figure 2.17 Microstructures of porous alumina samples produced via the starch cosolidation casting technique by sintering the samples at 1700 °C with (a) 3, (b) 8 and (c) 13 wt.% corn starch (images reprinted from [138]).

2.4 Molten Salt Synthesis (MSS) Technique

The term "molten salt" is defined as an ionic liquid matrix [148]. The molten salt compositions can be classified as single, binary, ternary and quaternary mixtures based on the number of salts used in the system, as displayed in Table 2.4.

Table 2.4: List of salt-type examples

Types	***Examples***
Single	KCl, NaCl, LiCl
Binary	NaCl+KCl, KCl+LiCl
Ternary	KCl+LiCl+KF
Quaternary	NaCl+KCl+LiCl+$CaCl_2$

Molten salt synthesis (MSS) is a well-established low-temperature synthesis technique that has received much interest in recent years for its potential use in fabricating a variety of materials such as carbides [149], oxides [150], aluminates [151], and titanates [152]. The key point of this synthesis technique is that a significant amount of water-soluble salt is added to the reactants and the mixture is heated above the melting point of the salt to gain a large amount of liquid phase in the synthesis system. The selected salt usually possesses a low melting point and provides a liquid phase at a relatively low temperature. The obtained liquid bath acts as a reaction solvent that defines the product characteristics (e.g., sizes, shapes). The given molten salt facilitates the dissolution of the reactants in the molten salt, leading to a homogeneous mixture and to increased contact opportunities between the reactants in the melt. In addition, the liquid medium provides easy routes for the dissolved species to transport through it, resulting in an increased diffusion rate of those species and thus the completion of reactions at a relatively low temperature and in a short reaction period.

2.4.1 Selection of Salts

To effectively process this technique, the selection of a salt is a crucial step for achieving a relatively low temperature synthesis and a high purity of the synthesised products. The basic criteria for choosing a salt as a reaction medium are listed below.

1) The salt is desired to be stable, readily available and inexpensive.
2) The suitable salt must not produce undesirable reactions with either the reactants or the products. This means that the salt only acts as a reaction medium.
3) The salt system must be easily removed by washing away with water during the process of salt removal or with hydrochloric acid during the process of purification.
4) Salts with low melting points are preferable for facilitating the dissolution of the reactants into the melt, resulting in a quicker rate of reaction. The lower the melting point of the salt is, the earlier the dissolution of the reactants in the melt becomes and, hence, the earlier the formation of the product phase occurs.
5) Salts with low viscosity at the reaction temperature are favoured to promote the diffusion rate of the reactant species in the melt. The lower the viscosity of the reaction medium is, the more rapid the species can transport.
6) The solubilities of the reactants in the molten salts also affect the formation rate of the product phase. The higher the solubility of the reactant in the melt is, the quicker the formation of the product phase becomes. It is noted here that the differences in the solubility of the reactants in the melt significantly influence the synthesis reaction mechanism. This is discussed below.

An example explaining the effects of these mentioned parameters is given here. Li et al. [153] synthesised $ZnAl_2O_4$ powders by reacting ZnO with Al_2O_3 powders in three different types of alkaline chlorides: LiCl, NaCl, and KCl. It was found that the formation of the product phase ($ZnAl_2O_4$) started at 700 °C in the molten LiCl while the phase began to form at 800 °C in the NaCl and KCl melts. This phenomenon was attributed to the effects of the melting points and viscosities of the molten salts as well as the solubilities of the reactants in the melt systems. LiCl possesses the lowest melting point of 610 °C compared with NaCl (801 °C) and KCl (771 °C). Furthermore, the viscosity of molten LiCl is 0.86 mPa·s at 800 °C [154], which is lower than those of NaCl (1.03 mPa·s) and KCl (1.02 mPa·s) [154, 155] at an identical temperature. The solubility of ZnO in the molten NaCl at 900 °C is 1.7×10^{-6} mol/g which is higher than the solubility in the molten KCl (9.1×10^{-7} mol/g) at an identical temperature. This resulted in a higher XRD intensity of the $ZnAl_2O_4$ peaks at 800 and 900 °C fabricated in the molten NaCl than in KCl melt at the same reaction temperature.

2.4.2 Synthesis Mechanism

Two main reaction mechanisms are usually involved in the MSS technique, which define the product's morphologies: template-growth and dissolution-precipitation. The relative dissolution rates of the reactants in the molten salt system determine the principal reaction mechanism. Li et al. [153, 156] and Kimura [157] clearly summarised the different characteristics of the two reaction mechanisms.

The dissolution-precipitation mechanism governs the synthesis formation when the dissolution rates of reactants A and B in the molten salt are comparable (Fig. 2.18a). Thus, both reactants are soluble to the molten salt, and the resultant

product precipitates in the melt under an extreme degree of supersaturation. The final product gained from this formation mechanism displays a different morphology than the starting materials. A typical example of the product formed via the dissolution-precipitation mechanism is the formation of rhombohedral $LaAlO_3$ powders (Fig. 2.19) that were synthesised by Li et al. [158] via the reaction of La_2O_3 with Al_2O_3 particles in a molten KF-KCl eutectic. The starting La_2O_3 and Al_2O_3 powders exhibited spherical-like morphologies with particle sizes of less than 1 μm, whereas the resultant $LaAlO_3$ product had a rhombohedral shape with a particle size of less than 3 μm. The totally different morphologies between the reactants and the synthesised powder was attributed to the effects of the dissolution-precipitation mechanism.

The template-growth mechanism is dominant when the dissolution rate of reactant A is significantly higher than that of reactant B. A dissolves in the molten salt and diffuses onto the surface of B (Fig. 2.18b) and B functions as the reaction template. The reaction subsequently takes place on the surface and forms the layer of product phase in situ (C) (Fig. 2.18b). The formed layer prevents the further dissolution of B. The dissolution of A in the melt increases with time (Fig. 2.18b) while the dissolution of B is prohibited by the product layer. More dissolved A diffuses deeper to the unreacted zone of B, thereby increasing the product layer. This phenomenon is repeatedly processed until the reaction is completed. Thus, the morphologies (shapes and sizes) of the synthesised product (C) obtained via the template growth reaction are similar to those of the less soluble reactant (B).

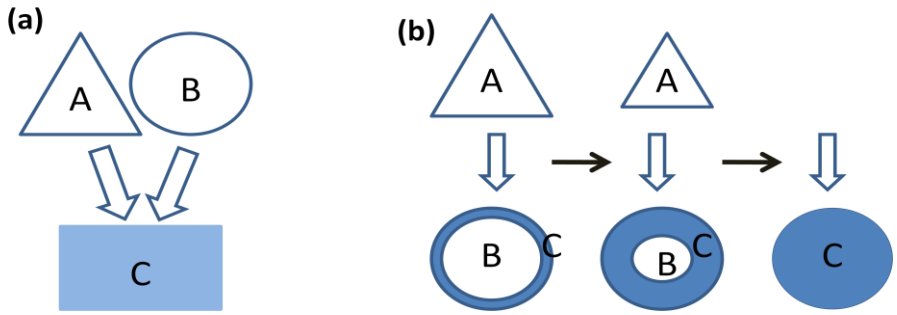

Figure 2.18 Schematic diagrams explaining the formation of product C from reactants A and B via (a) dissolution-precipitation and (b) template growth mechanisms (diagrams redrawn from [157]).

An example of this synthesis mechanism is the fabrication of magnesium aluminate spinel ($MgAl_2O_4$) powders produced via the reaction of MgO with Al_2O_3 particles in molten LiCl, KCl, and NaCl by Zhang et al. [151]. The product exhibited similar shapes and sizes to the starting Al_2O_3 powders (Fig. 2.20). When the morphology of the starting Al_2O_3 was changed from powder to microplatelet after reacting with MgO in the molten salts, $MgAl_2O_4$ platelets with well-preserved shapes and sizes of the starting Al_2O_3 (Fig. 2.21) were obtained [159]. Another example is that of titanium carbide nanofibres (Fig. 2.22), which were synthesised in a LiCl-KCl-KF molten system using carbon nanotubes and titanium powders as raw materials [160]. In those three studies, the synthesised products ($MgAl_2O_4$ powders and platelets, and TiC nanofibres) retained the original shapes and sizes of their starting materials, indicating that the template formation mechanism was dominant in these syntheses.

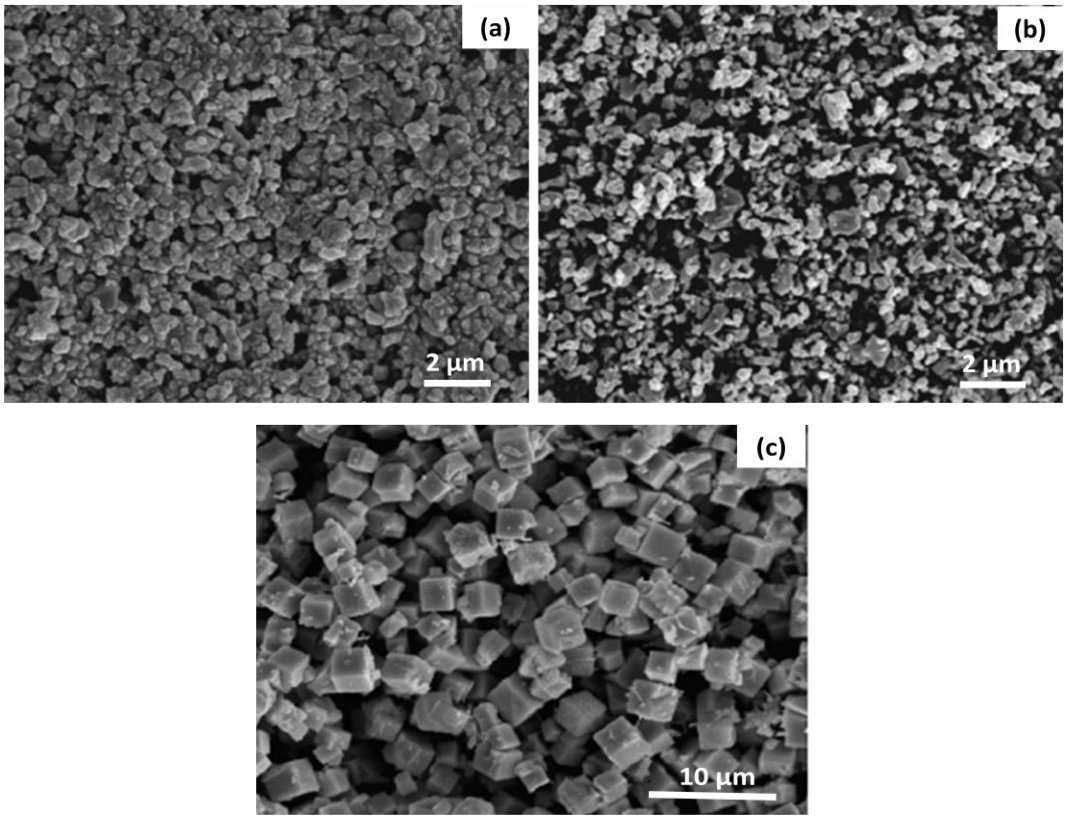

Figure 2.19 SEM images of raw materials (a) La_2O_3 and (b) Al_2O_3 powders and the $LaAlO_3$ particles produced (images reprinted from [158]).

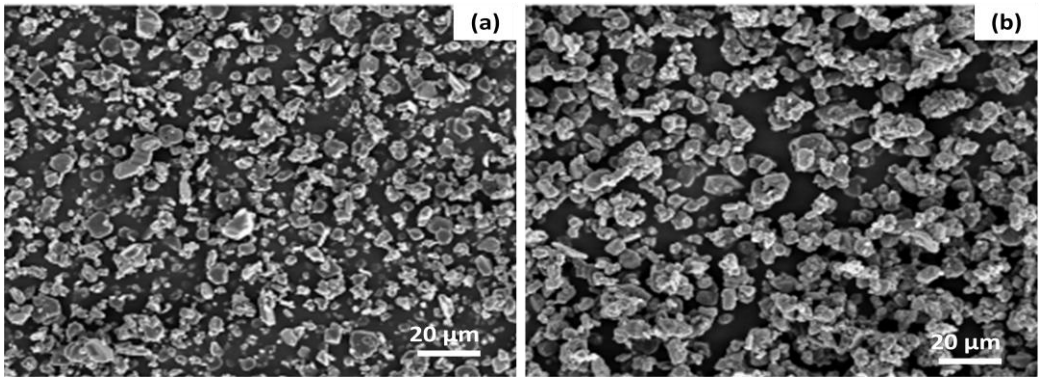

Figure 2.20 SEM images of (a) the Al_2O_3 powder used as raw material and (b) the $MgAl_2O_4$ particles produced (images reprinted from [151]).

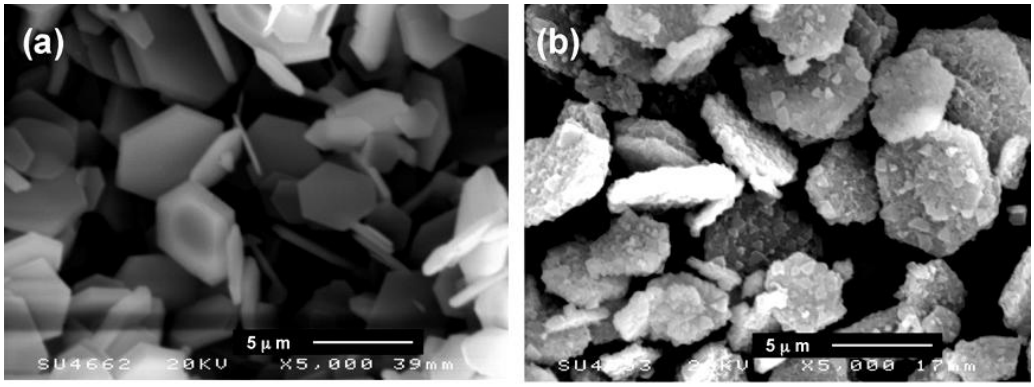

Figure 2.21 SEM images of (a) Al_2O_3 platelets used as the raw material and (b) the produced $MgAl_2O_4$ platelets (images reprinted from [159]).

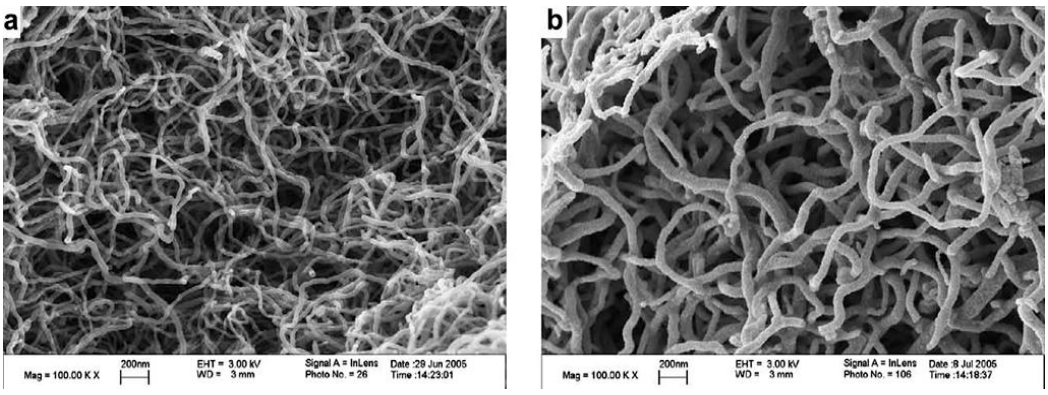

Figure 2.22 SEM images of (a) carbon nanotubes used as the raw material and (b) TiC nanofibres (images reprinted from [160]).

2.4.3 Advantages and disadvantages

A number of advantages of the MSS technique are highlighted as follows.

1) A wide range of precursors including cheap natural raw materials can be used as the reactants for the synthesis.
2) The presence of the molten bath enhances the reaction rate and hence considerably lowers the required temperature and time for the reaction.
3) The as-prepared powders have a high degree of homogeneity, are well dispersed and have high a surface reactivity, which promotes the densification process.
4) The particle shape and size of the final product can be easily controlled through the template-growth mechanism. This means that particular shapes (spheroidal, platelet, or lath/needle) and sizes (nano-scale to micro-scale) can be well defined.
5) The process is simple, practical, inexpensive and applicable for large scale production.
6) MSS can be applied in the fabrication of a wide range of materials, including those with complex shapes, which are difficult to synthesise by other processing methods.

It sould be noted that though the MSS technique provides various benefits, the process is limited due to some reasons. The typical processing temperature is usually less than or equal to 1100 °C because the heating temperature strongly affects the evaporation rate of the molten salt. Thus, if the temperature is too high (above 1100 °C), extreme evaporation of the molten salt is generated during the synthesis, resulting in an insufficient amount of reaction medium to facilitate the dissolution of reactants in the melt. Thus, incomplete reactions occur at particularly high synthesis temperatures. Likewise, long reaction times enhance the loss of molten salt to evaporation, leading to the requirement of a larger salt

concentration for the synthesis. Evaporation of the molten salt occurs upon heating, leading to the deposition of white powders on the furnace wall and particularly at the heating zone. Furnace cleaning should be applied afterwards, otherwise contamination may be introduced into the next firing samples.

Chapter Three

Characterisation Techniques

In this chapter, the scientific techniques employed in this work to characterise the samples are highlighted as follows.

3.1 X-ray diffraction (XRD)

X-ray diffraction (XRD) is a useful technique that uses X-rays diffraction to characterise the phase composition and measure the structural properties of a material. This technique gives an identical diffraction pattern for each phase contained in a substance no matter whether it is in the pure form or a mixture. In 1919, Hull [161] indicated that "every crystalline substance gives a pattern; the same substance always gives the same pattern; and in a mixture of substances each produces its pattern independently of the others." This characterisation method is therefore primarily used to identify phase compositions in a sample.

The most commonly used diffractometer is the para-focusing Bragg-Brentano instrument [162]. A typical Bragg-Brentano para-focusing powder diffractometer is shown in Fig. 3.1.

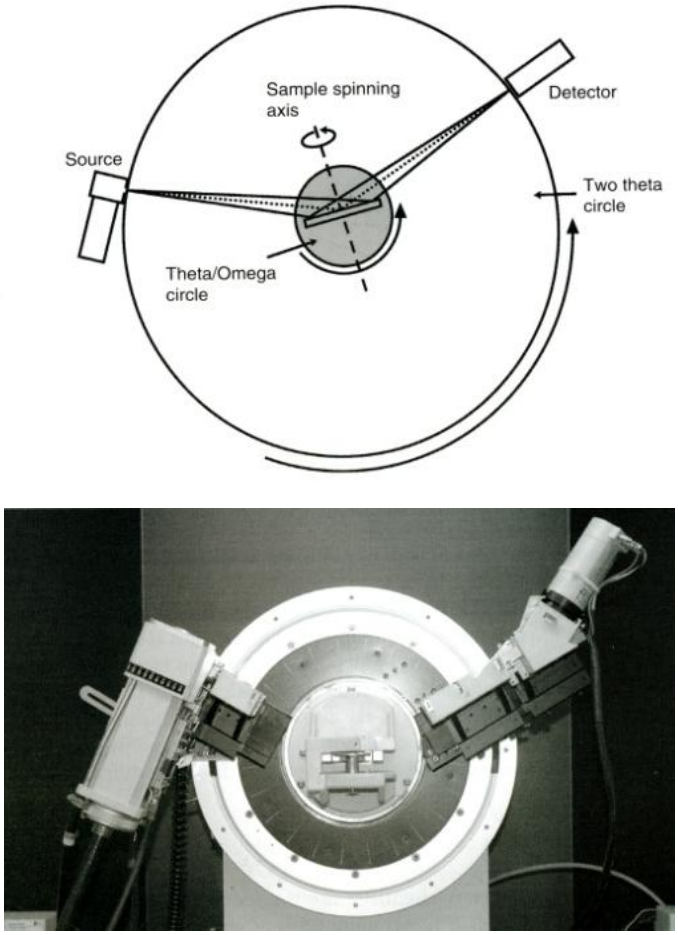

Figure 3.1 Schematic of a typical Bragg-Brentano para-focusing powder diffractometer (image obtained from [162]).

In XRD, a beam of x-rays with a typical wavelength is released from its source to strike the sample and is diffracted by the crystalline phases present in the sample according to Bragg's law:

$$\lambda = 2d\sin\theta$$

where d is the distance between the adjacent planes in the crystalline phase, λ is the wavelength of the X-ray beam and θ is the Bragg angle.

Apart from phase identification, structural parameters such as the inter-planar spacing (d_{hkl}) and lattice parameters (a, b and c) for each crystal structure can be estimated using Bragg's law. In addition, the average crystallite size of the sample can be measured via the XRD diffraction pattern using the Scherrer formula [75]:

$$D = \frac{0.9\lambda}{\beta \cos\theta}$$

where D is the average crystallite size, β is the broadening of the diffracted peak measured at half of the maximum intensity of the peak, θ is the Bragg angle, and λ is the wavelength of the X-ray beam. An example XRD curve is shown in Fig. 3.2.

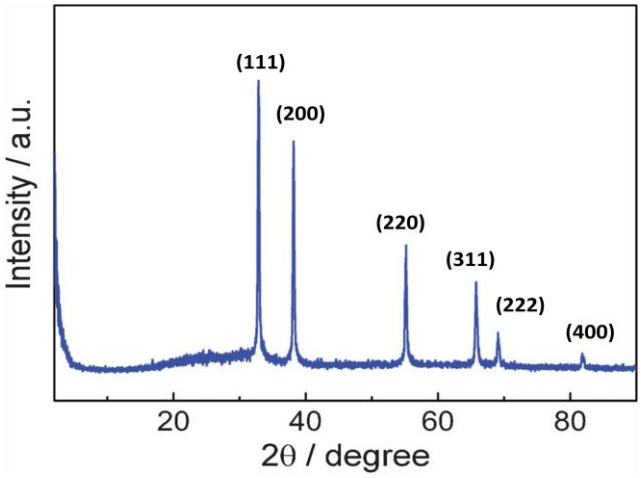

Figure 3.2 An XRD pattern of ZrC nanoparticles produced by pulsed plasma in liquid ethanol (data reprinted from [163]).

3.2 Scanning electron microscopy (SEM)

The scanning electron microscope (SEM) is a very useful tool for morphological examination. The information obtained from SEM observation is a microstructural image of the investigated specimen. The image is produced by scanning the sample's surface with a focused beam of high-energy electrons, as shown in Fig. 3.3. The electrons interact with atoms in the sample, generating a variety of signals such as secondary electrons (SE), backscattered electrons (BSE), cathodoluminescence (CL) and characteristic x-ray radiation at the surface of the sample. This is illustrated in Fig. 3.4. Those signals, which contain information about the sample's surface topography, morphology, and chemical composition as well as the orientation of materials making up the sample, can be detected by the detectors supported for those electron signals. A two-dimensional image is then generated according to the collecting signal type. An example for the secondary and backscattered electron image is shown in Fig. 3.5.

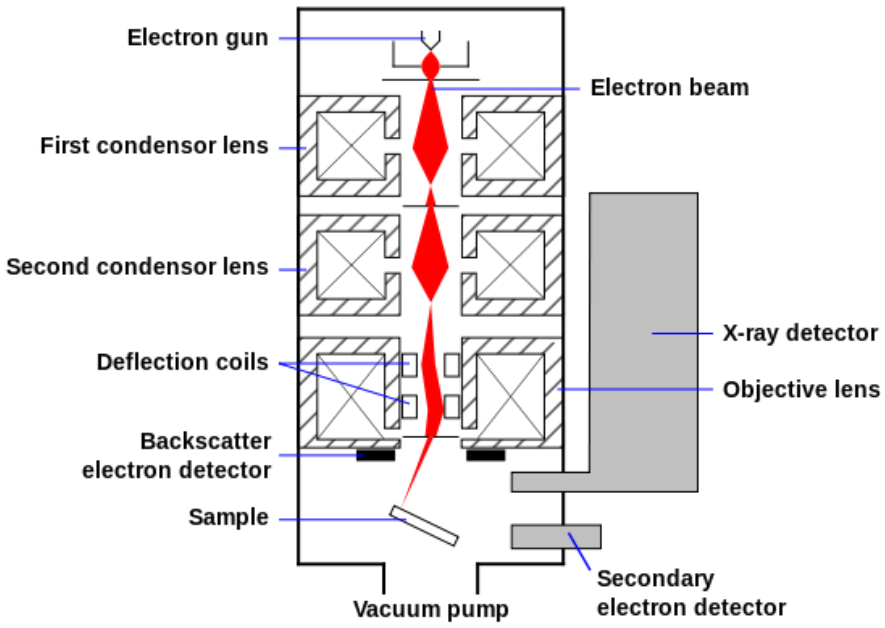

Figure. 3.3 Schematic representation the major components of a typical scanning electron microscope (image reprinted from [164]).

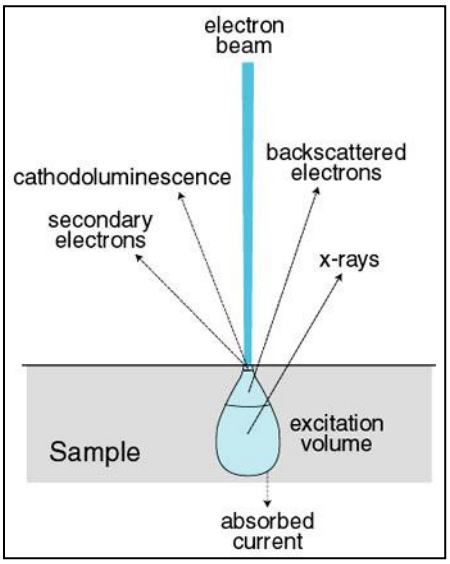

Figure 3.4 Various electron signals gained when the focused electron beam interacts with a surface sample (image reprinted from [165]).

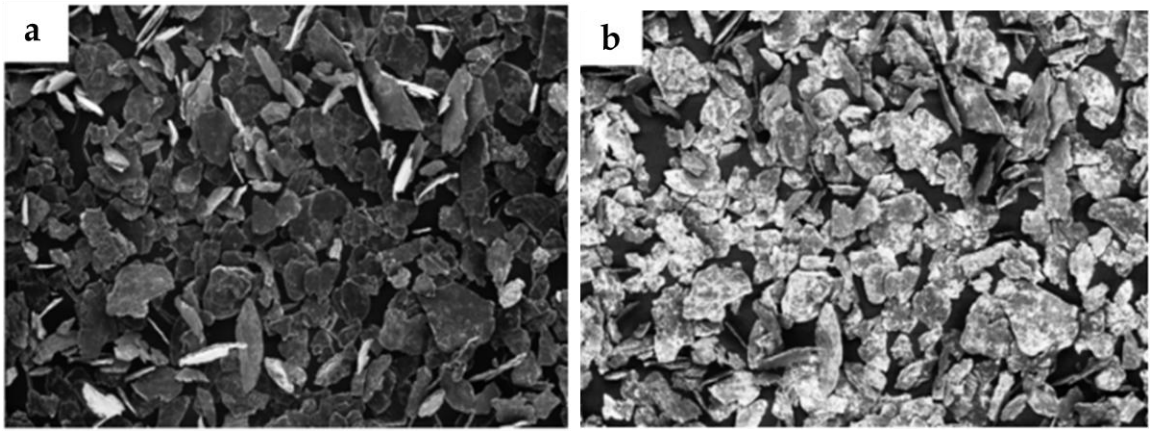

Figure 3.5 (a) Secondary electron image and (b) backscattered electron image of TiC-coated graphite (data reprinted from [166]).

3.3 Transmission electron microscopy (TEM)

To study the microstructure of a sample at a significantly high resolution, transmission electron microscope (TEM) is widely used. TEM is a microscopy

technique that operates on the same basic principles as the light microscope but employs a high-energy beam of electrons instead of light to reveal the microstructure of a sample at an atomic-level resolution. The similar functions of a basic TEM and an optical microscope are illustrated in Fig. 3.6.

A typical TEM consists of various main parts, including the source of the electron beam (electron gun), an electron lens, objective lenses, apertures, and a fluorescent screen or a CCD camera, as shown in Fig. 3.7.

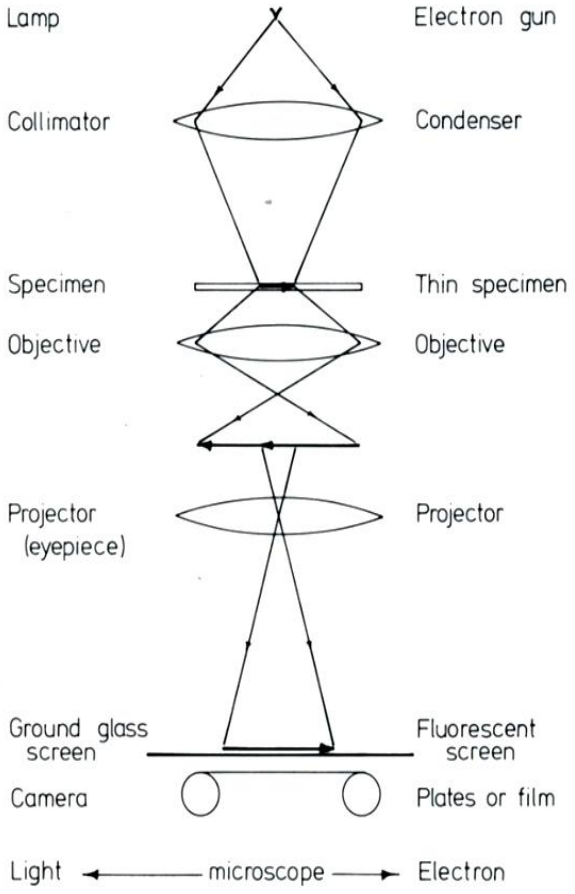

Figure 3.6 Schematic showing the main parts of a basic TEM. The operating system in light microscopy is demonstrated on the left. The equivalent terms in TEM are illustrated on the right (image reprinted from [167]).

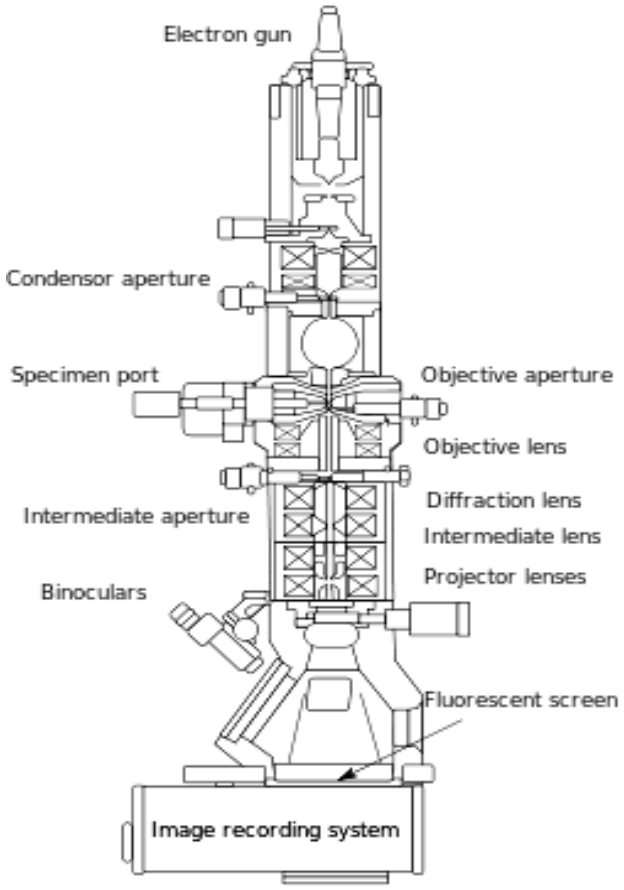

Figure 3.7 Schematic of a basic TEM instrument (image reprinted from [168]).

In TEM, electrons can be accelerated to several hundred kV (normally 100-400 kV). The higher the kV is, the better the resolution of the image becomes due to the decrease in the wavelength of the electrons to a wavelength of 0.0025 nm at 200 kV. Therefore, a much higher resolution can be obtained from TEM than from an optical microscope due to the limitations of the wavelength of light. In TEM, the accelerated beam is projected onto an ultrathin specimen (less than 200 nm) by means of the condenser lens system. The beam interacts with the specimen as it penetrates, and an image is generated from the interaction and displayed onto a fluorescent screen or a CCD camera.

When electrons interact with the thin specimen and pass through it, electron-scattering processes are performed as shown in Fig. 3.8. Such phenomena can be grouped into two major categories: elastic and inelastic scattering [169]. Elastic scattering represents the scattering with no energy loss of the beam after interaction with the specimen. This scattering type provides diffraction patterns of the evaluated sample. In contrast, inelastic scattering results in energy loss from the beam due to energy absorption caused by interactions between the primary electrons and the sample electrons.

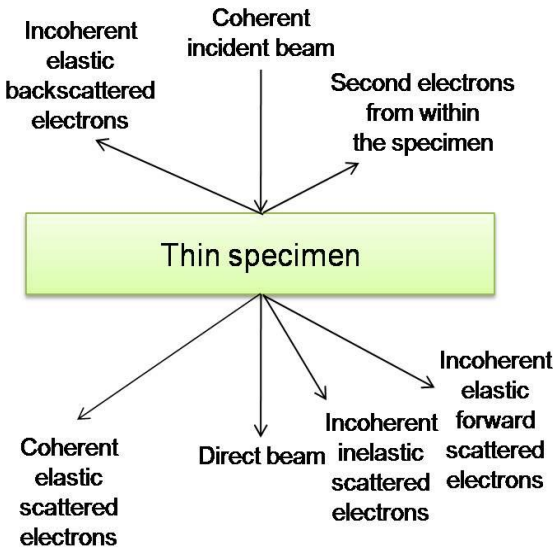

Figure 3.8 Schematic of elastic and inelastic scattered electrons gained from a thin specimen when the incident beam interacts with the sample (image reprinted from [169]).

Thus, TEM provides various types of information gained from the investigated sample such as morphology, stacking sequence, crystalline orientation, defects, dislocations, and diffraction patterns. To view the diffraction patterns of a sample, the working conditions can be simply switched from image viewing mode to diffraction pattern mode by changing the strength of the intermediate

lens. An example of morphologies, stacking sequences, and the selected area electron diffraction (SAED) pattern of a sample is demonstrated in Fig. 3.9.

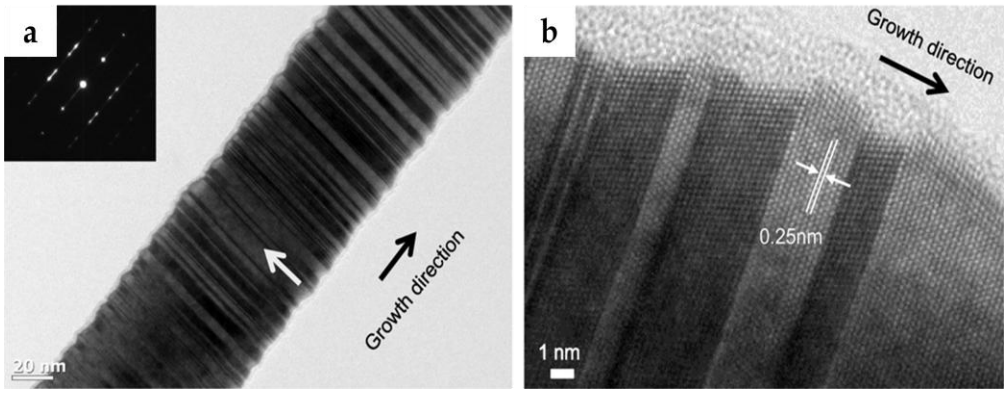

Figure 3.9 TEM images of the SiC nanofibre showing (a) the morphology of the fibre and (inset) the SAED of the fibre, and (b) the stacking sequences of the SiC fibre (data reprinted from [170]).

3.4 Energy Dispersive X-ray Spectroscopy (EDS)

EDS is an analytical technique used to analyse the elemental composition of a sample in which the instrument is normally coupled with SEM or TEM. This technique relies on an interaction of a high energy electron beam and a sample. Interaction of the primary beam with atoms in the sample results in shell transitions leading to the emission of an X-ray, as shown in Fig. 3.10. The emitted X-ray has an energy characteristic of the parent element, allowing the elemental composition of the sample to be measured by an energy-dispersive spectrometer.

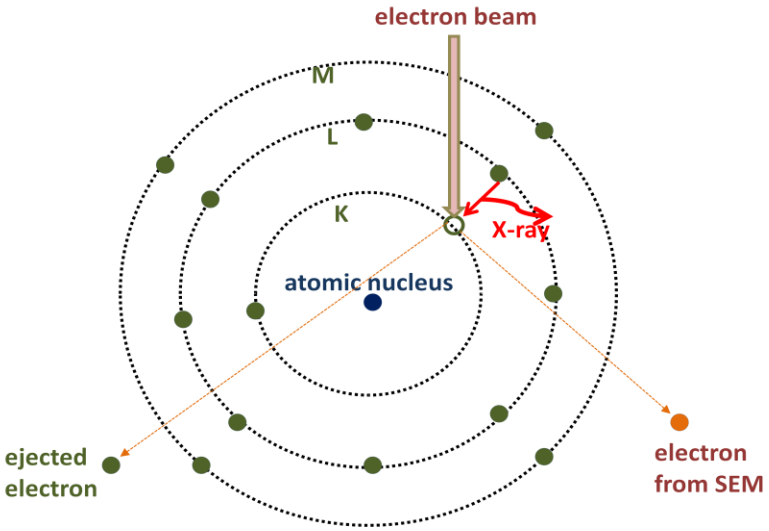

Figure 3.10 Schematic of the characteristic X-ray production.

EDS can provide a rapid qualitative or, with adequate standards, quantitative analysis of the elemental composition of a sample with a sampling depth of 1-2 μm. The analysis method may be performed in the form of point scans, line profiles, or maps, showing the elemental distribution of a sample surface. Examples of an EDS spectrum and mapping profile are shown in Figs. 3.11 and 3.12, respectively.

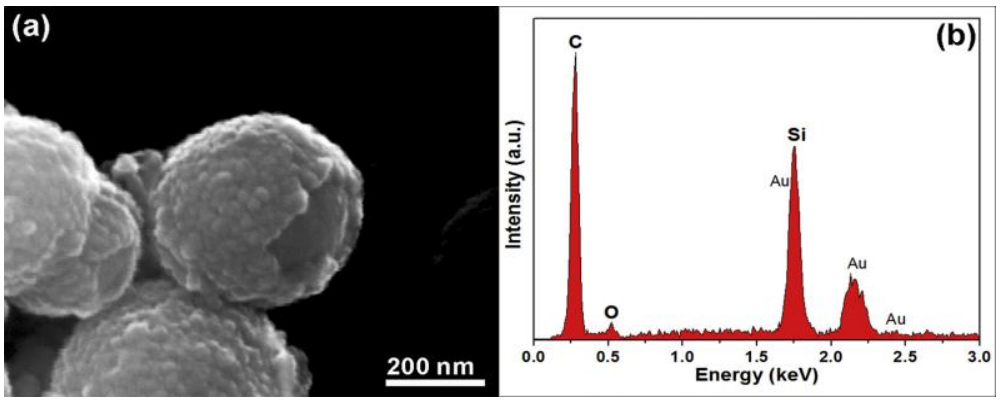

Figure 3.11 (a) SEM image of SiC-coated carbon black powders and (b) the corresponding EDS spectrum (data reprinted from [171]).

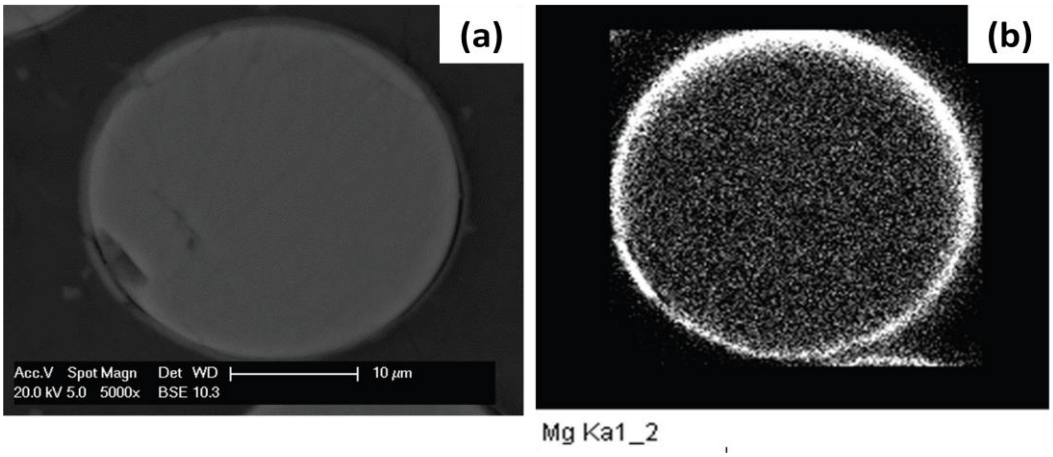

Figure 3.12 (a) SEM cross-sectional view of Mg coated fibre and (b) the corresponding Mg distribution observed using EDS in mapping mode (data reprinted from [172])

3.5 Raman spectroscopy

Raman scattering spectroscopy has become a popular analytical technique in materials characterisation and in biological and chemical sensing [173, 174] since the discovery of the Raman effect by Raman in 1922 [175]. Raman spectroscopy is a spectroscopic technique that allows for the detection and identification of the chemical bonds in a material through their unique vibrational and rotational energy level structures. Once the molecular vibrations of a material are excited, they start to absorb the energy of a particular frequency (wavelength). With the use of an excitation source, this absorption can be measured and represented as the characteristic vibration behaviours of different chemical bonds [176]. A monocromatic light such as a laser in the visible, near infrared, or near ultraviolet range is normally used as the light source of the instrument that excites the molecules in the investigated material. This is because a laser provides high intensity and the light can easily be focused in a small spot on the sample.

The laser interacts with molecules in the material, resulting in molecular vibrations, phonons or other excitations that occur through the inelastic scattering of photons, or Raman scattering. This interaction causes the laser energy to shift up or down depending on the vibrational state of the molecule under study, providing the vibrational modes of a system and hence the distinction of the chemical bonds present in the material. A schematic diagram of a typical Raman spectroscopy operation is shown in Fig. 3.13 and examples of Raman spectra are shown in Fig. 3.14.

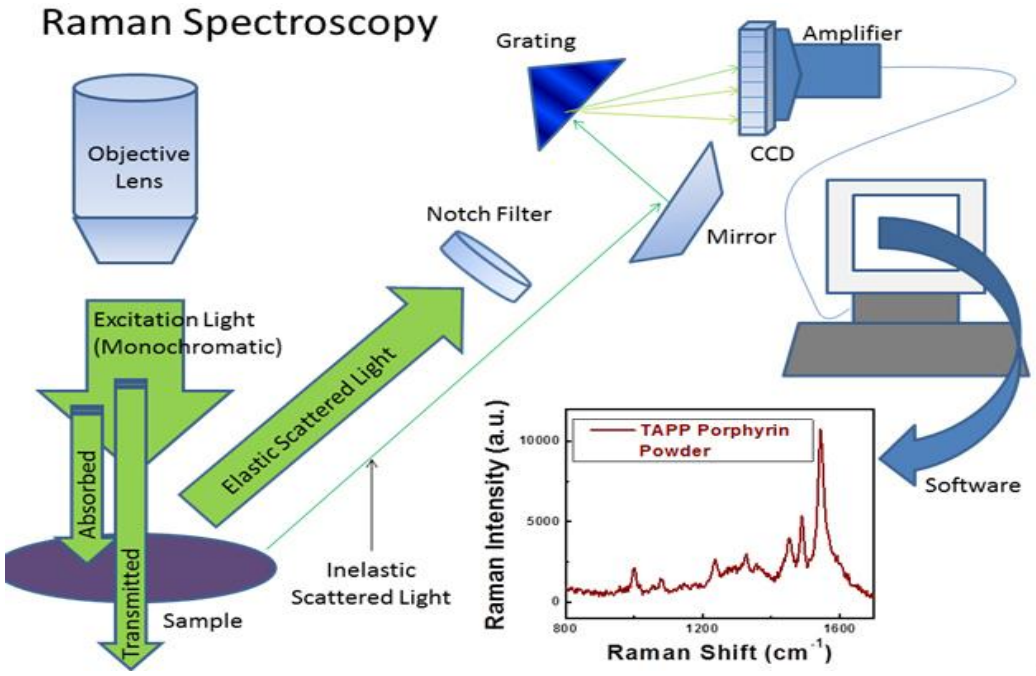

Figure 3.13 Schematic of a typical Raman spectroscopy operation.

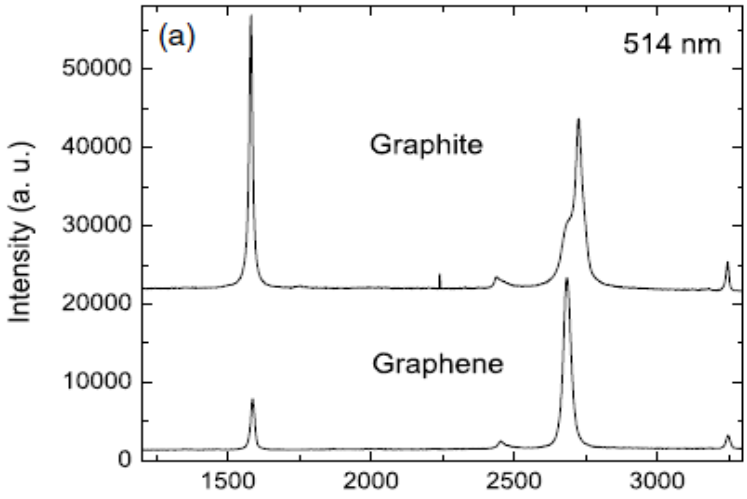

Figure 3.14 Raman spectra of graphite and graphene (data reprinted from [177]).

3.6 Differential thermal analysis (DTA)

The DTA is a simple and very popular thermal analysis technique for monitoring the endothermic and exothermic transitions of a sample as a function of temperature. The difference in temperature between the sample and a reference material (which undergoes no phase changes) is recorded against time or temperature while both materials are subjected to the same heating programme [178]. Figure 3.15 shows a block diagram of DTA reprensenting an overview of its fundamental operation. The temperatures of both the sample and reference material increase (or decrease) uniformly until the sample reaches a point at which it experiences a phase change. At this stage, whether the phase change is endothermic or exothermic and the differences in temperature are recorded. Various materials can be characterised using this instrument, including pharmaceuticals, food and biological materials, and organic or inorganic chemicals. Transitions measured include glass transitions, crystallisation, melting and sublimation. Figure 3.16 demonstrates an example DTA curve of an inorganic compound glass. The curve experienced both endothermic peaks, such

as the glass transition temperature (Tg), and exothermic peaks, such as the first onset of crystallisation above the Tg.

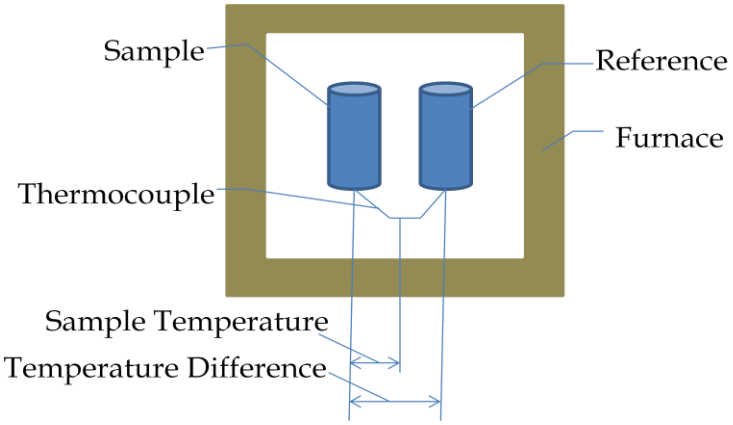

Figure 3.15 DTA block measuring system.

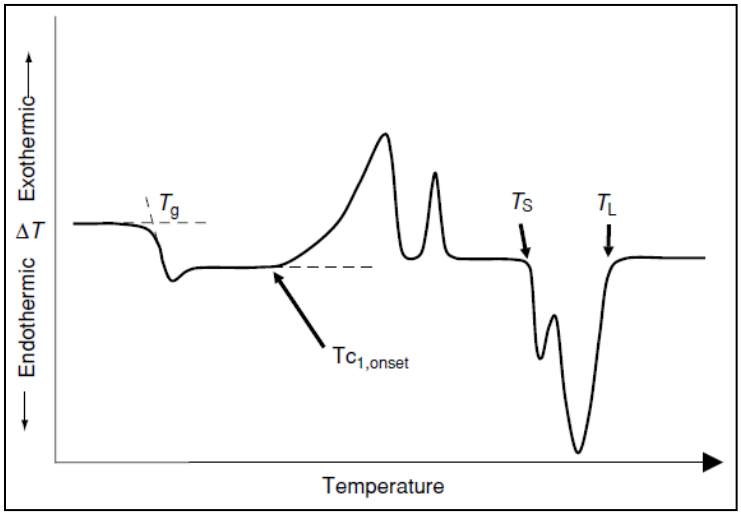

Figure. 3.16 Schematic of a typical DTA curve of an inorganic compound glass (data reprinted from [179]).

Chapter Four

Low Temperature Synthesis of ZrB_2 Powder Via Molten Salt Mediated Magnesiothermic Reduction

4.1 Introduction

As reviewed in Chapter two, because of its many excellent properties such as high melting point, high hardness, good thermal and electrical conductivities and excellent erosion and corrosion resistances, zirconium diboride (ZrB_2) is considered as an important candidate material for various applications, e.g., in thermal protection systems of hypersonic flights, rocket propulsion systems, cutting tools, refractory linings and metal treatment crucibles [2, 74, 80, 180]. A variety of synthesis techniques have been proposed to prepare ZrB_2 powders with different sizes and purity levels, including the conventional high temperature processing methods [62, 69, 70, 181-184], metallothermic reduction [2, 80, 85, 185], self-propagating-high-temperature synthesis (SHS) [14, 86, 186, 187], molten salt electrolysis [188], and sol-gel technique [53, 90, 92, 96, 189].

These techniques, however, suffered from a number of drawbacks such as high processing temperature, expensive raw materials, and heavy agglomeration and poor purity of the product powders. To overcome these, an alternative synthesis technique is therefore needed to be developed.

In the work presented in this Chapter, a novel molten-salt-mediated magnesiothermic reduction technique was developed, which leads to the fabrication of phase pure nano/submicron-sized ZrB_2 powder at a much lowered synthesis temperature. The effects of processing parameters (e.g. processing temperature and time) on the synthesis were examined, and the relevant reaction mechanisms discussed.

4.2 Experimental

4.2.1 Raw materials

Zirconium dioxide (ZrO_2), sodium tetraborate ($Na_2B_4O_7$), metallic magnesium (Mg), magnesium chloride ($MgCl_2$) and potassium chloride (KCl) were used as starting raw materials. All the chemicals used were supplied by Sigma Aldrich, UK. Some physical properties of the raw materials are given in Table 4.1.

Table 4.1: List of starting materials and some of their physical properties

Raw Materials	*Purity (%)*	*Particle size*	*Melting point (~℃)*
ZrO_2	99	300-400 nm	2700
$Na_2B_4O_7$	99	<200 μm	743
Mg	98	841-63 μm	650
$MgCl_2$	≥98	-	714
KCl	99	-	770

4.2.2 Sample preparation

The reactants (ZrO_2, $Na_2B_4O_7$, and Mg) in stoichiometric ratios indicated by reaction (4.1) or non-stoichiometric ratios (with 10-30 wt.% excessive Mg and/or $Na_2B_4O_7$) were mixed homogeneously using an agate mortar.

$$Na_2B_4O_7 + 2ZrO_2 + 10Mg = 2ZrB_2 + 10MgO + Na_2O \qquad (4.1)$$

The mixture was then combined with either $MgCl_2$ or KCl in the weight ratio of 1/4 prior to be contained in an alumina crucible covered with a lid and placed in an alumina tube furnace under a constant flow of argon. The furnace was then heated to a target temperature between 800 and 1200°C at 3°C/min and held for 3 h before being cooled down at the same rate to room temperature. The reacted mass was washed repeatedly with hot distilled water and then subjected to acid leaching with a dilute HCl solution to remove the residual salt and the by-product MgO. The final product powder was oven-dried overnight at 100 °C prior to further characterisation. The general flow chart for synthesising ZrB_2 powder is shown in Fig. 4.1.

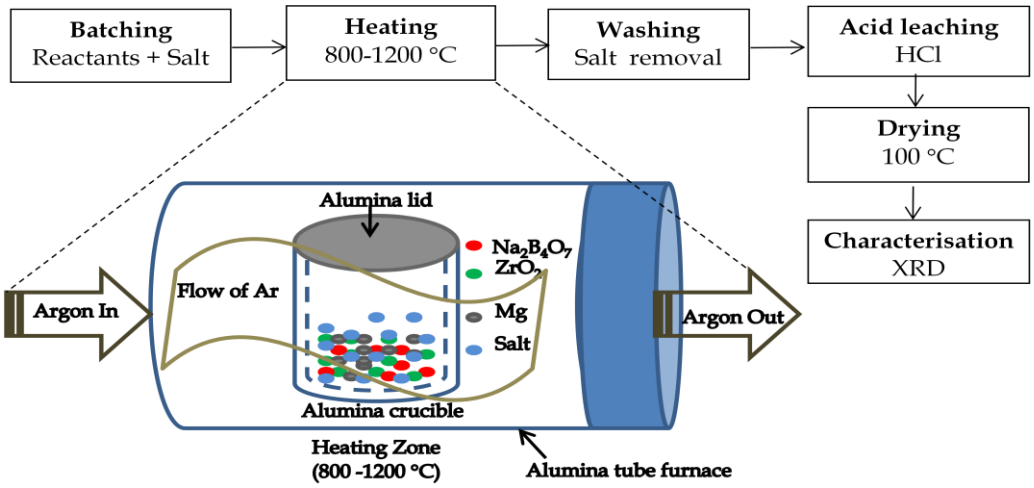

Figure 4.1 A flow chart of sample preparation procedure and schematic of a sample heating process in the tube furnace.

Phase compositions in as-prepared product powders were identified by powder X-ray diffraction (XRD) analysis (Siemens D500 reflection diffractometer). XRD patterns were recorded at 30 mA and 40 kV using Ni-filtered Cu Kα radiation. The scan rate was 2°/min with a step size of 0.05°. ICDD cards used for phase identification are ZrB_2 (65-8704), ZrO_2 (37-1484), MgO (65-476), $Mg(OH)_2$ (7-239) and $Mg_3B_2O_6$ (38-1475). Morphologies of as-prepared product powders were observed using a field emission gun scanning electron microscope (FESEM Inspect F). Purity levels of the synthesised ZrB_2 powder were also additionally investigated using Raman spectrometry (Renishaw In Via micro-Raman spectrometer). Thermodynamic predictions for possible reactions involved in the synthesis were made based on calculations of the Gibbs free energy changes (ΔG) corresponding to the relevant reactions at between 25 and 1200 °C using a software with an extensive thermochemical database (HSC chemistry 6.0, Outokumpu Research Oy, Finland).

4.2.3 Sample compositions and heating profiles for the ZrB_2 synthesis

All sample compositions and heating profiles are listed in Table 4.2. Those samples labelled as ZBK750, ZBMg750, ZBK800, and ZBMg800 were stoichiometrically produced to determine the effect of salt type on the ZrB_2 formation at 800 °C. Samples named as ZB800, ZB1000 and ZB1200 represented the samples heated in $MgCl_2$ for 3 h at 800, 1000, and 1200 °C, respectively, to evaluate the temperature-dependence of ZrB_2 formation. Samples labelled as ZB10Mg, ZB20Mg and ZB30Mg were non-stoichiometrically mixed samples prepared in $MgCl_2$ with 10, 20, and 30 wt.% excessive Mg, respectively, according to the mixing requirement of Reaction (4.1), and heated at 1200 °C for 3 h. The according samples were prepared to figure out the actual amount of Mg loss during the synthesis. Samples named as ZB20Mg10B, ZB20Mg20B and ZB20Mg30B were those contained 20 wt.% excessive Mg as well as 10, 20 and 30 wt.%, respectively, excessive $Na_2B_4O_7$, which were reacted in $MgCl_2$ at 1200 °C for 3h to find out the optimum amount of $Na_2B_4O_7$ required for completing Reaction (4.1). In addition, salt-free samples (ZB_800, ZB_1000 and ZB_20Mg30B) were prepared under identical batching conditions to those in the cases of salt-containing samples (ZB800, ZB1000 and ZB20Mg30B), and their reaction extents examined and compared with those in the case of salt-containing samples.

Table 4.2: List of sample compositions and heating profiles

Sample ID	*Mg excess (wt.%)*	*$Na_2B_4O_7$ excess (wt.%)*	*Raw materials used (g)*			*Salt type*	*Temperature (℃) x 3 h*
			ZrO_2	*$Na_2B_4O_7$*	*Mg*		
ZBK800	0	0	0.6161	0.5031	0.6076	KCl	800
ZBMg800	0	0	0.6161	0.5031	0.6076	$MgCl_2$	800
ZB800	0	0	0.6161	0.5031	0.6076	$MgCl_2$	800
ZB1000	0	0	0.6161	0.5031	0.6076	$MgCl_2$	1000
ZB1200	0	0	0.6161	0.5031	0.6076	$MgCl_2$	1200
ZB10Mg	10	0	0.6161	0.5031	0.6684	$MgCl_2$	1200
ZB20Mg	20	0	0.6161	0.5031	0.7292	$MgCl_2$	1200
ZB30Mg	30	0	0.6161	0.5031	0.7899	$MgCl_2$	1200
ZB20Mg10B	20	10	0.6161	0.5534	0.7292	$MgCl_2$	1200
ZB20Mg20B	20	20	0.6161	0.6037	0.7292	$MgCl_2$	1200
ZB20Mg30B	20	30	0.6161	0.6540	0.7292	$MgCl_2$	1200
ZB_800	0	0	0.6161	0.5031	0.6076	$MgCl_2$	800
ZB_1000	0	0	0.6161	0.5031	0.6076	$MgCl_2$	1000
ZB_20Mg30B	20	30	0.6161	0.6540	0.7292	$MgCl_2$	1200

4.3 Results and Discussion

4.3.1 Thermodynamic calculation

Based on the literatures [62, 80, 184], possible reactions which might involve during the synthesis are listed as follows:

$$Na_2B_4O_7 + 6Mg = 4B + Na_2O + 6MgO \quad (4.2)$$

$$ZrO_2 + 2Mg = Zr + 2MgO \quad (4.3)$$

$$Zr + 2B = ZrB_2 \quad (4.4)$$

$$3ZrO_2 + 10B = 3ZrB_2 + 2B_2O_3 \quad (4.5)$$

Gibbs free energy changes (ΔG) for the relevant reactions at 25-1200 °C are presented as a function of temperature (Fig. 4.2).

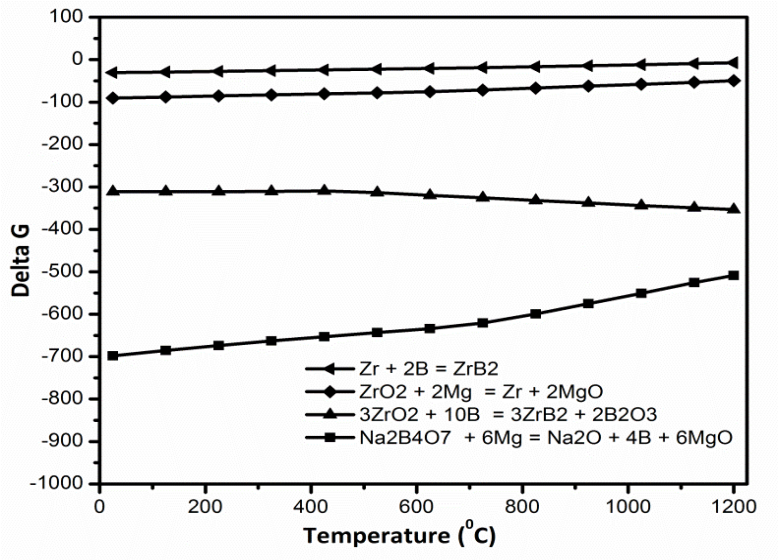

Figure 4.2 Changes of Gibbs free energy of the relevant reactions with temperature (°C).

As shown in Fig. 4.2, all listed reactions (4.2-4.5) are thermodynamically favorable at the observed temperature range due to their negative values of ΔG. Consequently, two possible reaction routes for ZrB_2 formation can be suggested. One is via reactions (4.2)-(4.4) and the other via reactions (4.2) and (4.5). The actual route will be discussed in more detail below, based on the experimental results.

4.3.2 Effect of salt type on the ZrB_2 formation

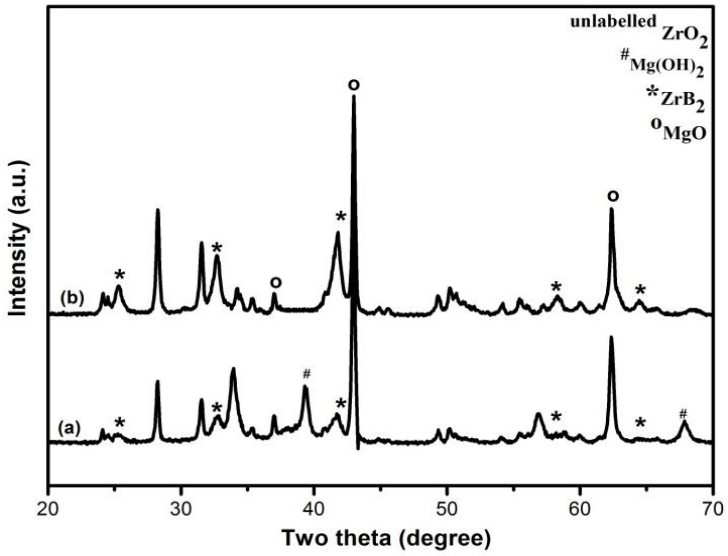

Figure 4.3 XRD of unleached powders after firing at 800 °C for 3 h in (a) KCl and (b) $MgCl_2$.

Figure 4.3 compares XRD curves obtained from the samples heated in KCl (Fig. 4.3a) and $MgCl_2$ (Fig. 4.3b) for 3 h at 800 °C. Although the formation of ZrB_2 was already evident in both samples, its peaks intensity in the sample fired in $MgCl_2$ was twice stronger than that in the sample heated in KCl. The findings demonstrated that $MgCl_2$ was a better reaction medium than KCl in enhancing the formation of ZrB_2. This could be caused by the solubility difference that solubility of Mg in $MgCl_2$ might be much higher than in KCl. Another reason could be due to the difference in melting temperature of the salts used ($MgCl_2$ melted at ~714 °C while KCl melted at ~770 °C). At ~714 °C, the reaction rate was greatly enhanced in the sample fired in $MgCl_2$ due to an easier transportation of the reacting species through the liquid medium and the increased contact opportunities between the reactants in the melt. Whereas, this prefered liquid

medium occured later at 770 °C in KCl system. Consequencely, higher peaks intensity of ZrB_2 is gained from the sample reacted in $MgCl_2$ salt (Fig. 4.3b).

4.3.3 Effect of processing temperature on the ZrB_2 formation

Figures. 4.4-4.5 show XRD of unleached and leached stoichiometric-composition samples after 3 h of heating at 800 to 1200 °C. Prior to leaching, a number of crystalline phases including ZrB_2, m-ZrO_2, MgO, $Mg_3B_2O_6$ were detected (Fig. 4.4). After the acid treatment, only MgO phase was leached out (Fig. 4.5), whereas others still remained, indicating that they were resistant to the dilute HCl solution.

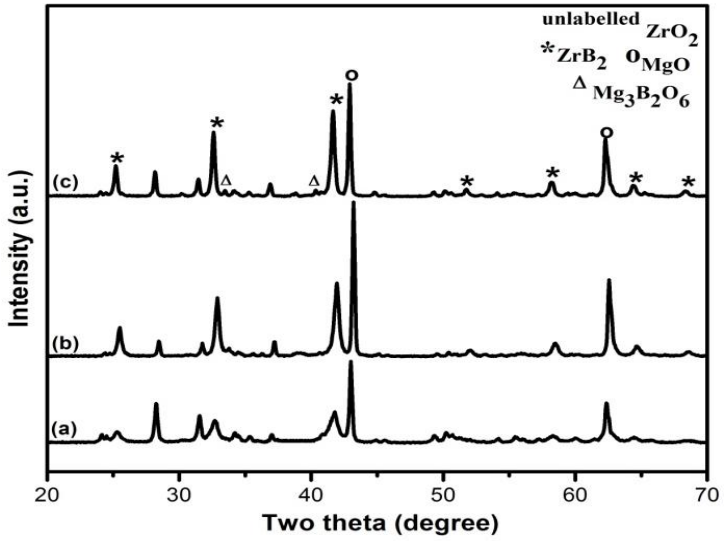

Figure 4.4 XRD of unleached powders stoichiometrically batched and heated for 3 h at (a) 800, (b) 1000, and (c) 1200 °C in Ar.

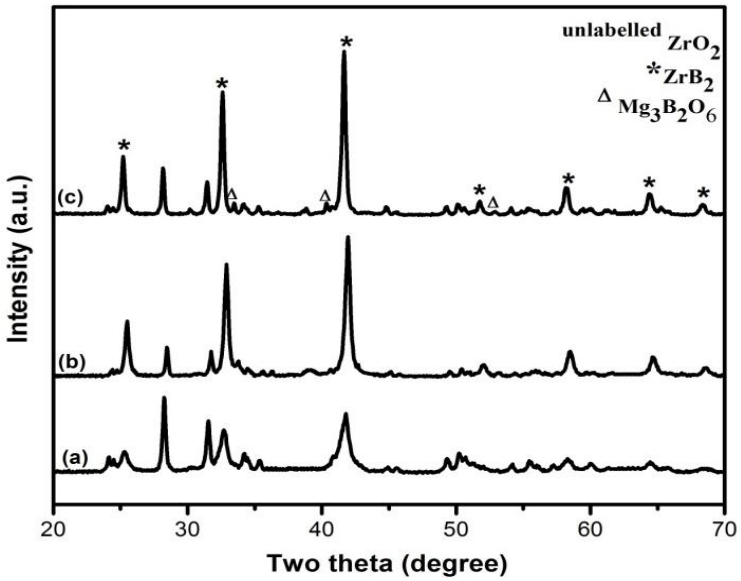

Figure 4.5 XRD of leached powders stoichiometrically batched and heated for 3 h at (a) 800, (b) 1000, and (c) 1200 °C in Ar.

As shown in Fig. 4.5, with increasing the temperature, the peaks width of ZrB_2 decreased along with its increased peaks intensity, indicating that the crystallinity and crystallite size of ZrB_2 increased with temperature [74, 190]. At the test temperature of 800 °C, the formation of ZrB_2 already became evident in the sample (Fig. 4.5a) but a significant amount of the unreacted ZrO_2 still remained. Upon increasing the temperature to 1000 °C, ZrB_2 peaks increased considerably, while ZrO_2 peaks decreased (Fig. 4.5b) suggesting the greatly enhanced reaction extent. At this temperature, minor $Mg_3B_2O_6$ was also observed. On further increasing the temperature to 1200 °C, ZrO_2 peaks became noticeably higher than at 1000 °C (Fig. 4.5c) revealing that the conversion from ZrO_2 to ZrB_2 was adversely affected by further increasing the temperature. This could result from the presence of insufficient Mg, for reducing $Na_2B_4O_7$ and ZrO_2, due to its evaporation loss at elevated temperatures [191]. Therefore, the actually lost amount of Mg was indirectly verified by XRD results shown in Fig. 4.6.

4.3.4 Effect of excessive Mg addition on the ZrB_2 formation

Figure 4.6 demonstrates XRD of samples containing various excessive Mg contents (0-30 wt.%) after heating at 1200 °C for 3 h. As shown in Fig. 4.6a-c, the peaks intensity of ZrB_2 increased, whereas those of ZrO_2 decreased evidently, with the increase in excessive Mg amounts from 0 to 20 wt.%. On further increasing the excessive amount to 30 wt.% (Fig. 4.6d), however, no further improvement in the reaction extent was seen. This might be due to some evaporation loss of B sources at the test temperature [192]. To prove this, excessive amounts of $Na_2B_4O_7$ along with 20 wt.% excessive Mg were applied, and the results are discussed in the next section (Fig. 4.7). Nevertheless, it was noticed that an intermediate $Mg_3B_2O_6$ phase was always left in the system no matter how much the excessive amounts of Mg were added. This suggested that excessive addition of Mg exhibited no obvious effect on the formation of $Mg_3B_2O_6$, which is in consistence with the study of Bilgi et al. [84].

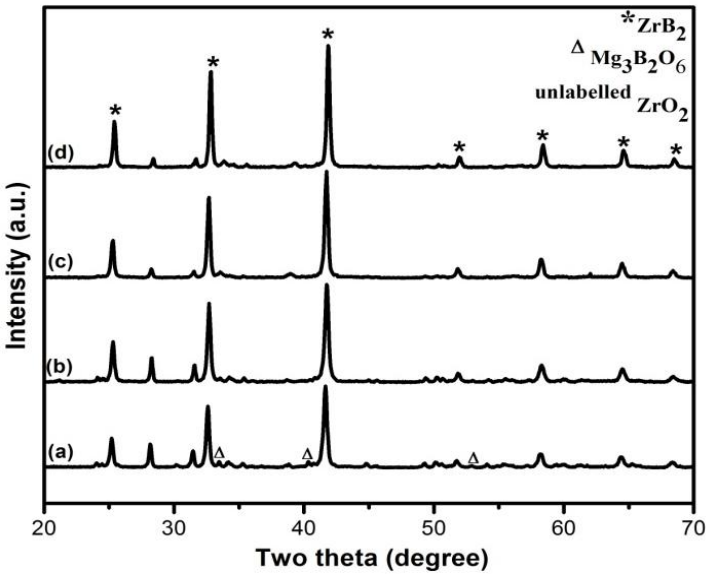

Figure 4.6 XRD of leached samples obtained from 3 h heating at 1200 °C of the batch powders with (a) 0, (b) 10, (c) 20 and (d) 30 wt.% excessive Mg.

4.3.5 Effect of excessing $Na_2B_4O_7$ addition on the ZrB_2 formation

As shown in Fig. 4.7, upon increasing the excessive amounts of $Na_2B_4O_7$ to 20 wt.%, $Mg_3B_2O_6$ became invisible, only ZrB_2 along with very minor ZrO_2 was detected. The finding showed that the formation of $Mg_3B_2O_6$ phase was related to the excessive addition of the boron source ($Na_2B_4O_7$). With further increasing the excessive amount to 30 wt.%, ZrO_2 peaks disappeared and only ZrB_2 was obtained as a final product powder.

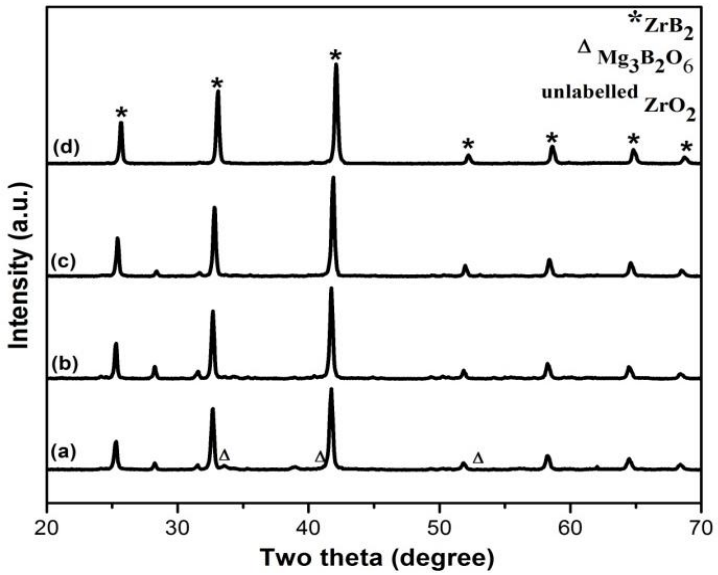

Figure 4.7 XRD of leached samples obtained from 3 h heating at 1200 °C of the batch powders with 20 wt.% excessive Mg and (a) 0, (b) 10, (c) 20 or (d) 30 wt.% excessive $Na_2B_4O_7$.

The seven peaks in Fig. 4.7d can be indexed as hexagonal ZrB_2 possessing diffraction planes (001), (100), (101), (002), (110), (102), and (111). The values of d-spacings and lattice parameters of the synthesised ZrB_2 powder were determined using the Bragg's law indicated by equations (4.1) and (4.2), respectively. The calculated lattice constants are a = 3.1525 and c = 3.5202 A which are in good agreement with a = 3.1687 and c = 3.5300 A of the ICDD card# 34-423.

$$d_{hkl} = \frac{n\lambda}{2(\sin\theta_{hkl})} \qquad (4.1)$$

$$\frac{1}{d^2} = \frac{4}{3}\frac{h^2 + hk + k^2}{a^2} + \frac{l^2}{c^2} \qquad (4.2)$$

where:

d is the d-spacing between te planes in the atomic lattice

a and c are lattice parameters

λ is the wavelength of incident wave

θ is the angle between the incident ray and the scattering planes.

4.3.6 Advantages of molten salt synthesis in the ZrB_2 fabrication

Here, the reaction extent produced by the conventional reduction and the MSS methods are compared between 800 and 1200 °C as shown in Figs. 4.8 and 4.9, respectively.

The formation of ZrB_2 became evident at 1000 °C (Fig. 4.8b) in the sample produced by conventional reduction route (salt-free), while it became apparent (Fig. 4.9a) at as low as 800 °C in the case of using MSS, indicating a significantly enhanced formation of ZrB_2 in the case of MSS. Although, the peaks intensity of ZrB_2 increased with the processing temperature in both synthesis routes, a large amount of unreacted ZrO_2 still remained in the sample fired via the conventional salt-free route, even at the temperature as high as 1200 °C (Fig. 4.8c) indicating that the reaction was far from the completion. On the other hand, with the same batch composition, phase pure ZrB_2 powder was achieved obtained at 1200 °C (Fig. 4.9c) when the reaction took place in the molten salt medium. Furthermore,

peaks intensity of the undesired $Mg_3B_2O_6$ increased considerably with the synthesis temperature in the salt-free system, whereas its formation was effectively inhibited by the MSS route at 1200 °C (Fig. 4.9c).

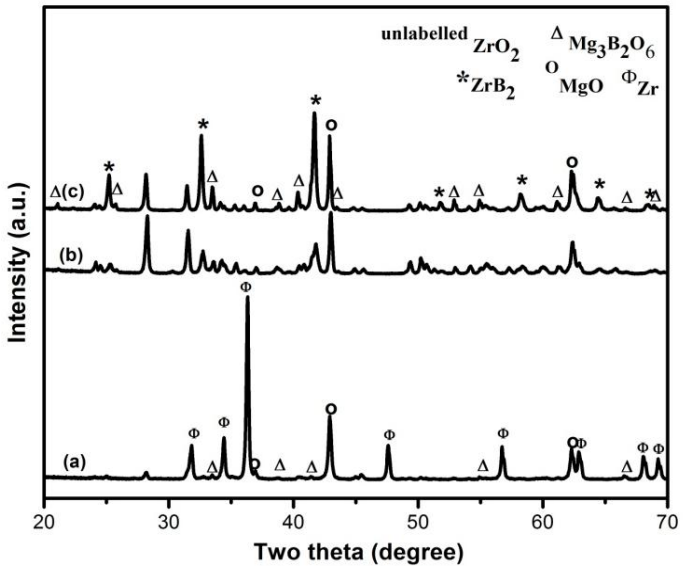

Figure 4.8 XRD of salt-free samples after 3 h of heating at (a) 800, (b) 1000 and (c) 1200 °C, respectively.

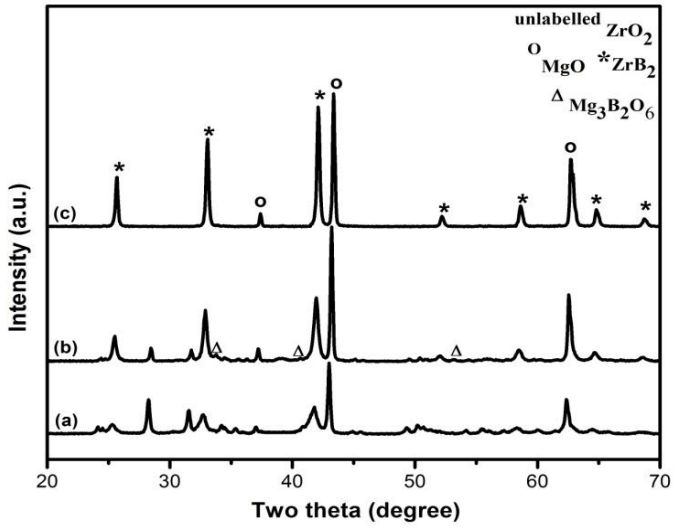

Figure 4.9 XRD of samples after 3 h of firing in $MgCl_2$ at (a) 800, (b) 1000 and (c) 1200 °C, respectively.

It is clear that the molten salt plays an important role in enhancing the formation of ZrB_2 and the reaction could be completed at a much lowered temperature than other processing techniques [69, 74, 90, 96, 181, 182, 186, 193, 194]. In addition, synthesis of high purity ZrB_2 product powder was achieved with the present MSS route, whereas some impurities still remained in the final product produced by other methods. For example, ZrB_2 powder was synthesised via volume combustion synthesis and mechanochemical process through the reaction system of ZrO_2-Mg-B_2O_3. Residual ZrO_2 and $Mg_3B_2O_6$ were remained in the final product even with excess additions of Mg and B_2O_3 [80]. ZrB_2 powder, containing residual Mg and ZrO_2 phases, was prepared via ZrO_2-Mg-B_2O_3 system at 1200 °C with the assistance of prolonged mechanochemical process [85]. ZrB_2 powder along with minor ZrO_2 and $B_{51}Zr$ phases was synthesised via the reaction system of ZrO_2-Mg-H_3BO_3 using double SHS technique [14].

4.3.7 Microstructural observations

Figure 4.10 illustrates microstructure of as-prepared ZrB_2 powder in comparison with that of the as-received ZrO_2 powder. The starting ZrO_2 particles displayed angular shapes with an averaged particle size of 300-400 nm (Fig. 4.10a). The synthesised ZrB_2 particles exhibited similar shapes and sizes of the original ZrO_2 powders (Fig. 4.10b) indicating a template growth mechanism of the product formation which is discussed in section 4.3.9.

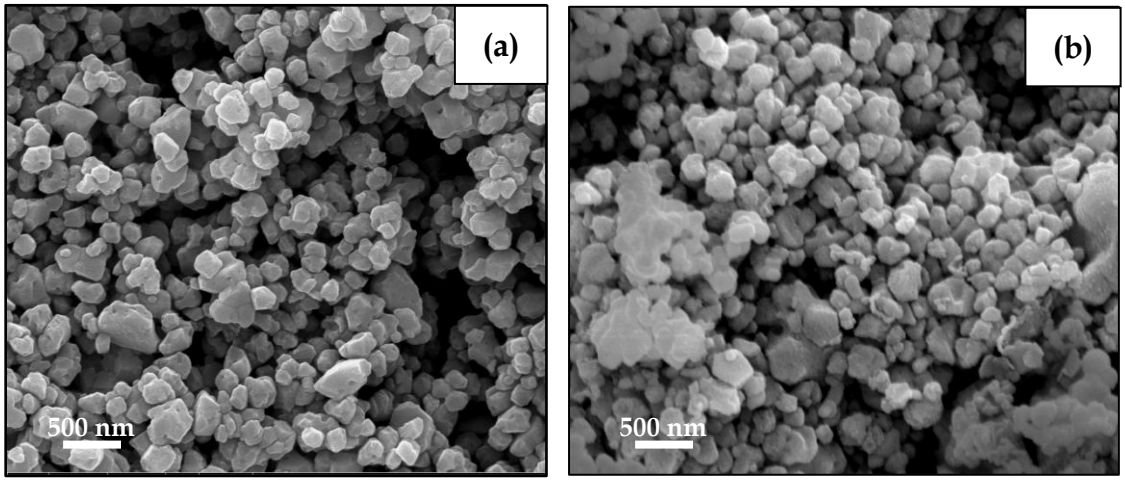

Figure 4.10 SEM images of: (a) the as-received ZrO_2 powder and (b) the as-prepared ZrB_2 powder after heating at 1200 °C for 3 h in Ar.

4.3.8 Raman spectrometry

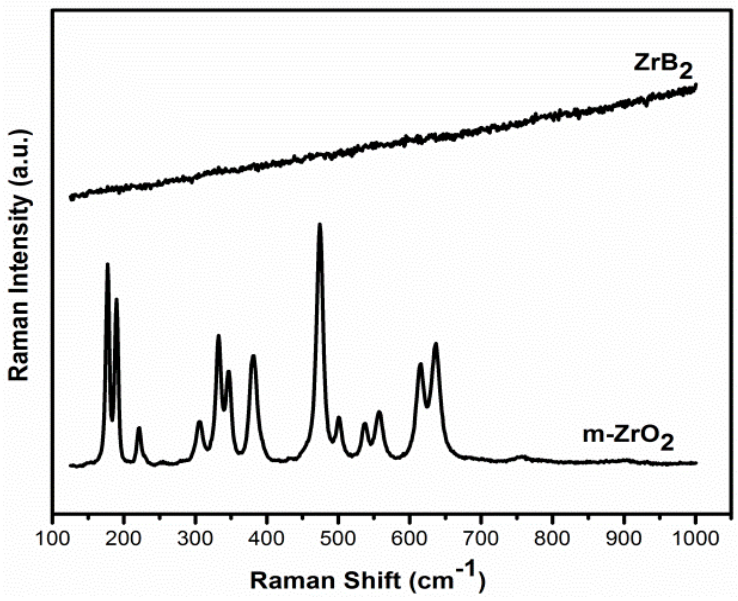

Figure 4.11 Raman spectra of the synthesised ZrB_2 and the as-received ZrO_2 powders

Figure 4.11 displays Raman spectra of the as-prepared ZrB_2 powder in comparison with that of the starting m-ZrO_2. The results show that the m-ZrO_2 powder was significantly active to Raman spectroscopy and exhibited strong Raman bands, while the as-prepared ZrB_2 powder was not and displayed non-Raman modes. The findings, therefore, confirmed that the as-prepared ZrB_2 was highly pure without containing unreacted ZrO_2 and other impurity phases. This is in good accordance with the studies of Zamora et al. and Li et al. [195, 196] that their as-prepared ZrB_2 powder exhibited very weak Raman peaks intensity and no obvious peaks presented.

4.4 Synthesis mechanism and further discussion

As mentioned above, the main reactions possibly involved in the synthesis process can be indicated by equations (4.2)-(4.5) [184, 187, 191, 197, 198].

Also, two possible reaction routes for the ZrB_2 synthesis can be proposed. One is via reactions (4.2)-(4.4) and the other is via reactions (4.2) and (4.5). The former route, however, would be possible if Zr was detected in the reacted samples. Otherwise, the latter route would be expected to dominate the ZrB_2 formation. The former reaction route was often proposed for the traditional magnesiothermic reduction process, based on the fact that Zr was detected in the samples [187]. However, Zr was not observed at any test temperatures in the MSS route. This seems to suggest that the first reaction mechanism might not be predominant in this case. Therefore, in the present study, the later reaction route is considered to be the principal reaction mechanism dominating the synthesis of ZrB_2, as further described below.

It is believed here that $MgCl_2$ only acted as a reaction medium at the test temperatures. An evidence supporting this is that the phenomenon of insufficient reducing agent (Mg) during synthesis at elevated temperatures and therefore the requirement in excessive addition of Mg powder (upto 20 wt.%) into the reaction system to compensate its lost amount at high temperatures. At the test temperatures, $MgCl_2$ melted itself at ~714°C producing large amount of liquid phase in the reaction system. In this liquid medium, Mg slightly dissolved [199] and then reduced $Na_2B_4O_7$ in the melt to generate amorphous B via reaction (4.2). The produced B also slightly dissolved in the molten salt [200, 201] and would diffuse rapidly through the liquid medium onto the surfaces of ZrO_2 particles and subsequently reduce ZrO_2 in-situ forming ZrB_2 particles via Reaction (4.5), which maintained shapes and sizes of the original ZrO_2 particles. Clearly, this is in well accordance with the microstructure observations shown in Fig. 4.10 that the as-prepared ZrB_2 exhibited similar shapes (angular) and sizes (300-400 nm) to the original ZrO_2 particles. The findings suggested that template growth was a dominant reaction mechanism responsible for the ZrB_2 formation and its morphologies, in which ZrO_2 particles had acted as the reaction templates.

The presence of the molten salt enhanced homogeneous mixing and mobility of the relevant species in the melt, which explained the accelerated reaction and the much lower synthesis temperature than used by most of the conventional ZrB_2 synthesis techniques. It also resulted in good dispersion of the final product powder (Fig. 4.10b). In addition, in the present work, the undesired $Mg_3B_2O_6$ phase, which is often formed by the conventional magnesiothermic reduction process and difficult to be removed, could be effectively avoided. This intermediate $Mg_3B_2O_6$ phase could be formed via the reaction of B_2O_3 with MgO [84, 202]. The effective avoidence of $Mg_3B_2O_6$ could be the advantage taken from

raw material ($Na_2B_4O_7$) selection. Magnesiothermic reduction for ZrB_2 synthesis was commonly processed via ZrO_2-Mg-B_2O_3 reaction system by previous studies [14, 70, 80, 189], whereas, in the present work, ZrB_2 was produced by ZrO_2-Mg-$Na_2B_4O_7$ instead. Because $Na_2B_4O_7$ was used as a boron source here, the generated Na_2O from reaction (4.2) would preferentially recombine with B_2O_3 formed from reaction (4.5) forming water-soluble $Na_2B_4O_7$ via reaction (4.6) and so the formation of an intermediate $Mg_3B_2O_6$ was avoided.

$$2B_2O_3 + Na_2O = Na_2B_4O_7 \qquad (4.6); \quad \Delta G^{\circ}_{298K} = -322.79\ \text{kJ/mol}$$

4.5 Conclusions

Phase pure ZrB_2 powder was synthesised in $MgCl_2$ at 1200 °C for 3 h using ZrO_2, $Na_2B_4O_7$ and Mg as the starting raw materials. In comparison with KCl, $MgCl_2$ was a better reaction medium for enhancing the formation of ZrB_2. By using appropriately excessive amounts of Mg (20 wt.%) and $Na_2B_4O_7$ (30 wt.%) to compensate their evaporated losses at 1200 °C, the conversion of ZrO_2 to ZrB_2 was completed and the formation of unwanted $Mg_3B_2O_6$ was effectively inhibited. SEM analysis revealed that the as-prepared ZrB_2 particles were generally well dispersed and their shapes (angular) and sizes (300-400 nm) were similar to those of the original ZrO_2 particles. The well preservation in shapes and sizes of the original ZrO_2 pariticles suggested that template growth mechanism governed the reaction synthesis. The overall reaction mechanism is proposed as follows. At the test temperatures, $MgCl_2$ and $Na_2B_4O_7$ interacted with each other forming a boro-chloride melt medium, in which Mg partially dissolved and reduced $Na_2B_4O_7$ homogeneously in the melt to generate amorphous B. The produced B, which also slightly dissolved in the melt, diffused through the melt to the surfaces of ZrO_2 particles and reacted to form ZrB_2 which retained shapes and sizes of the

original ZrO_2 particles. The presence of molten salt in the system is believed to have played an important role in reducing the synthesis temperature and providing good dispersion of the final product powder.

Chapter Five

Low Temperature Synthesis of Submicron And Nanosized ZrC Powders Via Molten Salt Mediated Magnesiothermic Reduction

---

5.1 Introduction

ZrC is one of the promising carbide materials applied extensively in ultra-high temperature areas, cutting tools, wear-resistant parts and nuclear insulation components due to its many excellent properties as reviewed in Chapter two. To fabricate its powders, many approaches have been reported to date including conventional thermal reduction techniques, self-propagating high-temperature synthesis (SHS), and sol-gel techniques. Unfortunately, they suffered from a number of drawbacks, for example, high processing temperature, coarse product grains, contaminations on the final product from the milling media, heavy

agglomoration of the product particles, expensive raw materials and complexity of the operating process.

In this chapter, a novel molten salt mediated magnesiothermic reduction has been developed to synthesise nano/submicron-sized ZrC particles at a much lowered temperature. The resultant ZrC powders were carefully characterised and the results, along with the relevant reaction mechanisms discussed.

5.2 Experimental

5.2.1 Raw materials

Zirconium dioxide (ZrO_2), carbon black, metallic magnesium (Mg), sodium chloride (NaCl) and potassium chloride (KCl) were used as starting raw materials. They were all supplied by Sigma Aldrich, UK. Some of their physical properties are listed in Table 5.1.

Table 5.1: List of starting materials and some of their physical properties

Raw Materials	*Purity (%)*	*Particle size*	*Melting point (℃)*
ZrO_2	99	300-400 nm, 30-50 nm	2700
*CB	99	~30 nm	**3550
Mg	98	841-63 μm	650
NaCl	99.5	-	801
KCl	99	-	770

Note: *CB refers to carbon black. **Melting point of carbon at 10 atm. Carbon does not melt when heated at stardard atmospheric pressure (1 atm).

5.2.2 Sample preparation

The reactants (ZrO_2, CB, and Mg) in the stoichiometric ratios indicated by reaction (5.1) or non-stoichiometric ratios (with 10-40 wt.% excessive Mg) were mixed homogeneously using an agate mortar. The mixture was then combined with either NaCl, KCl or a binary NaCl-KCl in the weight ratio of 1/8. The molar mixing ratio for the binary salt system used in this study was [NaCl]/([NaCl]+[KCl]) = 3/10. The resultant powder batch was contained in an alumina crucible covered with a lid and placed in an argon-protected alumina tube furnace. The furnace was heated to a given temperature between 650 and 950°C at 3°C/min and held for 6-8 h before being cooled down at the same rate to room temperature. The reacted mass was washed repeatedly with hot distilled water and then subjected to acid leaching in a dilute HCl solution to remove the residual salt and the by-products such as MgO and $Mg(OH)_2$. The formation of $Mg(OH)_2$ is explained later in the section of salt selection (5.3.3.1). The final product powder was oven-dried overnight at 100 °C prior to further characterisation. The general flow chart for synthesising ZrC powders is illustrated in Fig. 5.1.

$$ZrO_2 + C + 2Mg = ZrC + 2MgO \qquad (5.1)$$

To study melting behaviours of salts and assist identification of a proper temperature range for the synthesis process, differential thermal analysis (DTA, STD-Q600) of three stoichiometrically mixed samples containing NaCl, KCl, and NaCl-KCl, respectively, was carried out from room temperature to 1000 °C in a constant flow of argon at a heating rate of 10°/min. Phases in final product powders were identified by powder X-ray diffraction (XRD) analysis (Siemens D500 reflection diffractometer). Spectra were recorded at 30 mA and 40 kV using Ni-filtered Cu Kα radiation. The scan rate was 2°/min with a step size of 0.05°.

ICDD cards used for identification are ZrC (65-8835), ZrO_2 (37-1484), Zr (5-665), MgO (65-476), and $Mg(OH)_2$ (7-239). Morphologies of the final product powders were observed using a field emission gun scanning electron microscope (FESEM Inspect F). To better understand the reaction mechanisms, thermodynamic calculations for reactions possibly involved in the ZrC synthesis were also carried out by using the same software and database as used in the case of ZrB_2 synthesis (See Chapter 4).

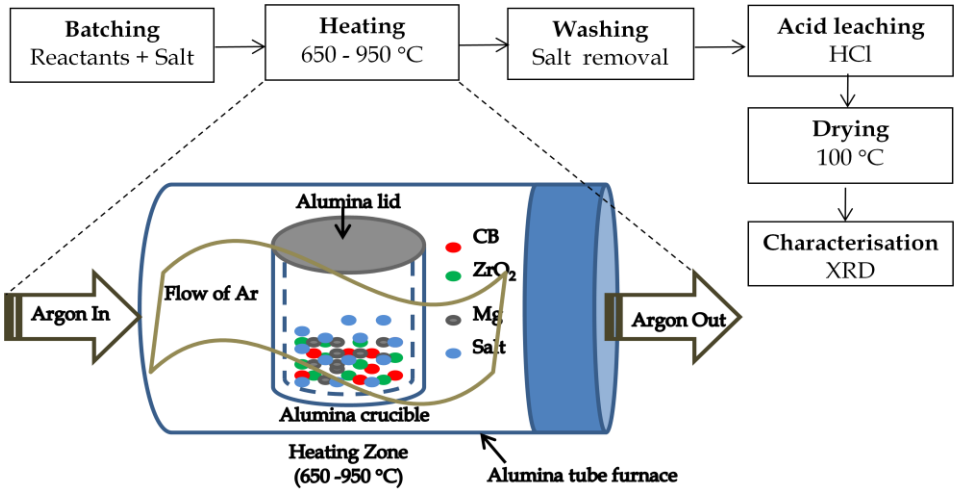

Figure 5.1 A flow chart of sample preparation and schematic of a sample heating process in the tube furnace.

5.2.3 Sample compositions and heating profiles for the ZrC synthesis

In the part of salt selection, because a binary NaCl-KCl was applied as a reaction medium for the synthesis, evaluation of an optimum mixing ratio between the two salts was performed. Six samples with different molar fractions of NaCl/(NaCl+KCl) were stoichiometrically prepared according to Table 5.2. In order to investigate the effect of processing temperature on the ZrC formation, five samples were stoichiometrically prepared and heated at a temperature from

650 to 950 °C for 8 h. The sample compositions and processing conditions are presented in Table 5.3. Apart from synthesis temperatures, holding time and excessive Mg contents were also studied. The dwell time for the synthesis was reduced from 8 to 6 h to study its effect on the ZrC formation. Because the conversion of ZrO_2 to ZrC is directly related to Mg concentrations in the reaction system, an appropriate compensation amount of the lost Mg due to different dwell time (6 and 8 h) was researched. Table 5.4 presents the sample compositions and heating conditions for optimising the Mg compensation contents at 950 °C for 8 and 6 h. Furthermore, to explore advantages of having a molten salt in the reaction system of ZrO_2-Mg-CB in comparison with carbothermal reduction and magnesiothermic reduction methods, two additional samples were prepared from coarse ZrO_2 and fine CB powders and heated for 8 h at 950 °C in a constant flow of argon. The sample for carbothermal reduction was prepared using carbon black and ZrO_2 as starting raw materials and NaCl-KCl as reaction medium. The other for magnesiothermic reduction was prepared without salt using CB, ZrO_2 and Mg as raw materials with 40 wt.% excessive Mg, according to the mixing requirement of Reaction (5.1) as illustrated in Table 5.5. When finer ZrO_2 particles were applied as a zirconium source for the synthesis, a lower processing temperature was expected. In order to investigate the effect of fine ZrO_2 particles on the ZrC formation, some samples were produced acccording to Tables 5.6 and 5.7. An optimum amount of evaporated Mg loss at 850 °C was evaluated by heating the samples (as shown in Table 5.7) containing variously excessive Mg contents (0-20 wt.%) at the test temperature for 8 h in the environment of argon.

Table 5.2: List of sample compositions and heating profiles for selecting a proper molar ratio of NaCl/([NaCl+KCl]).

Sample ID	*[NaCl]/ ([NaCl]+[KCl]) (molar ratio)*	*Raw materials used (g)*			*Excessive Mg (wt.%)*	*Heating profiles (℃ x h)*
		*ZrO_2 (*Coarse)*	*CB (**Fine)*	**Mg**		
NaK0	0	0.6161	0.0600	0.2430	0	900x8
NaK0.1	0.1	0.6161	0.0600	0.2430	0	900x8
NaK0.3	0.3	0.6161	0.0600	0.2430	0	900x8
NaK0.5	0.5	0.6161	0.0600	0.2430	0	900x8
NaK0.7	0.7	0.6161	0.0600	0.2430	0	900x8
NaK01	1	0.6161	0.0600	0.2430	0	900x8

Note: *Coarse represents the starting particle size of ~300-400 nm. **Fine refers to the original grain size of ~30 nm.

Table 5.3: List of sample compositions and heating profiles for investigating the effect of processing temperatures.

Sample ID	*[NaCl]/ ([NaCl]+[KCl]) (molar ratio)*	*Raw materials used (g)*			*Excessive Mg (wt%)*	*Heating profiles (℃ x h)*
		ZrO_2 (Coarse)	*CB (Fine)*	**Mg**		
ZC650	0.3	0.6161	0.0600	0.2430	0	650x8
ZC750	0.3	0.6161	0.0600	0.2430	0	750x8
ZC800	0.3	0.6161	0.0600	0.2430	0	800x8
ZC900	0.3	0.6161	0.0600	0.2430	0	900x8
ZC950	0.3	0.6161	0.0600	0.2430	0	950x8

Table 5.4: List of sample compositions and heating profiles for seeking the optimum excessive amounts of Mg at 950 °C for 8 and 6 h, respectively.

Sample ID	*[NaCl]/ ([NaCl]+[KCl]) (molar ratio)*	*Raw materials used (g)*			*Excessive Mg (wt%)*	*Heating profiles (℃ x h)*
		ZrO_2 (Coarse)	*CB (Fine)*	**Mg**		
ZC8hMg10	0.3	0.6161	0.0600	0.2673	10	950x8
ZC8hMg20	0.3	0.6161	0.0600	0.2916	20	950x8
ZC8hMg30	0.3	0.6161	0.0600	0.3159	30	950x8
ZC8hMg40	0.3	0.6161	0.0600	0.3402	40	950x8
ZC6hMg0	0.3	0.6161	0.0600	0.2430	0	950x6
ZC6hMg20	0.3	0.6161	0.0600	0.2916	20	950x6
ZC6hMg30	0.3	0.6161	0.0600	0.3159	30	950x6
ZC6hMg40	0.3	0.6161	0.0600	0.3402	40	950x6

Table 5.5: List of sample compositions and heating profiles for examining the effects of Mg and molten salt on the synthesis.

Sample ID	*[NaCl]/ ([NaCl]+[KCl]) (molar ratio)*	*Rawmaterials used (g)*			*Excessive Mg (wt.%)*	*Heating profiles (℃ x h)*
		ZrO_2 (Coarse)	*CB (Fine)*	**Mg**		
ZCnoMg	0.3	0.6161	0.0600	0.2430	0	950x8
ZCnosalt	0.3	0.6161	0.0600	0.3402	40	950x8

Table 5.6: List of sample compositions and heating profiles for investigating the effect of fine ZrO_2 particles on the ZrC formation.

Sample ID	*[NaCl]/ ([NaCl]+[KCl]) (molar ratio)*	*Raw materials used (g)*			*Excessive Mg (wt%)*	*Heating profiles (℃ x h)*
		ZrO_2 (Fine)	*CB (Fine)*	**Mg**		
ZC750F	0.3	0.6161	0.0600	0.2430	0	750x8
ZC800F	0.3	0.6161	0.0600	0.2430	0	800x8
ZC850F	0.3	0.6161	0.0600	0.2430	0	850x8

Table 5.7: List of sample compositions and heating profiles for seeking an optimum excessive amount of Mg at 850 °C.

Sample ID	*[NaCl]/ ([NaCl]+[KCl]) (molar ratio)*	*Raw materials used (g)*			*Excessive Mg (wt%)*	*Heating profiles (℃ x h)*
		ZrO_2 (Fine)	*CB (Fine)*	**Mg**		
ZC0MgF	0.3	0.6161	0.0600	0.2430	0	850x8
ZC10MgF	0.3	0.6161	0.0600	0.2673	10	850x8
ZC20MgF	0.3	0.6161	0.0600	0.2916	20	850x8

5.3 Results and Discussion

5.3.1 Thermodynamic calculations

Relevant reactions which might involve during the synthesis are listed as follows based on the references [87, 203]:

$$ZrO_2 + 2Mg = Zr + 2MgO \quad (5.2); \quad \Delta H_{298K} = -103.21\ kJ/mol$$

$$Zr + C = ZrC \quad (5.3); \quad \Delta H_{298K} = -196.38\ kJ/mol$$

$$ZrO_2 + C = Zr + CO_2 \quad (5.4); \quad \Delta H_{298K} = 706.51\ kJ/mol$$

$$ZrO_2 + 2C = ZrC + CO_2 \qquad (5.5); \quad \Delta H_{298K} = 510.13\ kJ/mol$$

$$2Mg + 3C = Mg_2C_3 \qquad (5.6); \quad \Delta H_{298K} = 80.97\ kJ/mol$$

$$C + 2MgO = 2Mg + CO_2 \qquad (5.7); \quad \Delta H_{298K} = 809.71\ kJ/mol$$

Gibbs free energy changes (ΔG) of the relevant reactions were calculated as a function of temperature and presented in Fig. 5.2.

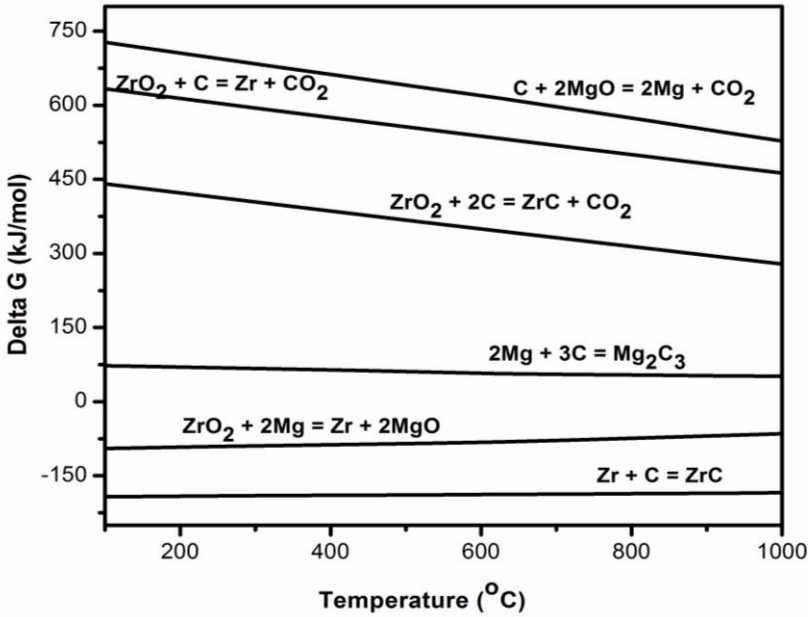

Figure 5.2 Gibbs free energy of a reaction possibly involved in the synthesis process as a function of temperature.

It can be found that, among those listed reactions, only reactions (5.2) and (5.3) are thermodynamically favorable at the test temperature range due to their negative values of ΔG. As a result, three possible subreactions can be predicted here. The first is that ZrO_2 could be reduced by Mg via reaction (5.2) rather than by carbon black (CB) via reaction (5.4). The second is that ZrC could be formed by the reaction of Zr with CB via reaction (5.3) rather than by the direct reaction

of ZrO_2 with CB (reaction (5.5)). However, in the method of carbothermal reduction, it was reported that reaction (5.4) becomes favourable at the temperature above 1500 °C [91, 204]. The final prediction is that the presence of an intermediate reaction (5.6) is unlikely at the test temperature range because of the positive value of ΔG.

5.3.2 Differential thermal analysis

As shown in Fig. 5.3, DTA curves exhibited sharp endothermic peaks (indicated by numbers (1), (2), (3), and (4)) at ~650, ~660, ~770, and ~800 °C, respectively. These endothermic peaks are attributed to the transitions from solid phases to liquid phases, i.e., melting of the solid phases originally present in the samples. Endothermic peak (1) was observed in all samples, although it was almost invisible in sample (3) due to its overlapping with peak (2). It corresponded to the melting point (~650 °C) of metallic Mg. The sharp endothermic peaks (2), (3), and (4) at ~660, ~770, and ~800 °C, respectively, in samples containing NaCl-KCl, KCl, and NaCl corresponded to the melting points of the three salts. Thermal changes and melting orders of those solid phases contained in the samples, therefore, can be described as follows.

On heating, the first liquid phase formed in the reaction system was Mg. It started melting at ~640 °C and finished at ~660 °C. The overlapping of peaks (1) and (3) in the case of sample (c) suggested that the mixed NaCl-KCl salt started melting while Mg was melting, and finished at ~700 °C. Whereas, the melting temperature ranges of KCl and NaCl were 750-785 °C and 780-820 °C, respectively. As a result, the minimum processing temperature for the ZrC synthesis should be at least equal to the melting temperature of the binary NaCl-KCl salt.

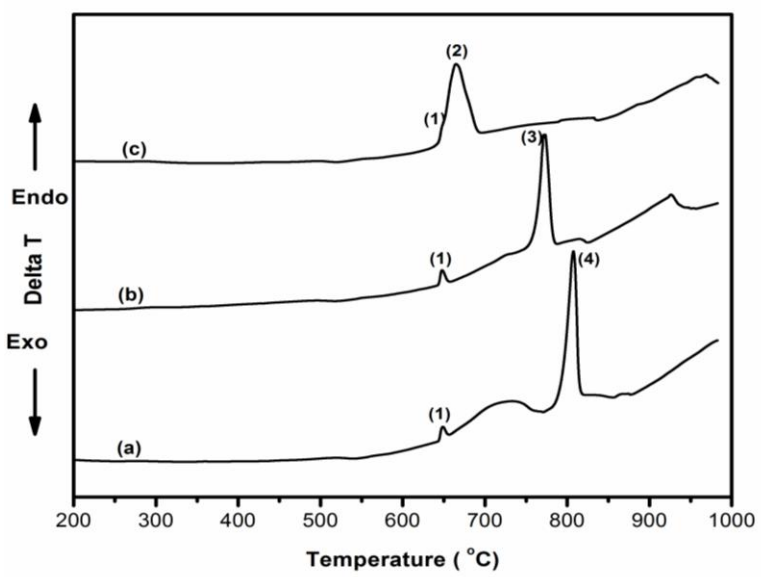

Figure 5.3 DTA curves of the stoichiometric mixtures containing (a) NaCl, (b) KCl, and (c) NaCl-KCl.

5.3.3 Effects of processing parameters on the ZrC formation

5.3.3.1 Salt Selection

Figure 5.4 shows XRD of samples containing various molar ratios of [NaCl]/[NaCl+KCl] = (a) 0, (b) 0.1, (c) 0.3, (d) 0.5, (e) 0.7 and (f) 1. Figure 5.5 illustrates the formation extents of ZrC indicated by the calculated value of $I_{max, ZrC}/I_{max,ZrO2}$, at each molar ratio ($I_{max, ZrC}$ and $I_{max,ZrO2}$ values were the maximum intensities of ZrC and ZrO_2 peaks located at 2θ around 33.40° and 28.40°, respectively). The larger the value of $I_{max, ZrC}/I_{max,ZrO2}$ is, the higher the productivity of ZrC and hence the less the residual ZrO_2 remained in the sample. Fig. 5.5 also displays the melting temperature of each mixed composition, according to the phase diagram determined by Coleman and Lacy [205].

As shown in Fig. 5.4, ZrC and $Mg(OH)_2$ were evident as major phases in all salt systems at the test temperature. ZrC was formed as a product phase of the reaction during heat treatment process, whereas $Mg(OH)_2$ was produced in the process of salt removal via reaction (5.8).

$$Mg(s) + 2H_2O(g) = Mg(OH)_2(s) + H_2(g) \quad (5.8)$$

An evidence supporting this is that the observation of bubbles (gas phase) when hot distilled water was poured into the reacted sample. This is attributed to hydration process of the residual Mg in the resultant powder during the washing procedure [206]. As compared with the results gained from Chapter 4 (Fig. 4.3), $Mg(OH)_2$ was absent when $MgCl_2$ was used as a reaction medium, whereas its formation was obvious when KCl salt was applied. This is because the better dissolution of Mg in the molten $MgCl_2$ than in the molten KCl which leads to the absence of $Mg(OH)_2$, when $MgCl_2$ was used, due to the nonexistence of residual Mg in the resultant powder fired in $MgCl_2$ salt.

Here, although ZrC phase was evident in all salt systems at the test temperature, its content (Fig. 5.5) was different depending on the salt compositions. It is clear that additions of NaCl to KCl salt did provide some effects on the ZrC formation and ZrO_2 reduction. Sample (a) (without NaCl) exhibited $I_{max,\,ZrC}/I_{max,ZrO2} = 1.62$. However, when NaCl was increasingly added to KCl based-salt to 0.3 molar fraction, the value of $I_{max,\,ZrC}/I_{max,ZrO2}$ increased considerably to the maximum of 2.27. On further increasing NaCl concentrations, however, the $I_{max,\,ZrC}/I_{max,ZrO2}$ changed adversely to the lowest value of 1.40 at the molar fraction of 0.7. These results were attributed to the effect of melting points of the binary salts. According to a previous study [205], a binary NaCl-KCl salt with a mixing molar ratio between 0.3 and 0.6 melts eutectically at the lowest temperature of ~645°C.

Even so, however, only in the case of the molar fraction = 0.3, the highest value of $I_{max,\ ZrC}/I_{max,ZrO2}$ was achieved. This implied that too much NaCl in the salt mixture would result in less formation of ZrC phase even at a eutectic region. Furthermore, in comparison with single salt NaCl and KCl, the binary salt with the molor ratio of [NaCl]/[NaCl+KCl] = 0.3 still resulted in the highest productivity of ZrC. Thus, the binary salt NaCl-KCl with the mixing molar fraction of 0.3 was chosen as a reaction medium for further optimisation of the synthesis condition.

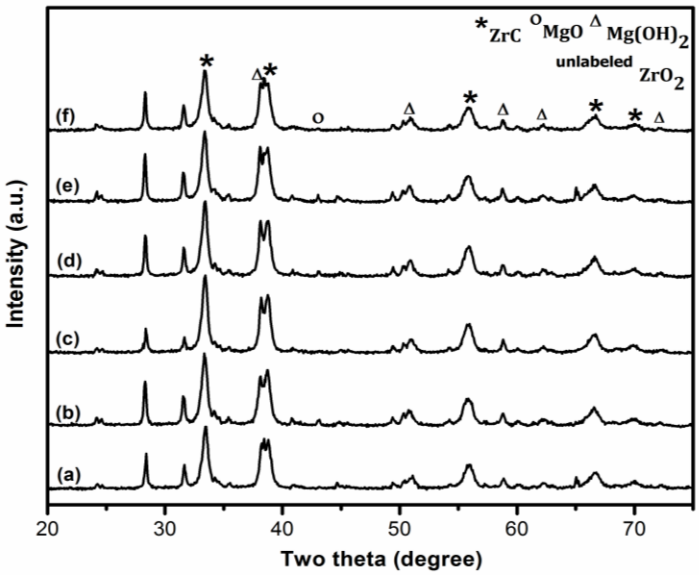

Figure 5.4 XRD patterns of samples containing different molar fractions of [NaCl]/[NaCl+KCl] = (a) 0, (b) 0.1, (c) 0.3, (d) 0.5, (e) 0.7, and (f) 1 which were heated at 900 °C for 8h in Ar.

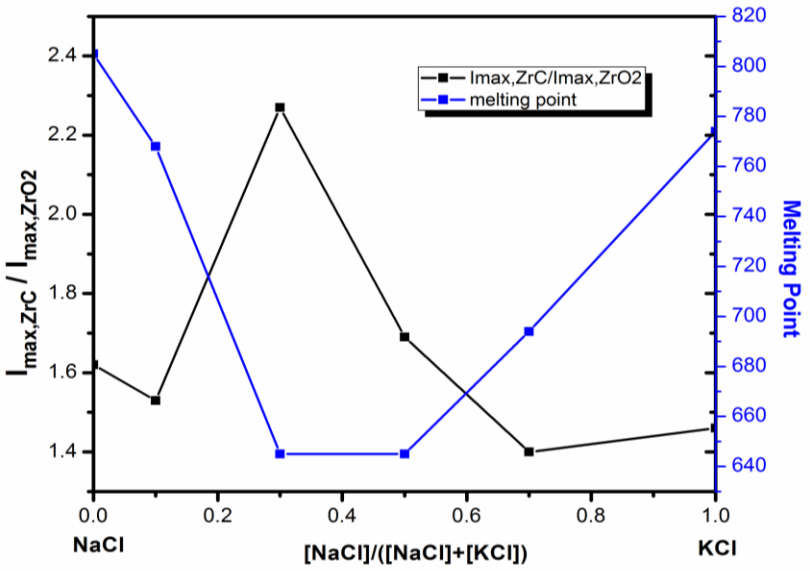

Figure 5.5 (Left) Imax, ZrC/Imax,ZrO_2 value of each sample ((a)-(f)) obtained from XRD results in Fig. 5.4 and (Right) melting temperatures of NaCl-KCl binary salts according to the phase diagram given by Coleman and Lacy [205].

5.3.1.2 Effect of processing temperature on the ZrC formation

Figure 5.6 gives XRD of unleached samples after heating for 8 h at 650 to 950 °C in argon. As shown in Fig. 5.6, five crystalline phases including monoclinic ZrO_2, cubic ZrC, Zr, MgO, and $Mg(OH)_2$ were detected in the fired samples. ZrO_2 always remained even after firing at the temperature as high as 950 °C indicating its high stability. At 650 °C, ZrO_2 remained as a major phase whereas the product ZrC was a minor. At this temperature, Zr was formed along with MgO suggesting reduction process of ZrO_2 via Reaction (5.2). On further increasing temperature to 750 °C, ZrC became predominant whereas ZrO_2 became a minor phase along with the significant reduced Zr. The observation revealed that the conversion of ZrO_2 to ZrC had been enhanced considerably with an increase in the synthesis temperature. Furthermore, that ZrC already became a major phase at as low as 750 °C illustrated an obvious advantage of this processing technique.

As a comparison, in the case of using conventional synthesis techniques, ZrC appeared as a major phase only when the processing temperature was above 1450 °C [7, 67, 97, 204].

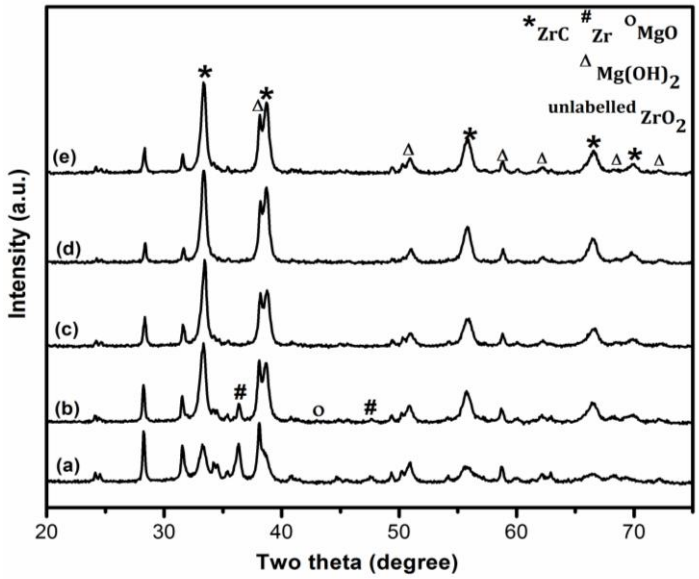

Figure 5.6 XRD patterns of samples heated for 8 h at (a) 650, (b) 750, (c) 800, (d) 900 and (e) 950 °C, respectively, in Ar.

Five obvious peaks of ZrC phase were observed at 2θ around 33.18°, 38.50°, 55.59°, 66.30° and 69.66° which correspond to the diffraction planes of (111), (200), (220), (311) and (222), respectively. ZrC peaks increased considerably with temperature, while ZrO_2 peaks decreased, indicating the enhanced conversion of ZrO_2 to ZrC with temperature. Upon heating to 950 °C, no further obvious improvement in the peaks intensity of ZrC whereas that of ZrO_2 became slightly increased as compared to the results gained from heating at 900 °C. These results were due to the presence of insufficient reductant (Mg) which partially evaporated at the test temperatures. Considering this, excessive Mg was added

to compensate its loss at high temperatures. The results are presented in the next section.

5.3.1.3 Effect of excessive Mg addition on the ZrC formation

Figure 5.7 presents XRD of non-stoichiometrically mixing samples, containing excessive Mg contents of 10-40 wt.%, after firing for 8 h at 950 °C. As shown in Fig. 5.7, with increasing the excessive Mg contents from 10 to 40 wt.%, ZrO_2 peaks decreased evidently and disappeared when the excessive Mg was 40 wt.%, indicating the complete conversion of ZrO_2 to ZrC at this optimised synthesis condition. The significant improvement in the reduction of ZrO_2 peaks intensity, when Mg contents were excessively added, confirmed that Mg was partially evaporated during the synthesis because of its higher evaporation pressure at elevated temperatures [191].

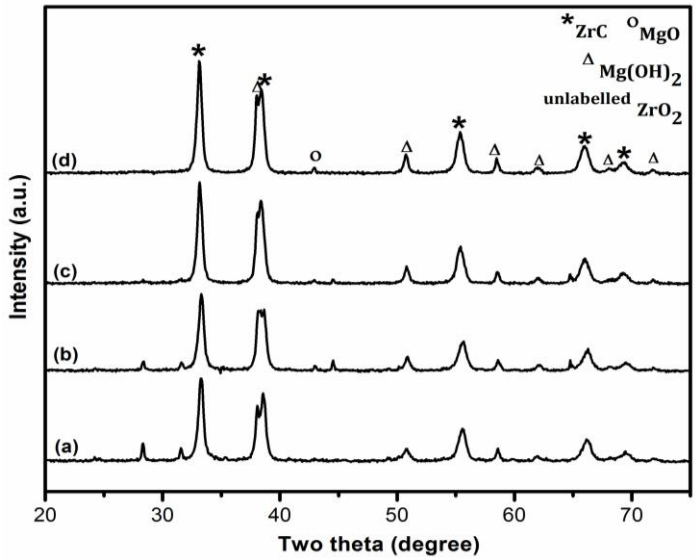

Figure 5.7 XRD patterns of unleached samples containing excessive Mg contents of (a) 10, (b) 20, (c) 30, and (d) 40 wt.%, according to the stoichiometric requirement of reaction (5.1), heated in NaCl-KCl for 8 h at 950 °C in Ar.

5.3.1.4 Effect of the holding time on the ZrC formation

Figure 5.8 shows XRD of samples containing excessive Mg contents of 10-40 wt.% after firing for 6 h at 950 °C. As shown in Fig. 5.8, the ZrO_2 peaks intensity in the samples decreased dramatically with increasing the excessive Mg additions from 0 to 30 wt.% and the lowest peaks intensity of ZrO_2 was observed in the sample containing 30 wt.% excessive Mg. Nevertheless, tiny ZrO_2 peaks were still remained indicating an incomplete reaction at the synthesis condition. On further increasing the excessive Mg to 40 wt.%, ZrO_2 peaks increased adversely (Fig. 5.8d). These observations suggested that it is unworthy to add more Mg into the system than that actually required for the compensation. The findings in this section revealed that (i) with 6 h-holding time, the reaction was incomplete even though with the corrected compensation of the reducing agent, and (ii) the amount of Mg loss due to its evaporation increased from 30 wt.% to 40 wt.% with the increased holding time from 6 h to 8 h.

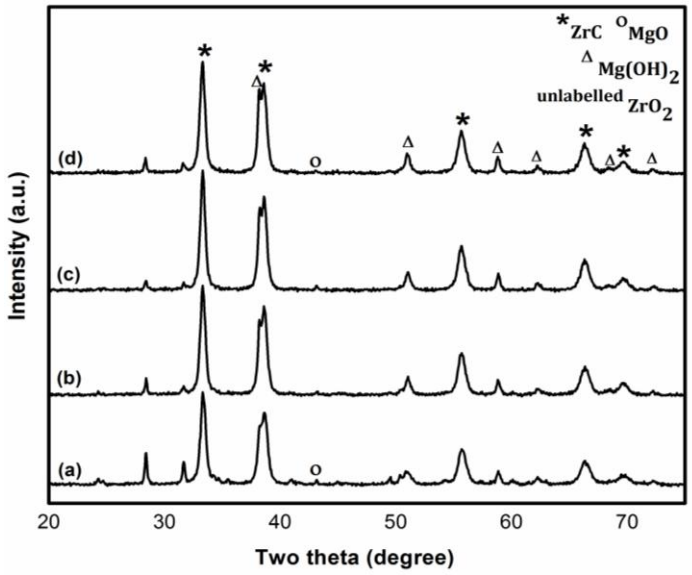

Figure 5.8 XRD patterns of unleached samples containing excessive Mg contents of (a) 0, (b) 20, (c) 30, and (d) 40 wt.%, according to the stoichiometric requirement of Reaction (5.1) which were heated in NaCl-KCl at 950 °C for 6 h.

5.3.1.5 Effect of use of fine ZrO_2 particles on the ZrC formation

Figure 5.9 shows XRD of samples prepared from fine ZrO_2 and CB particles which were heated for 8 h at 750-850 °C. As shown in Fig. 5.9, ZrC was already a major phase at as low as 750 °C, whereas ZrO_2 and Zr remained as minor phases. On further increasing temperature, there was a significant reduction in the ZrO_2 peaks intensity and significant increase in ZrC peaks intensity. Furthermore, the intermediate phase Zr disappeared. These results indicated the enhanced reduction rate of ZrO_2 with temperature and the high reactivity of the produced Zr with CB forming the final product ZrC. Nevertheless, a considerable amount of ZrO_2 still remained even at 850 °C. This could be similarly attributed to the evaporation loss of Mg during the synthesis, as discussed above.

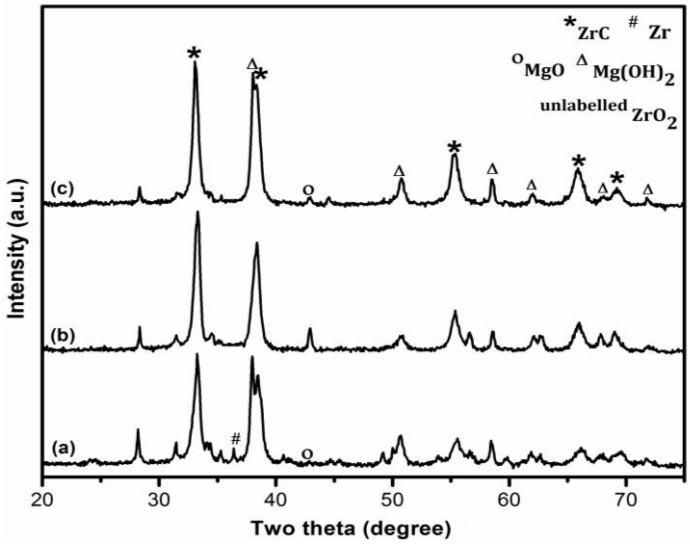

Figure 5.9 XRD patterns of unleached samples prepared from stoichiometrically mixing requirement of Reaction (5.1) which were heated in NaCl-KCl for 8 h at (a) 750, (b) 800, and (c) 850 °C in Ar.

Figure 5. 10 shows XRD of samples containing excessive Mg contents of 10-20 wt.% which were fabricated from fine ZrO_2 particles and heated at 850 °C for 8 h.

Similarly to those presented in Fig. 5.7, ZrO_2 peaks decreased evidently with the excessive amounts of Mg addition. They became invisible when 20 wt.% excessive Mg was added, indicating the complete conversion of ZrO_2 to ZrC product. It is clear that the evaporation loss of Mg was influenced greatly by the synthesis temperature. When coarser ZrO_2 particles were used, the reaction was completed at 950 °C and 40 wt.% excessive Mg had to be used (Fig. 5.7). However, when finer ZrO_2 used, the reaction could be completed at 850 °C and only 20 wt.% excessive Mg had to be used. This further implied that use of finer ZrO_2 particles could result in a lowered synthesis temperature and thus reduced evaporation loss of Mg.

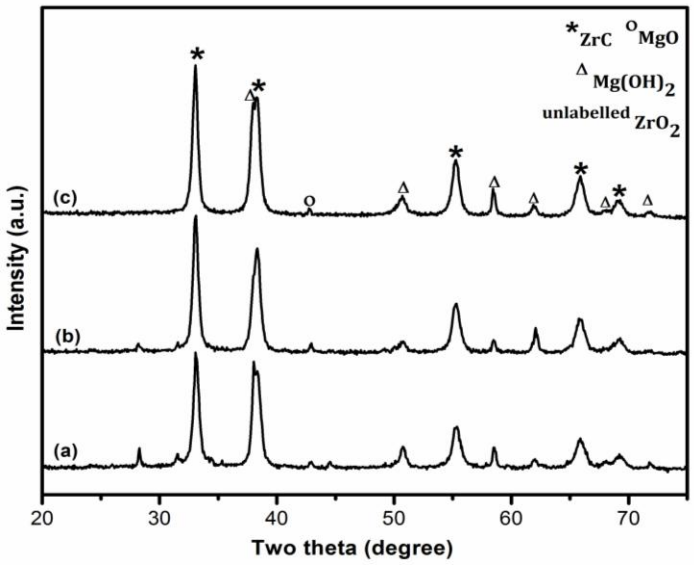

Figure 5.10 XRD patterns of unleached samples containing (a) 0, (b) 10 and (c) 20 wt.% excessive Mg, according to the stoichiometric requirement of Reaction (5.1), which were heated in NaCl-KCl for 8 h at 850 °C in Ar.

The reduced synthesis temperature from 950 to 850 °C, with replacing micronsized ZrO_2 powders by nanosized ones, indicated a great influence of the particle size on the synthesis reaction. Fine ZrO_2 particles possess higher specific

area resulting in increased contacts between the reactant species and their diffusion in the molten salt, thus, accelerating the conversion from ZrO_2 to ZrC.

Figure 5.11 illustrates XRD of the leached product powders produced from (a) coarse and (b) fine ZrO_2 particles at 950 and 850 °C, respectively, revealing high purity level of the final product. Furthermore, comparison between the ZrC peaks from both samples reveals that ZrC powders prepared at 950 °C (Fig. 5.11b) exhibited a higher peaks intensity along with the narrower peaks width, suggesting their higher crystallinity and larger crystallite size [13].

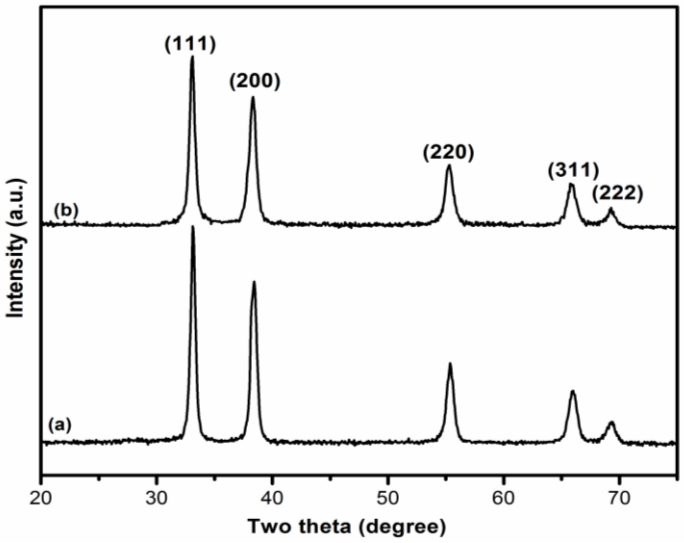

Figure 5.11 XRD patterns of leached ZrC powders synthesised from: (a) coarse and (b) fine ZrO_2 powders at 950 °C and 850 °C, respectively.

5.3.1.6 Comparison of the conventional reduction method and the MSS technique

Shown in Fig. 5.12 is XRD patterns of phases in samples after 8 h firing at 950 °C via the conventional reduction route and the MSS technique (with/without Mg). As shown in Fig. 5.12a, when Mg was absent, no ZrC phase was formed in the

ZrO_2-CB sample after 8 h firing in the molten salt at 950 °C. On the other hand, when a molten salt was absent, small amounts of ZrC were formed (Fig. 5.12b) in the sample of ZrO_2-Mg-CB. These results suggested that Mg acted as the only reducing agent generating Zr (Reaction (5.2)) which further reacted with CB forming ZrC (Reaction (5.3)). The extent of ZrC formation when no salt was used, however, was very low, as implied by the still high peaks of unreacted ZrO_2. However, when the reaction system (ZrO_2-Mg-CB) was performed in the molten salt at the identical temperature, the reaction was effectively completed (Fig. 5.12c). This revealed clearly a main advantage the MSS technique over the conventional reduction techniques.

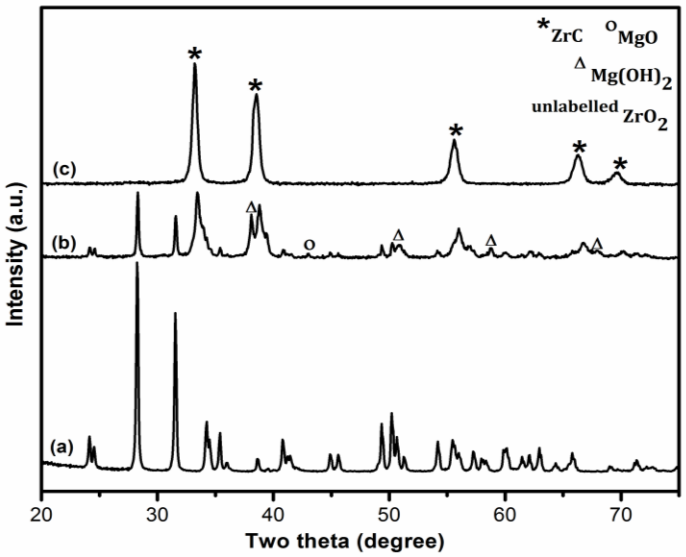

Figure 5.12 XRD patterns of samples prepared from coarse ZrO_2 with 40 wt.% excessive Mg after 8 h firing at 950 °C via (a) conventional thermal reduction (ZrO_2-CB, without Mg and salt), (b) conventional magnesiothermic reduction (ZrO_2-CB-Mg, without salt) and (c) molten salt mediated magnesiothermic reduction (ZrO_2-CB-Mg).

5.3.2 Microstructural observation

Figure 5.13 demonstrates microstructures of ZrC particles produced at 950 °C for 8 h in Ar from coarse ZrO_2 particles, along with those of the raw materials CB and ZrO_2 powders. CB particles showed approximately rounded shapes with an averaged size around 30 nm (Fig. 5.13a). ZrO_2 particles exhibited angular shapes with an averaged size around 300-400 nm (Fig. 5.13b). The as-prepared ZrC particles displayed the morphologies of both ZrO_2 and CB particels (Fig. 5.13c). Figure 5.14 illustrates microstructures of the as-prepared ZrC powder which was fabricated from fine ZrO_2 particles and heated at 850 °C for 8 h in the environment of argon, along with those of the raw materials used for the synthesis. The product powder exhibited a uniform distribution suggesting an attractive merit of the MSS route used. Both raw materials exhibited rounded shapes with an averaged diameter around 30 and 40 nm for CB and ZrO_2, respectively (Fig. 5.14a-b). The as-prepared ZrC powder also displayed rounded shapes with the particle sizes of 30-40 nm.

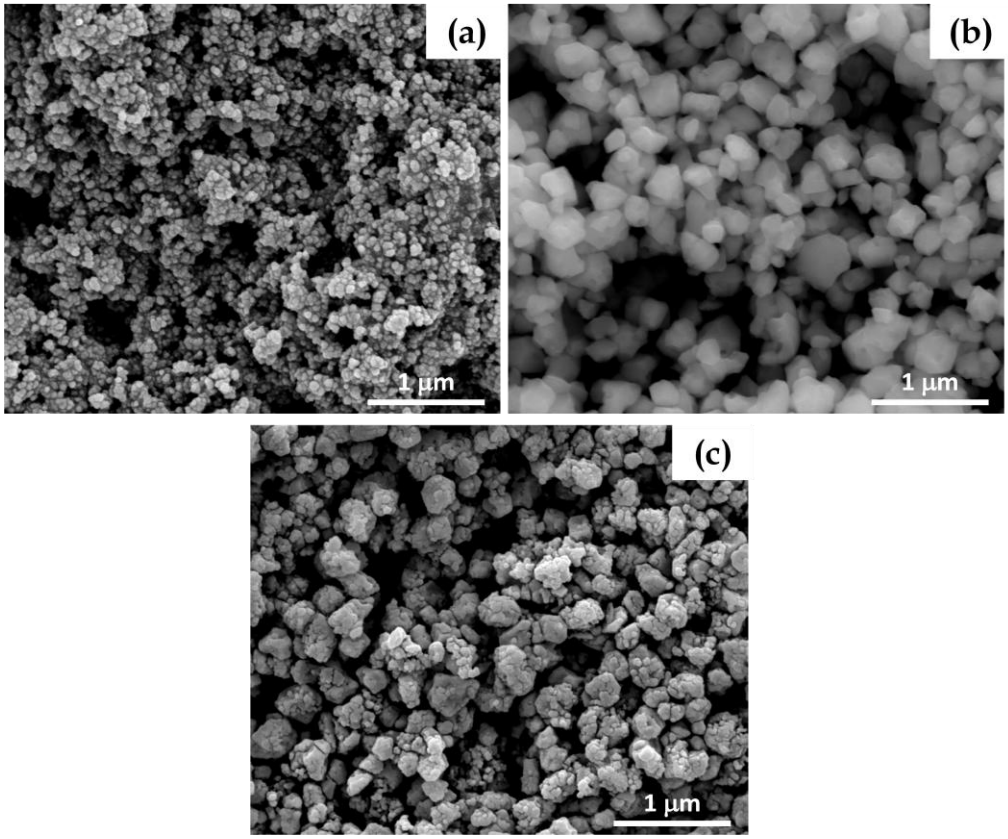

Figure 5.13 SEM images of the starting raw materials: (a) nanosized CB particles and (b) submicron ZrO_2 powder and (c) the as-prepared ZrC powder which was heated at 950 °C for 8 h in Ar.

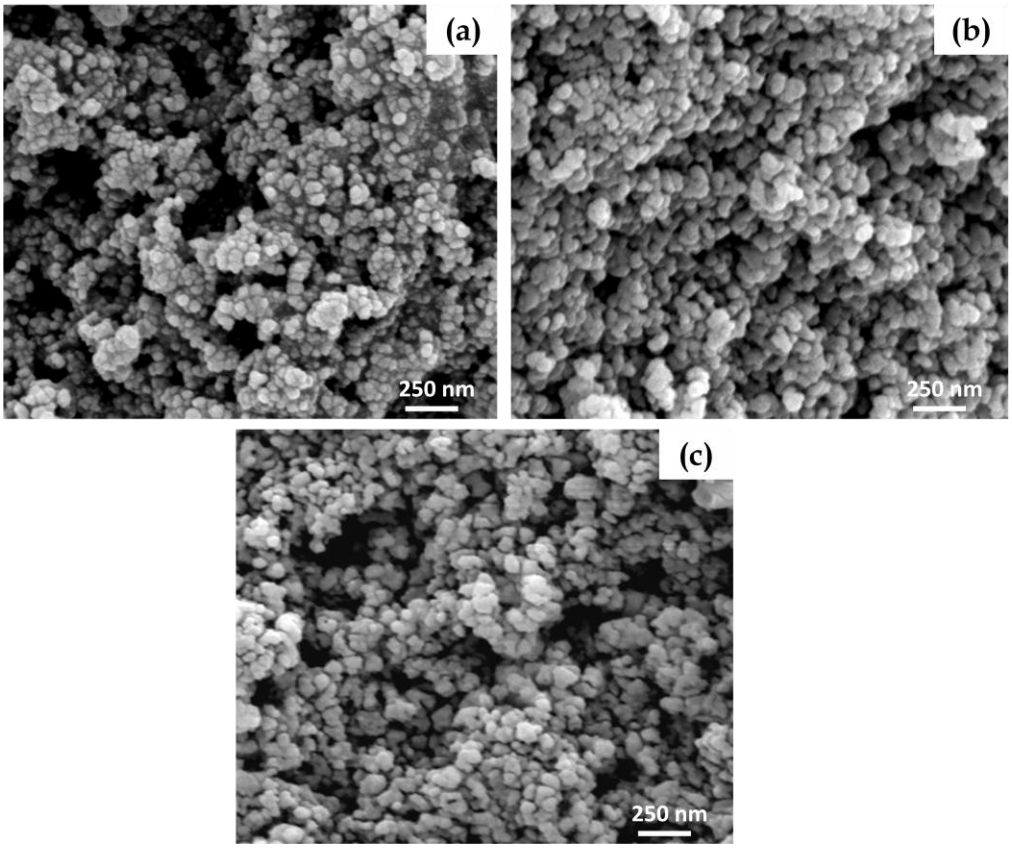

Figure 5.14 SEM images of the starting materials; (a) nanosized CB particles and (b) nanosized ZrO_2 powder and the as-prepared ZrC powder which was heated at 850 °C for 8 h in Ar.

The results suggested that the as-prepared ZrC powder composed of two different morphologies: one displayed similar shapes and sizes to those of the original ZrO_2 particles and the other showed the rounded shapes with an averaged particle size around 30 nm of the original CB particles. The former seemed to retain the shapes and the sizes of the starting ZrO_2 particles, whereas the latter preserved those of the CB particles. The well preservation in shapes and sizes of the original ZrO_2 and CB particles observed from the synthesised ZrC powder suggested that template growth mechanism [156, 157] governed the

product formation in which both ZrO_2 and CB could have acted as the templates, which will be discussed in more detail below.

5.4 Synthesis mechanism and advantages of molten salt mediated magnesiothermic reduction process

As mentioned above, reaction (5.2) and (5.3) had possibly involved in the synthesis process. On heating, ZrO_2 was reduced initially by Mg generating Zr and MgO (reaction (5.2)). Zr, which is more soluble than CB, would dissolve in the salt melt. The dissolved Zr would diffuse through the molten salt medium to the surfaces of CB particles and subsequently react to form ZrC particles via reaction (5.3) which retained the shapes and sizes of the original CB particles. This explanation is in well accordance with the formation of the rounded ZrC particles with an averaged diameter around 30 nm. Considering that CB almost does not dissolve in the molten salt used, it seemed difficult to use the "template-growth" mechanism to explain the formation of those ZrC particles having angular shapes with an averaged size around 400 nm. One possible explanation could be as follows. The much bigger size of Zr particles might have reduced their dissolution in the molten salt. CB powders, on the other hand, were much smaller sized and lightweight, so some of them might have been brought to the surfaces of Zr particles by the local movement of the salt and then reacted with the remaining Zr particles to form the ZrC particles which preserved the shapes and sizes of the Zr particles.

In comparison with other conventional synthesis methods, much lowered synthesis temperature could be achieved in the present work to fabricate pure ZrC powder, which could be attributed to the use of the molten salt which resulted in more homogeneous mixing and rapid diffusion of the relevant

species in them, thus accelerating the synthesis reaction. By using this cheap and simple but novel method, the formation of ZrC phase became evident at as low as 650 °C (Fig. 5.6) and phase pure ZrC powder was obtained at 950 or 850 °C when coarse or fine ZrO_2, respectively, were applied. Furthermore, the as-prepared ZrC fine particles were homogeneously dispersed, suffering from only limited agglomeration. To compare, Chu et al. [204] synthesised ZrC powder via a carbothermal reduction process at 1600 °C. This process, apart from high temperature involved, the final product powder contained high levels of impurity phases such as zirconium oxycarbides. Sevastyanov et al. [100] synthesised nanosized ZrC powder using a complex and expensive hybrid method which combines sol–gel processing and carbothermal reduction together. They found that ZrC phase began to form at 1050°C and the reaction completed at a temperature as high as 1400 °C. Doll et al. [99] fabricated nanosized ZrC powder (~90 nm) via sol-gel processing at temperatures between 1400 and 1600 °C. The technique used was complicated and expensive raw materials and high processing temperatures were required. Songet al. [207] used an SHS method to fabricate ZrC powder. Expensive elemental powders of Zr, Al and C were used. Although fine ZrC powder (50 nm) was prepared, 50 wt.% of expensive Al powder was excessively added and undesirable $ZrAl_3$ phase remained in the product powder. Nanocrystalline ZrC particles (~30 nm) were also prepared by Wang et al. [208] via solid state reaction of ZrO_2-Li_2CO_3-Mg, however, they were heavily agglomerated.

5.5 Conclusions

Phase pure submicron-sized and nanosized ZrC powders were synthesised using carbon black, ZrO_2 and Mg powders as raw materials and NaCl-KCl as a reaction medium. The synthesis temperatures were lowered to as low as 950 and 850 °C

when submicron-sized and nanosized ZrO_2 particles were used, respectively. These temperatures were much lower than those used by most of the reported conventional techniques. The synthesised ZrC powder exhibited shapes and sizes similar to those of starting CB and ZrO_2 particles, indicating that both CB and ZrO_2 could have acted as reaction templates during the ZrC formation.

Processing parameters including temperature, time, excesive Mg addition and particle sizes of starting ZrO_2 significantly influenced the ZrC formation. ZrC peaks increased, whereas ZrO_2 peaks reduced, with the synthesis temperature. At 950 $^{\circ}$C, the reaction was incomplete when 6 h of reaction time was performed but it was complete with 8 h of the holding time. The evaporation loss of Mg was strongly dependent on the firing temperature and holding time. The higher temperature (and/or holding time), the larger the amount of Mg evaporation loss. Therefore, 40 wt.% excessive Mg was required to make the reaction complete at 950 °C for 8 h, whereas only 20 wt.% Mg required at 850 °C for 8 h. Particle size of the starting ZrO_2 also plays an important role in determining the synthesis temperature. Using nanosized ZrO_2 particles to replace the micronsized ones could effectively lower the synthesis temperature from 950 to 850 °C.

Chapter Six

Low Temperature Molten Salt Synthesis of TiC nanosheets (TNS) and TiC-Coated Graphite Nanosheets (TCNS)

6.1 Introduction

Because of their outstanding properties and potential applications, ultrathin two-dimensional (2D) nanosheets have attracted a great deal of attention recently from researchers worldwide. The 2D-nanosheets can not only have enhanced intrinsic properties compared to their bulk counterparts, but also exhibit new properties. A good example is "graphene" which is the most well-known layer-structured material with atomic thickness and shows many excellent properties. The extensive studies on graphene have sparked new discoveries towards graphene-analogous materials. By using the similar fabrication techniques to those used in the case of graphene, a number of inorganic intrinsic 2D-

nanostructured materials, including BN, WS_2, MoS_2 and $NbSe_2$ [38, 41, 209, 210] have been prepared and characterised [15-17, 40, 41, 209, 211-217]. Quite recently, the quasi-ternary carbides such as Ti_3C_2 and Ti_2C and nitrides have been exfoliated to form the so-called 2D-nanostructured "MXene" (as reviewed in Chapter 2) [45, 51]. Nevertheless, the work on 2D-nanostructured carbide materials is still very limited, in particular, compared with that on intrinsic 2D-nanostructured materials mentioned above.

In the present work, a straightforward and cost effective method for producing novel TiC nanosheets (TNS) and TiC-coated graphite nanosheets (TCNS) with large specific surface areas has been developed. Graphite nanosheets (GNS) were used as 2D-nanostructured templates reacting with metallic titanium powder in the molten KCl at a given temperature range to obtain TNS (Fig. 6.1) and TCNS (Fig 6.2). The effects of processing parameters (e.g. processing temperature and time), and the relevant reaction mechanisms were discussed.

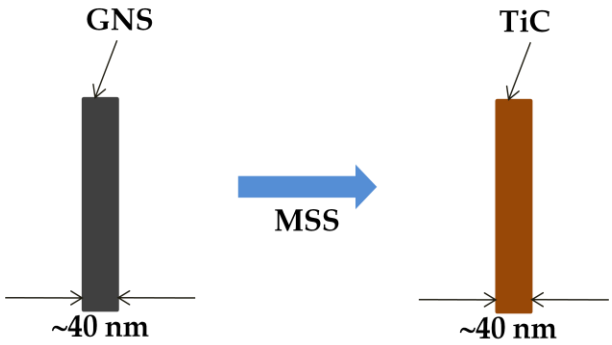

Figure 6.1 Schematic diagram illustrating the strategy used for producing TNS. The diagram was drawn based on side-view projections of the GNS and the final product (TNS).

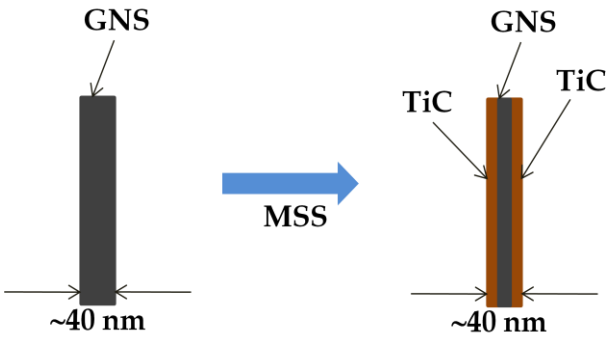

Figure 6.2 Schematic diagram illustrating the strategy used for fabricating TCNS. The diagram was drawn based on side-view projection of the GNS and the final product (TCNS).

6.2 Experimental

6.2.1 Raw materials

Graphite nanosheets (GNS, 97% purity, thickness: ~40 nm, typical sheet size: ~10 μm, BET surface area: 100 m^2/g), metallic titanium powder (Ti, 99.6% purity) and potassium chloride (KCl, 99% purity) were used as starting raw materials. The GNS was received from Cheap Tubes Inc., USA and the others were supplied by Sigma aldrich, UK.

6.2.2 Sample preparation

The as-received GNS were dispersed in isopropyl alcohol (IPA) for 30 minutes using mild ultrasonication. The dispersion was then oven-dried overnight at 70 °C. Titanium powder and the dispersed GNS in an equimolar mixing ratio indicated by reaction (6.1), or in non-stoichimetric ratios (1/2 and 1/4) were mixed homogeneously in an agate motar to prepare TNS or TCNS samples, respectively. The mixture was further combined with KCl in the weight ratio of 1/30.

$$Ti + C = TiC \qquad (6.1)$$

The mixture was then contained in an alumina crucible covered with a lid and placed in an alumina tube furnace under a constant flow of argon. Based on the previous studies [160, 218, 219], using MSS technique, single TiC phase was achieved at the temperature between 950 and 1050 °C depending on the morphologies and properties of carbon sources. Here, the test temperature range was designed from 850 to 950 °C with a heating rate of 3°C/min and held for 4-8 h before being cooled down at the same rate to room temperature. The reacted mass was washed repeatedly with hot distilled water to remove the residual salt. The final product powder was oven-dried overnight at 100 °C prior to further characterisation. Sample compositions and heating profiles for synthesising TNS and TCNS were presented in Table 6.1.

Phase compositions in as-prepared product powder were identified by powder X-ray diffraction (XRD) analysis (Siemens D500 reflection diffractometer). Spectra were recorded at 30 mA and 40 kV using Ni-filtered Cu Kα radiation. The scan rate was 2°/min with a step size of 0.05°. ICDD cards used for the identification are TiC (32-1383), Ti (65-9622) and C (65-6212). Raman spectroscopy (Renishaw In Via micro-Raman spectrometer) was employed to identify chemical bonds presenting in the observed samples at the vibration Raman peaks. Green laser with the excitation wavelength of 514.5 nm and power of ~20 mV was focused on a ~2 μm spot to obtain Raman spectra. The microstructure of the fabricated nanosheets was investigated using a field emission gun scanning electron microscope (FESEM Inspect F) and a high resolution TEM (HRTEM, JEOL 2010F microscope), along with energy-dispersive spectroscope (EDS) and selected area electron diffraction (SAED).

Table 6.1: Sample compositions and heating profiles for fabricating TNS and TCNS.

Product Type	*Sample ID*	*Ti : C (molar ratio)*	*Raw materials used (g)*		*Heating profiles (℃ x h)*
			Ti	*C*	
TiC nanosheets (TNS)	T850	1:1	0.240	0.060	850 x 8
	T900	1:1	0.240	0.060	900 x 8
	T950	1:1	0.240	0.060	950 x 8
	T4h	1:1	0.240	0.060	950 x 4
	T6h	1:1	0.240	0.060	950 x 6
	T8h	1:1	0.240	0.060	950 x 8
TiC-coated graphite nanosheets (TCNS)	TC850A	1:2	0.240	0.120	850 x 5
	TC900A	1:2	0.240	0.120	900 x 5
	TC950A	1:2	0.240	0.120	950 x 5
	TC850B	1:4	0.240	0.240	850 x 5
	TC900B	1:4	0.240	0.240	900 x 5
	TC950B	1:4	0.240	0.240	950 x 5

6.3 Results and Discussion

6.3.1 Fabrication and characterisation of TiC nanosheets (TNS)

6.3.1.1 Effects of processing temperature on the TNS synthesis

Figure 6.3 displays XRD of samples heated for 8 h at (a) 850, (b) 900 and (c) 950 °C. Five sharp TiC peaks were observed in all samples at 2θ around 36.1, 42.0, 60.7, 72.6 and 76.4° which corresponded respectively to diffraction from the (111), (200), (220), (311) and (222) planes of face-centred cubic TiC. With increasing the temperature, TiC peaks increased significantly, while Ti and carbon peaks

decreased. The detection of unreacted Ti and carbon at 850 and 900 °C suggested incomplete reaction at the test temperatures. On further increasing temperature to 950 °C, all Ti and carbon were consumed and single TiC phase was obtained (Fig. 6.3c).

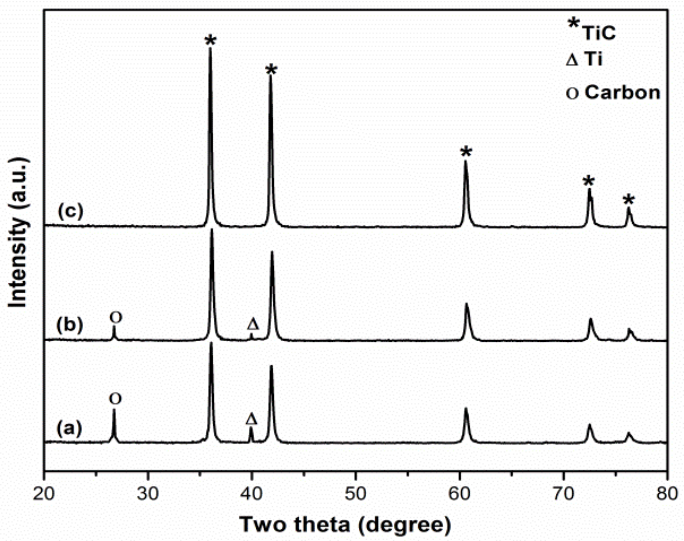

Figure 6.3 XRD patterns of samples heated for 8 h at (a) 850, (b) 900 and (c) 950 °C in Ar.

6.3.1.2 Effects of holding time on the TNS synthesis

Figure 6.4 demonstrates XRD of samples heated at 950 °C for different periods of time. TiC peaks increased evidently, while the residual Ti and carbon peaks decreased apparently, with increasing the holding time from 4 to 8 h (Fig. 6.4a-c). Both Ti and carbon peaks became invisible when the holding time was 8 h, suggesting the minimum holding time required for completing the reaction.

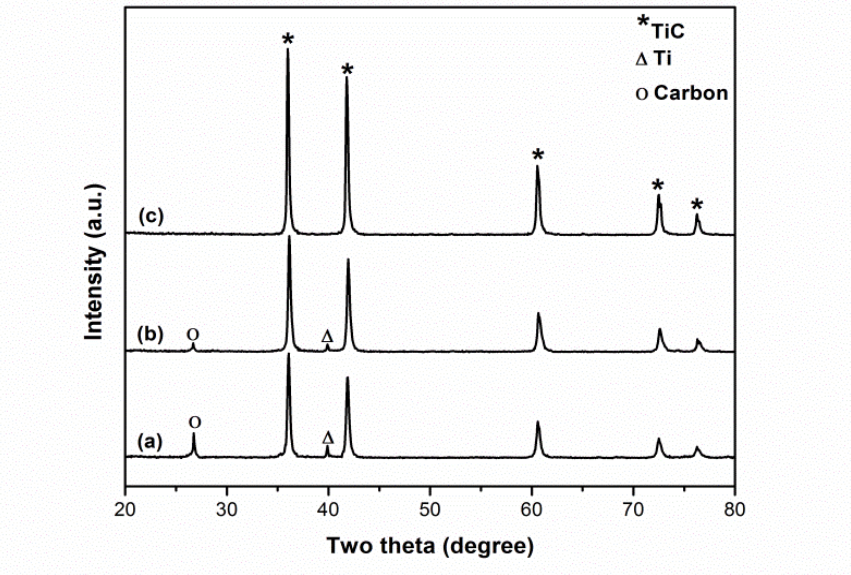

Figure 6.4 XRD curves of samples heated at 950 °C for (a) 4 h, (b) 6 h and (c) 8 h in Ar.

Although TNS could be synthesised successfully at such a relatively low temperature, the holding time used (8 h) seemed to be longer than that used previously in the MSS of other TiC materials. This is due to the difference in the carbon source used. For example, only 5 h was required to synthesise TiC nanofibres at 950 °C when carbon nanofibres were used as a carbon source [160]. Compared with GNS used in the present work, carbon nanofibres are much smaller and more reactive, so a shorter reaction time was required for completing the reaction.

6.3.1.3 Microstructural observations of the synthesised TNS

Figure 6.5 compares microstructures and EDS spectra of as-received GNS and as-prepared TNS. The original GNS were ultrathin (~40 nm) and wrinkled sheets with an average size around 10 μm. The as-prepared product displayed similar morphologies to the original GNS, in terms of an ultrathin sheet with its

thickness around 40 nm, although the lateral size was smaller (~5 μm). The reduction in size of the as-prepared nanosheets is attributed to the effect of mild sonication, performed in the process of sample dispersion prior to SEM and TEM examinations, along with the brittle nature of hard carbide materials resulting in cracking and splitting the product nanosheets into smaller pieces. Therefore, it can be considered that the as-prepared TNS exhibited similar shapes and sizes to those of the original GNS, indicating a template growth mechanism dominating the product formation.

Furthermore, compared with smooth surfaces of the as-received GNS (Fig. 6.5b), rougher surfaces (Fig. 6.5e) were observed on the TNS, suggesting the formation of some fine phases on the latter. EDS (Fig. 6.5f), along with XRD (Fig. 6.4c), confirms that these coating phases were TiC. On the other hand, EDS (Fig. 6,5c) reveals that the original GNS composed only of carbon phase (Fig. 4.5c). A minor oxygen (O) peak was noticed from both samples which could be attributed to tiny oxidation of the samples. The presence of Si peak in both spectra corresponds to the silicon-wafer substrate used for supporting the investigated materials.

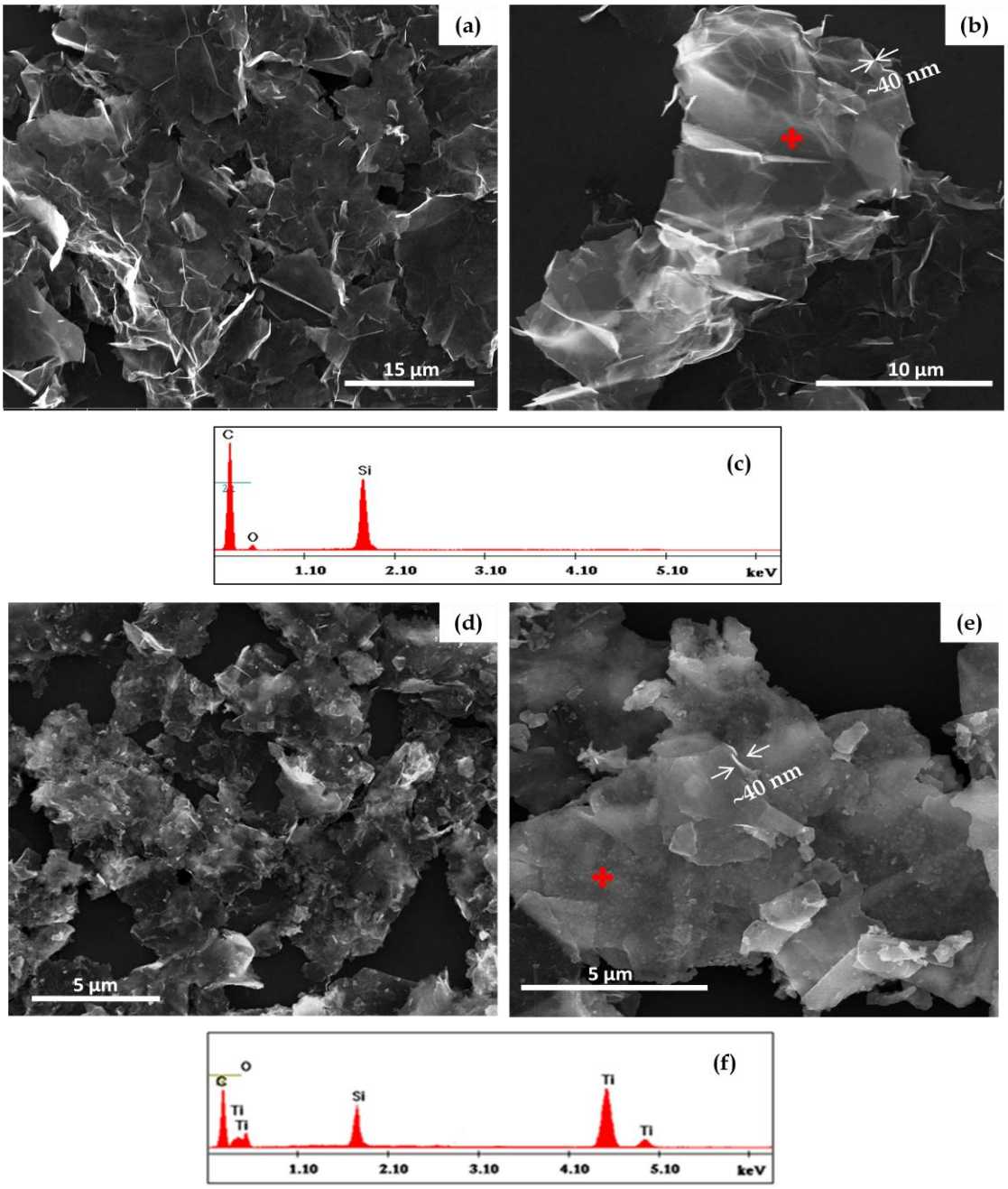

Figure 6.5 SEM images of (a, b) as-received GNS and (d,e) as-prepared TNS. EDS spectra of (c) as-received GNS and (f) as-prepared TNS.

The morphologies of original GNS and as-prepared TNS can be seen more clearly by HRTEM (Fig. 6.6). Both materials exhibited obviously 2D-nanostructure with micro-lateral sizes indicating their large specific area.

Compared with smooth surfaces of the original GNS (Fig. 6.6a), rougher surfaces composed of nanosized (~20 nm) particles were found on the as-prepared TNS (Fig. 6.6b).

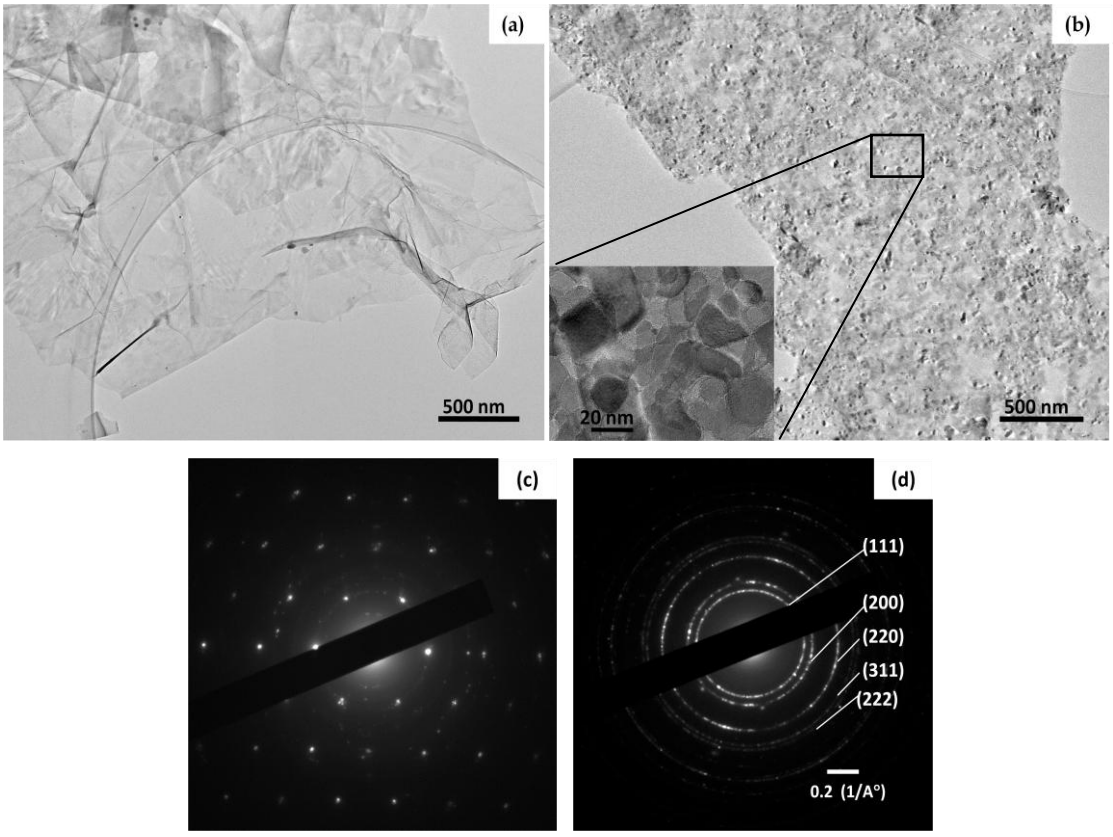

Figure 6.6 HRTEM images and SAED patterns of (a,c) GNS and (b,d) the as-prepared TNS, respectively.

SAED patterns further confirm that the synthesised nanosheets were TiC (based on the obtained diffraction rings of cubic TiC) (Fig. 6.6d). Those rings could be indexed to the (111), (200), (220), (311) and (222) planes, in which their relative intensities were in well accordance with the results obtained from XRD (Fig. 6.4(c)). In contrast, the original GNS displayed diffraction spots of hexagonal graphitic structure.

Figure 6.7 demonstrates stacking sequences of the as-prepared TNS. As shown in Fig. 6.7, the lattice interlayer distance was measured as around 0.25 nm, which corresponds to the (111) plane of cubic TiC. These lattice fringes, however, arranged in different orientations (indicated by the white arrows), indicating polycrystalline characteristics of the as-prepared TNS. This is in good agreement with the obtained diffraction rings from the SAED pattern (Fig. 6.6d).

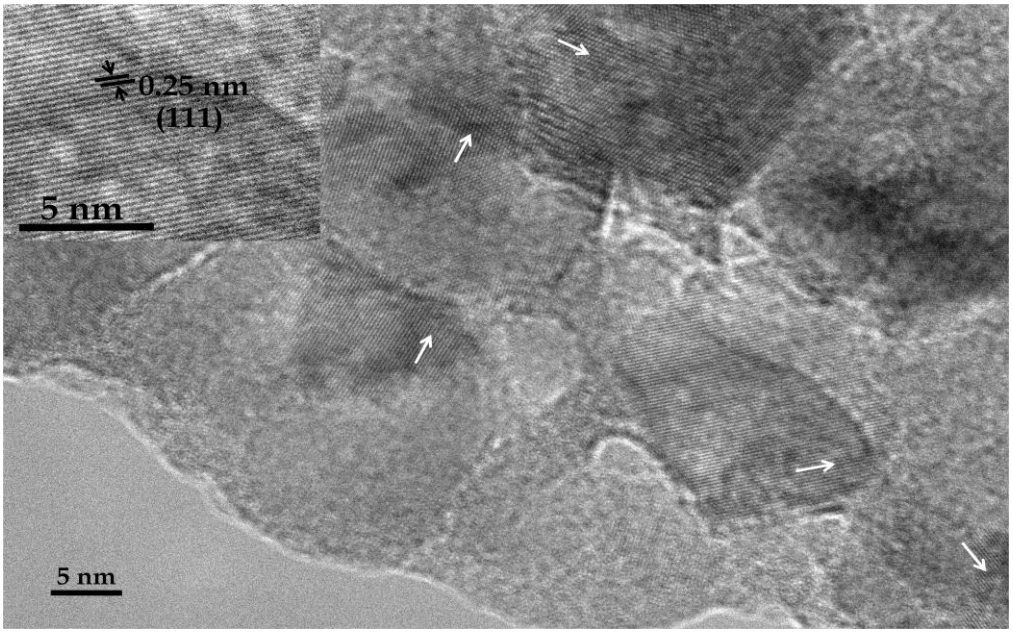

Figure 6.7 HRTEM image revealing stacking sequences of the as-prepared TNS.

6.3.1.4 Raman spectra of the synthesised TNS

Raman spectra of the as-received GNS and the as-prepared TNS were compared in Fig. 6.8 to further confirm phase compositions and purity of the resultant nanosheets.

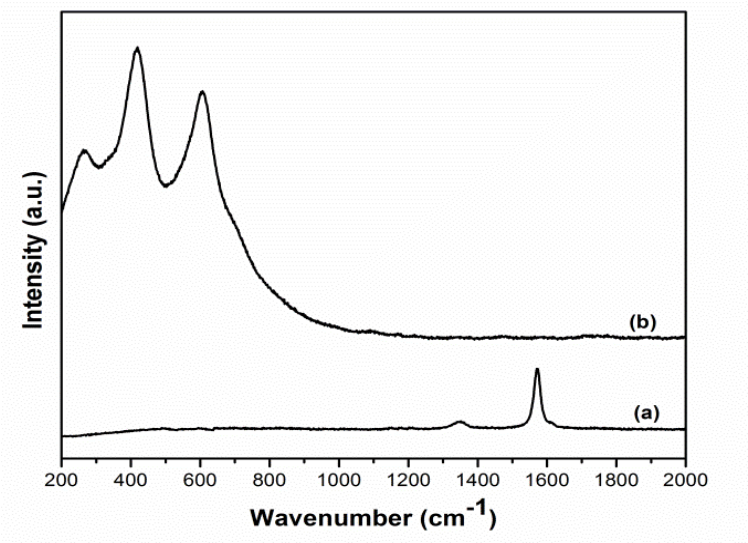

Figure 6.8 Raman spectra of (a) the starting GNS and (b) the as-prepared TNS.

As shown in Fig. 6.8, the spectrum of GNS exhibited the two typical Raman bands of graphitic structure corresponding to the centre values of D and G bands located at about 1347 and 1586 cm^{-1}, respectively. The G band indicates the tangential vibration of the carbon atoms in the graphitic layers. Whereas, the D band represents defect level in the GNS due to the disordered carbon atoms [15]. On the other hand, in the TNS spectrum, the three obvious peaks located at approximately 262, 418, an 610 cm^{-1} were observed which correspond to the vibration mode of Ti-C bonds. The findings are in good agreement with the reported studies of Rohse et al. and Chen et al. [220, 221]. However, it was claimed that stoichiometric cubic TiC has no Raman active vibrational modes due to every atom sitting at a site of inversion symmetry [222]. Thus, the presence of those three Raman peaks indicated that the as-prepared TNS were not completely stoichiometric. In addition, Chen et al. [221] suggested that the first-order Raman spectrum (at 262 cm^{-1}) may be caused by defects in the product structure. Such defects include carbon vacancies, surface defects, edge defects and dangling bonds which normally exist in the non-stoichiometric TiC materials.

6.3.2 Fabrication and characterisation of TiC-coated graphite nanosheets (TCNS)

6.3.2.1 Effects of processing temperatures on the TCNS synthesis

Figures. 6.9 and 6.10 illustrate XRD of samples with Ti/C = 1/2 and 1/4 (by molar ratios) respectively, after heating for 5 h at 850, 900 and 950 °C, in comparison with the XRD pattern of as-received GNS.

As shown in Fig. 6.9a, the pristine GNS composed only of graphite phase as indicated by the two evident peaks at $2\theta \approx 26.85°$ and 53.70° which correspond respectively to the (002) and (004) diffraction planes of graphite. On the other hand, three crystalline phases of graphite, Ti, and TiC were detected in the fired samples (Fig. 6.9b-c). Furthermore, with increasing the temperature, TiC peaks increased evidently, while Ti and C peaks decreased, indicating a significant influence of the synthesis temperature on the reaction rate and the growth of TiC. When the reaction system was processed at 950 °C, the Ti peak was invisible indicating the complete consumption of Ti (Fig. 6.9d).

Similar phases were also identified in the samples with Ti/C = 1/4, although as shown in Fig. 6.10, the carbon peaks intensity in this case was much higher than that in the case of the sample with Ti/C = 1/2, indicating a higher level of carbon remaining in the sample (Fig. 6.9). Furthermore, after 5 h of firing, Ti disappeared and only TiC was seen along with unreacted carbon at 900 °C (Fig. 6.10c), indicating a complete reaction at such a low temperature. On further increasing the temperature to 950 °C, no further phase changes were seen, though the peaks of TiC became slightly sharper (Fig. 6.10d), suggesting its enhanced crystallinity or grain growth.

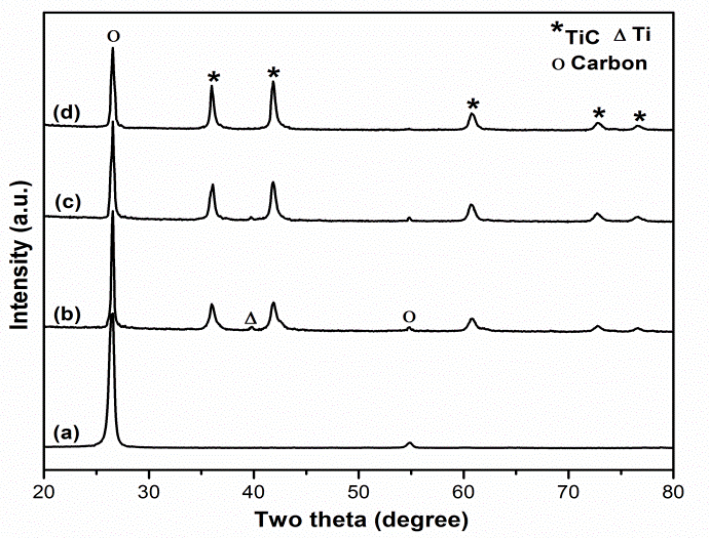

Figure 6.9 XRD of (a) the as-received GNS, and samples with Ti/C = 1/2 (by molar ratio) heated for 5 h at (b) 850, (c) 900 and (d) 950 °C.

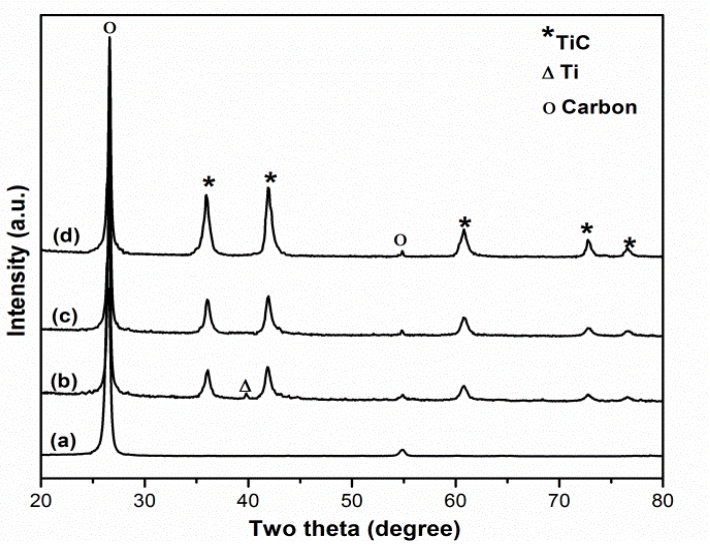

Figure 6.10 XRD of (a) the as-received GNS, and samples containing Ti/C = 1/4 (by molar ratio) heated for 5 h at (b) 850, (c) 900 and (d) 950 °C.

6.3.2.2 Microstructure observations of as-synthesised TCNS

Figure 6.11 demonstrates the microstructures of as-received GNS and as-prepared TCNS, showing that the TCNS retained to a large extent the

morphologies of as-received GNS (ultrathin sheets with an averaged lateral size around 10 μm). Unlike in the case of TNS preparation, the phenomenon of breaking the original bigger sheets into smaller pieces was not evident in this case, indicating that the coating nanosheets are resistant to sonication power performed in the dispersion process, probably due to the presence of GNS underneath the TiC coating layers. It is well known that hard materials such as ceramics possess low toughness [223]. Because of this and the ultrathin nature as well as large surface area, some of the synthesised TNS were split into smaller nanosheets by the mild sonication, whereas the as-prepared TCN S were not and so retained the original size of GNS templates.

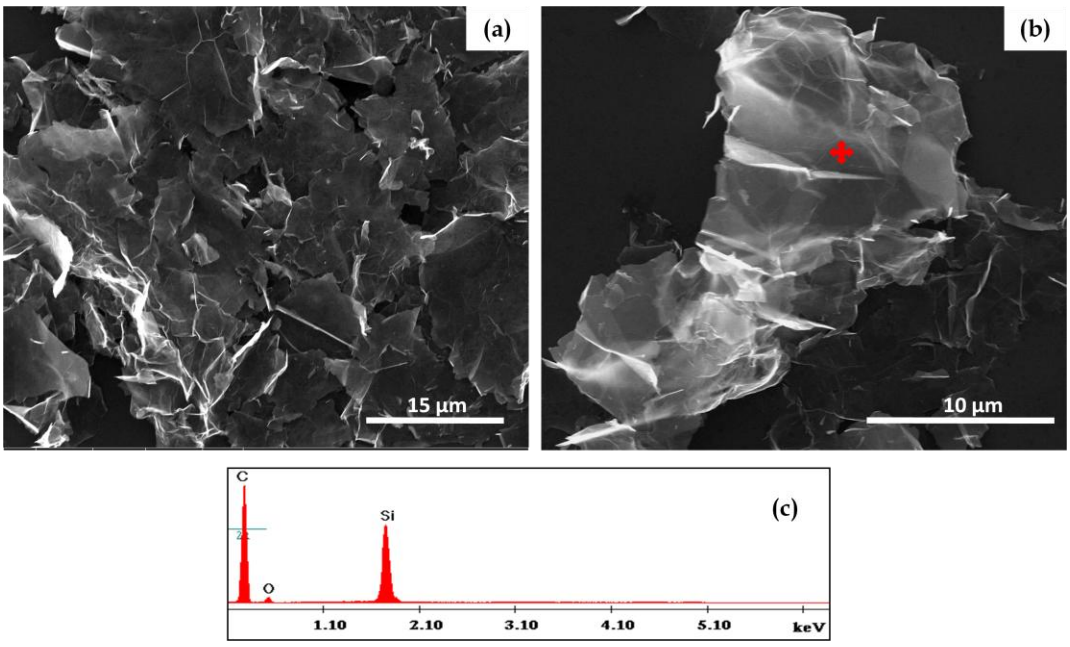

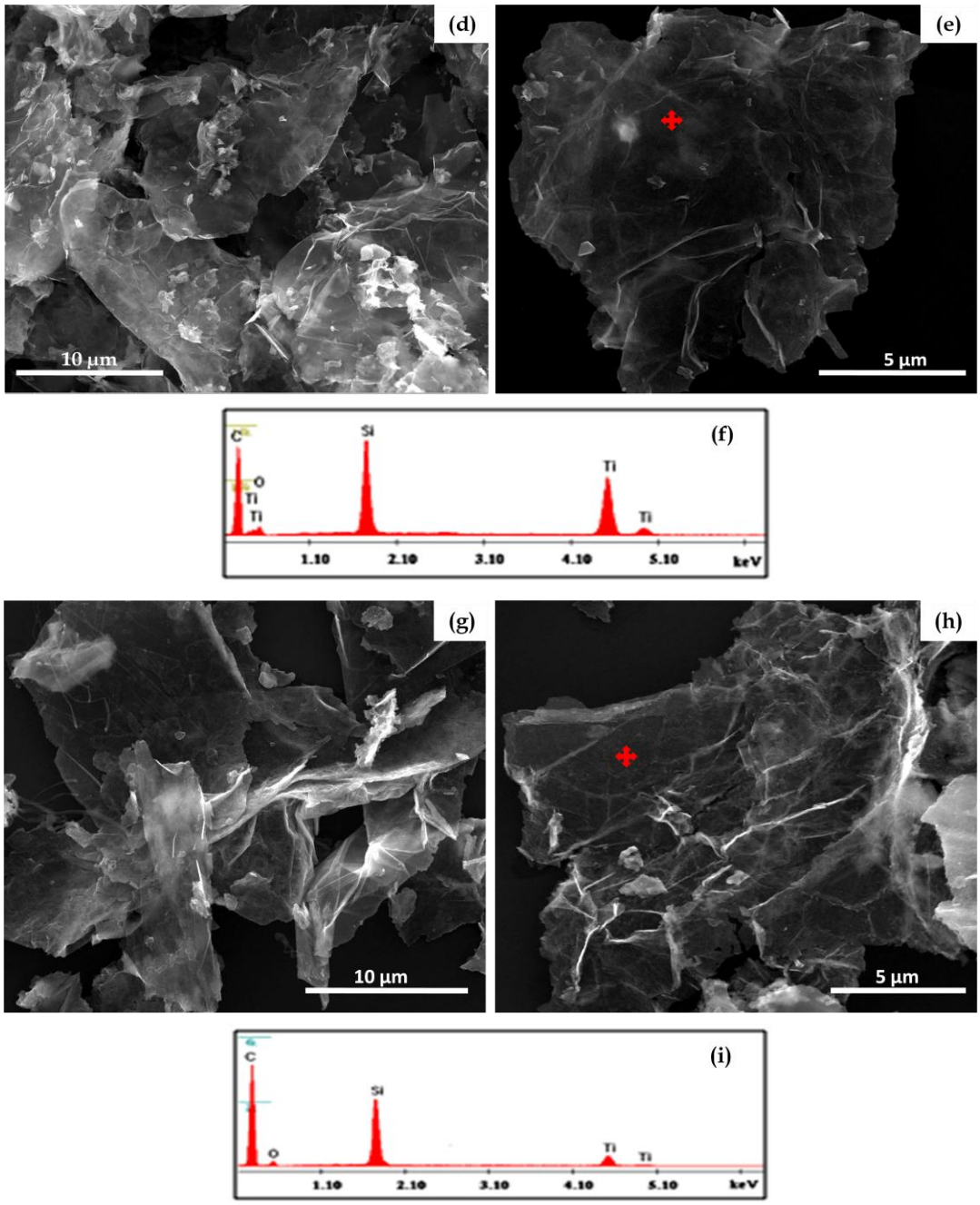

Figure 6.11 SEM images of the as-received GNS (a,b) and the TCNS with different molar ratios of (d,e) Ti/C=1/2 and (g,h) Ti/C=1/4. EDS spectra of (c) the pristine GNS and the synthesised TCNS: (f) with Ti/C=1/2 and (i) with Ti/C=1/4.

HRTEM further confirms that the as-prepared products, synthesised from Ti/C=1/4 (Fig. 6.12c) and Ti/C=1/2 (Fig. 6.12e), retained well the 2D-nanostructure of the GNS templates. Compared with the smooth surfaces of uncoated GNS (Fig. 6.12a), the TCNS displayed rougher surfaces, but crack-free coatings composed of TiC nanocrystals. SEAD patterns gained from the coating products (Figs. 6.12d,f) exhibited diffraction rings of two phases, one is TiC and the other is graphite. Those rings could be indexed to the (111), (200), (220), and (311) planes of cubic TiC, and the (002) and (004) diffraction planes of graphite. Among those diffraction planes, the (002) plane, obtained from the TCNS with Ti/C=1/4, exhibited strongest intensity revealing high crystallinity and volume fraction of graphite phase in the sample. This finding is in well accordance with XRD results in Fig. 6.10 showing the highest intensity of graphite peak at (002) reflection plane. However, the intensity decreased significantly, while the intensities of TiC diffraction planes became noticably stronger (Fig. 6.12f), with the increased Ti concentration (Ti/C=1/2), suggesting the reduction in volume fraction of graphite and the increased volume fraction of TiC phase in the sample.

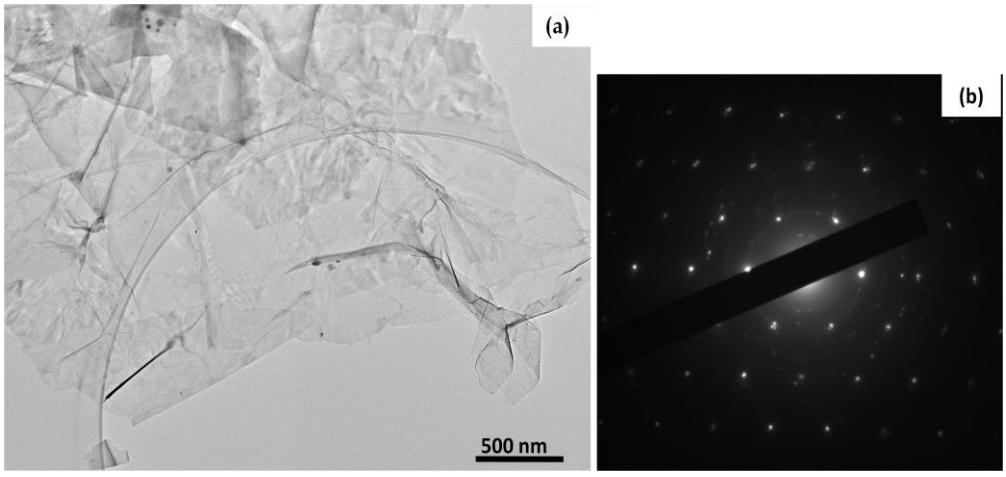

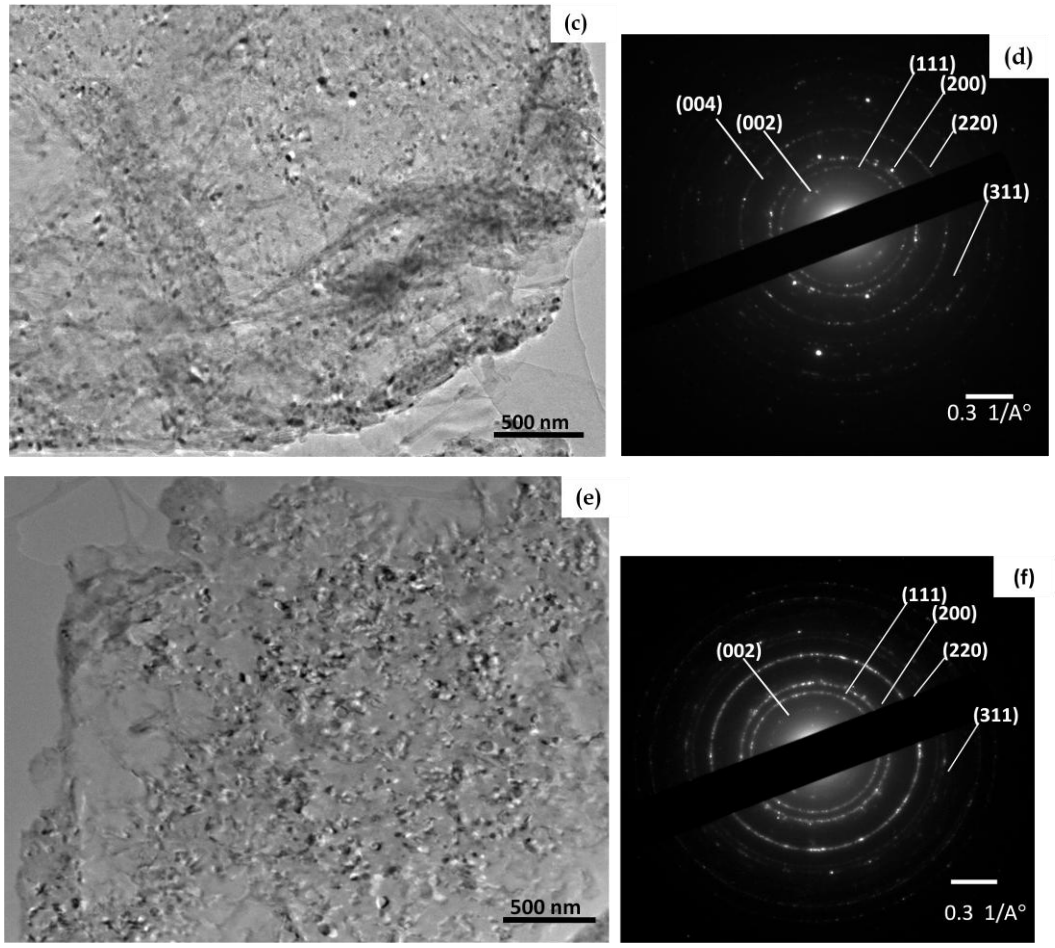

Figure 6.12 TEM images and SAED patterns, respectively, of (a,b) the as-received GNS and the as-prepared TCNS with (c,d) Ti/C=1/4, and (e,f) Ti/C=1/2.

6.4 Reaction mechanism

The as-prepared TiC nanosheets (TNS) and TiC-coated graphite nanosheets (TCNS) retained the nanosheet-shape and size of the original graphite nanosheets (GNS) indicating the template growth mechanism had dominated the synthesis process, in which the GNS had acted as templates. This suggests that, in the molten KCl, the GNS are much less soluble than the metallic Ti powder. The main stages involved in the synthesis can be illustrated in Fig. 6.13 and discussed as follows.

At the test temperatures, KCl melted itself forming a liquid reaction medium accelerating diffusion rates of the dissolved species in it. In this melt, Ti partially dissolved [224-227] and then diffused rapidly through the liquid medium onto the surfaces of GNS and subsequently reacted to in-situ form TiC via Reaction (6.1), which maintained shapes and sizes of the original GNS. At this stage, it is believed that the reaction occurred firstly on the outer layer of the template and gradually proceeded to the inner ones. Therefore, when the molar ratio of Ti to C was equal (stoichiometric), the GNS were completely converted to TiC nanosheets. On the other hand, when the molar ratio of Ti to C is less than 1, the outer layers of the starting GNS was firstly converted to TiC coating phase leaving their inner layers uncoated. As a result, TiC coated graphite nanosheets were finally resulted.

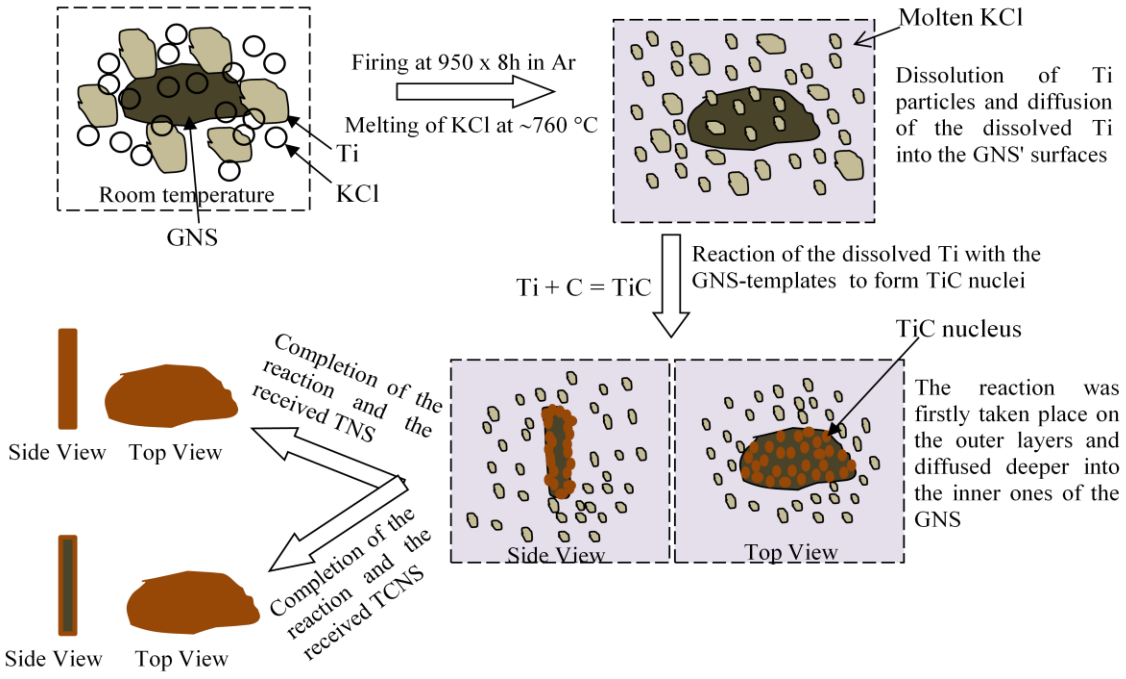

Figure 6.13 A schematic diagram illustrating the template growth mechanisms in the MSS of TNS and TCNS.

6.5 Conclusions

The fabrications of novel TiC nanosheets (TNS) and TiC-coated graphite nanosheets (TCNS) were acheived via the direct reaction of metallic titanium (Ti) with graphite nanosheets (GNS) at as low as 950 and 900 °C, respectively, in a molten KCl salt under a constant flow of argon. The processing time required for preparing TNS was 8 h, whereas that employed for synthesising the TCNS was 5 h. The synthesis temperature and time required for completing the reaction decreased with the reduction in molar ratios of Ti to C. Ti/C ratio also affected the volume fractions of unreacted GNS and the formed TiC phases. SEM analysis revealed that as-prepared TNS and TCNS were ultrathin sheets with an average lateral size around 10 μm, which were similar to those of the original GNS. The well preservation in shapes and sizes of the original GNS suggested that the template growth mechanism had governed the reaction synthesis, and GNS acted as both carbon source and reaction templates. While the as-received GNS displayed smooth surfaces, the as-prepared TNS and TCNS exhibited rougher surfaces. HRTEM revealed that those rougher surfaces composed of around 20 nm TiC nanocrystals with different orientations in the nanosheets. It is believed that the MSS developed here could be potentially used to prepare a range of other types of carbide nanosheets (e.g., ZrC, NbC and TaC nanosheets) which were difficult to be prepared via the conventional routes reported previously.

Chapter Seven

Low Temperature Synthesis and Characterisation of Titanium Carbide (TiC) Foam from Molten Salts

---

7.1 Introduction

Because of its many attractive properties such as lightweight, variable porosity, low thermal conductivity, high permeability, and high resistance to chemical attack [228], porous ceramics are regarded as good candidate materials for many important applications, e.g. in catalyst carriers, filters, gas separators, thermal insulators, and absorbers [66, 129]. Recently, a wide range of porous oxide, boride and carbide ceramics have been prepared and investigated. Among these materials, porous carbides, in particular, have attracted a great deal of research interest because of their high melting points and high hardness and thus great application potentials in high-temperature industries such as metallurgy and refractory industries.

Various technologies have been developed to date for synthesising porous ceramics, including replica technique, pore forming agent method, sol–gel technology, and the self-propagating high-temperature synthesis (SHS) process. However, these techniques suffered from various drawbacks, including high processing temperature, residual impurities, low porosity volume, difficulty in controlling the desired final pore size and structure, complicated operating process, and high production cost [18, 19, 130, 133, 134, 229, 230].

In the work presented in this Chapter, the molten salt synthesis (MSS) technique developed with the preparation of TiC nanosheets and TiC coated graphite nanosheets (see Chapter 6) has been extendedly used to synthesise macroporous TiC foam with a well-defined microstructure (Fig. 7.1). The resultant TiC foams were carefully characterised and the results, along with the relevant reaction mechanisms discussed.

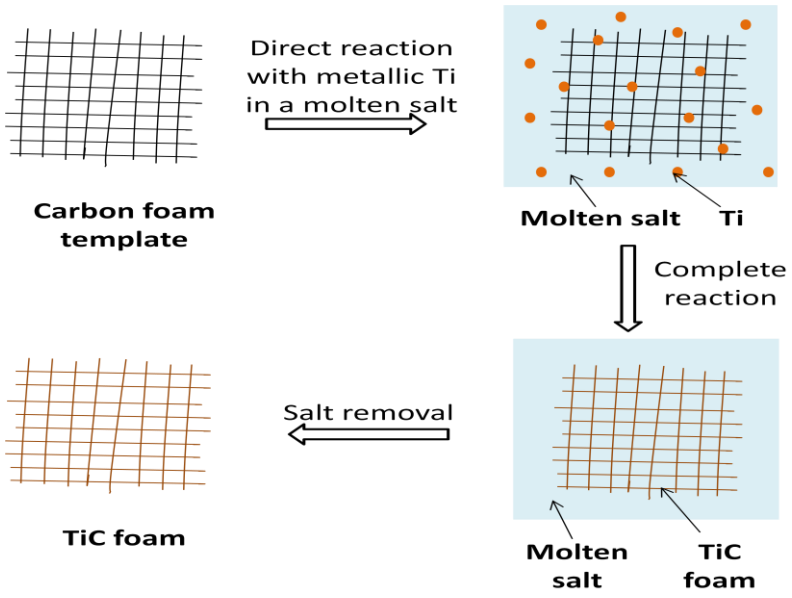

Figure 7.1 Scheme of molten salt processing route employed for fabricating TiC foams.

7.2 Experimental

7.2.1 Raw materials

Carbon vitreous foam (CF, porosity: 96.5%, density: 0.05 g/cm^3), metallic titanium powder (Ti, 99.6% purity) and potassium chloride (KCl, 99% purity) were used as starting raw materials. The CF was received from Goodfellow Cambridge Ltd., UK and the others were supplied by Sigma Aldrich, UK.

7.2.2 Sample preparation

The as-received CF was cut into small pieces with the dimensions of 15 x 15 x 6.3 mm^3. Metallic titanium powder (Ti) and CF were weighed according to stoichiometric requirement indicated by reaction (7.1).

$$Ti + C = TiC \qquad (7.1)$$

The required Ti was mixed homogeneously with KCl in a mortar gate. The weight ratio of reactants to salt is 1/40. At first, one-quarter of the mixture was loaded into an alumina crucible followed by centred placing the CF and then adding the rest of mixture powder into the crucible. The crucible was covered with a lid and charged into the heating zone of an argon protected furnace. The furnace was then heated to a designed temperature between 950 and 1050 °C and held for 4h before being cooled down at the same rate to room temperature. The reacted sample was washed repeatedly in hot distilled water to remove the residual salt and oven-dried overnight at 100 °C prior to further characterisation. An overview of sample preparation for fabricating TiC foam is presented in Fig. 7.2. Sample compositions and heating profiles for the synthesis are presented in Table 7.1.

Table 7.1: Sample compositions and heating profiles for synthesising TiC foams.

Sample ID	*Raw material used (g)*		*Salt : Reactants*	*Heating profiles*
	Ti	C	*(weight ratio)*	*(℃) x 4 h*
TF950	0.24	0.06	40:1	950
TF1000	0.24	0.06	40:1	1000
TF1050	0.24	0.06	40:1	1050

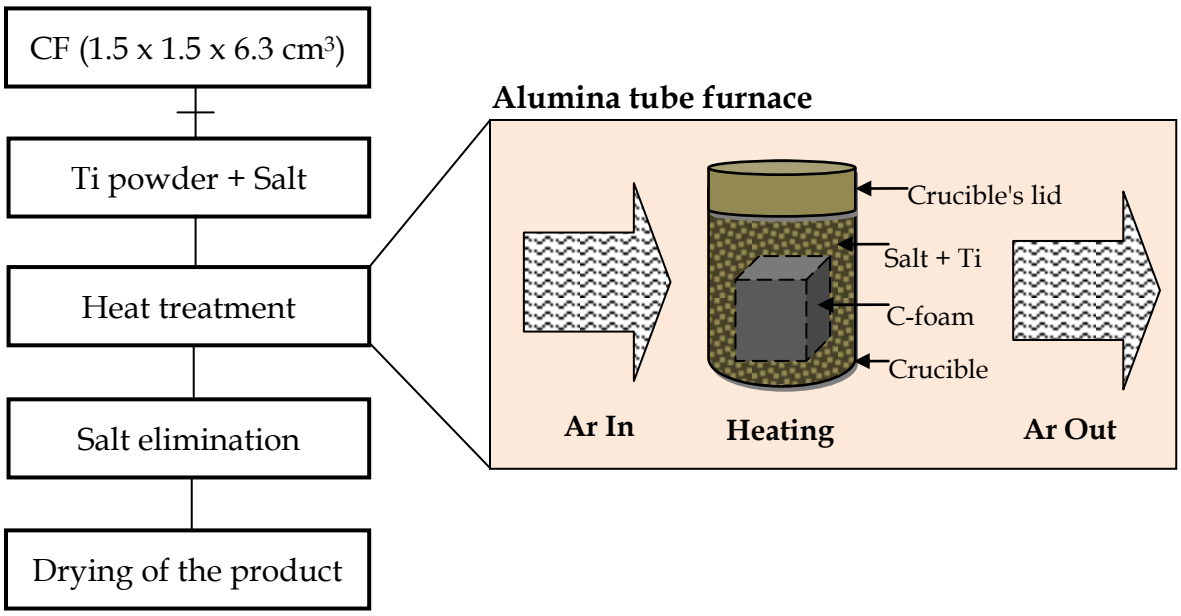

Figure 7.2 Scheme of MSS of macroporous TiC from carbon vitreous foam (CF)

7.2.3 Sample characterisation

Phase compositions in the as-prepared product powder were identified by powder X-ray diffraction (XRD) analysis (Siemens D500 reflection diffractometer). Spectra were recorded at 30 mA and 40 kV using Ni-filtered Cu Kα radiation. The scan rate was 2°/min with a step size of 0.05°. ICDD cards used for the identification are TiC (32-1383) and Ti (65-9622). The microstructure

of the fabricated foams was investigated using a field emission gun scanning electron microscope (FESEM Inspect F). Cell and pore size distributions were evaluated by measuring microstructural parameters (cell and pore sizes) using quantitative image analysis of SEM micrographs. Density of the samples were evaluated as the ratio of mass to volume (equation (7.1)). Because the evaluated samples were solid with geometrical shapes, their dimensions could be directly measured using a Vernier calliper to determine the bulk volumes.

$$\rho = \frac{W}{V} \qquad (7.1)$$

where,

ρ = Density of the sample (g/cm^3)

W = Weight of the sample (g)

V = Volume of the sample (cm^3)

7.3 Results and discussion

7.3.1 Conversion to TiC foam

Figure 7.3 shows phase evolution in the mixture of Ti and CF after 4 h of firing in KCl molten salt at various temperatures. At 950 °C, TiC peaks were observed, along with unreacted carbon (indicated by the broad peak) and Ti peaks (Fig. 7.3b). At 1000 °C, TiC peaks increased, while Ti peaks decreased, indicating the enhanced reaction rate with temperature (Fig. 7.3c). On further increasing temperature to 1050 °C, Ti and the broad carbon peaks disappeared completely and only TiC was identified in the resultant sample (Fig. 7.3d), indicating the complete conversion of carbon foam to TiC foam.

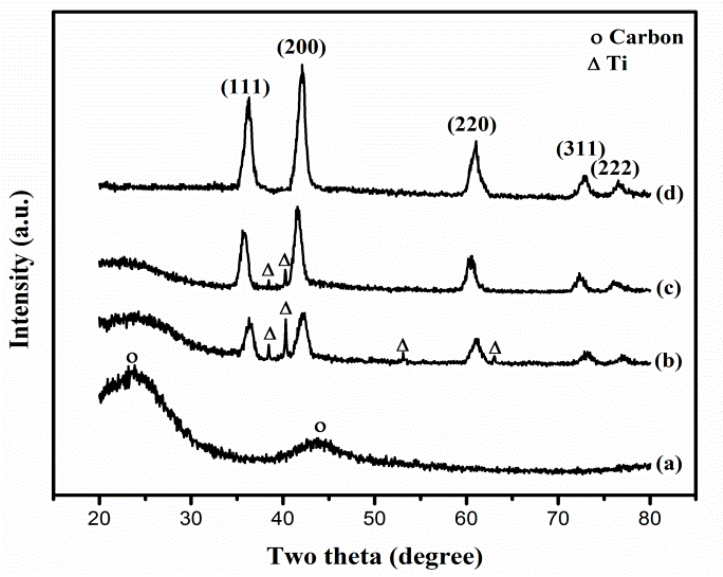

Figure 7.3 XRD patterns of (a) the as-received CF and the resultant foams heated for 4 h at (b) 950, (c) 1000 and (c) 1050 °C.

7.3.2 Macro- and microstructural observations

Macro-photographs and scanning electron micrographs of the as-received CF and the as-prepared TiC foams are shown in Fig. 7.4a-b and Fig. 7.5a-b, respectively.

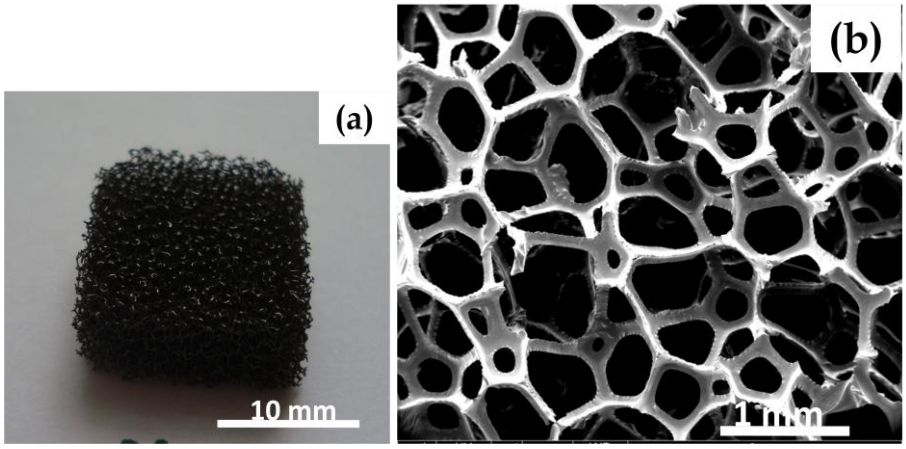

Figure 7.4 (a) Macro-photograph and (b) SEM image of the as-received CF.

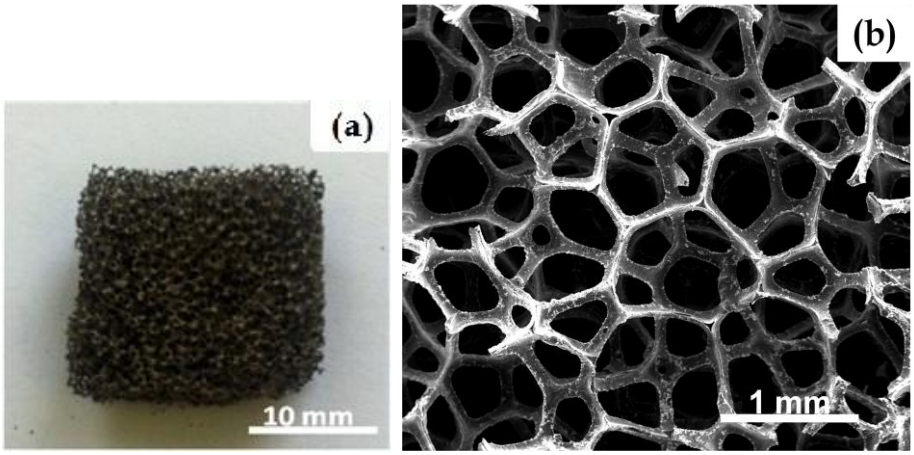

Figure 7.5 (a) Macro-photograph and (b) SEM image of the synthesised TiC foam after firing at 1050 °C for 4 h in Ar.

As shown in Figs 7.4 and 7.5, the as-received carbon foam displayed the black color of carbon (Fig. 7.4a) while the resulting TiC foam exhibited light gold color of TiC (Fig. 7.5a). The micrographs shown in Figs. 7.4b and 7.5b revealed that both CF and reacted foams possessed a three-dimensionally interconnected macroporous structure with pore sizes of 300-400 μm. Furthermore, pore windows of the as-prepared TiC foam were clear of any other materials, e.g. the unreacted carbon foam. The well defined open-cell structure of the resultant TiC foam, as compared with that of the starting carbon foam, indicated that template growth mechanism [156, 231] had played an important role in the synthesis process. Moreover, surface morphologies of the as-received CF and the as-prepared foams were compared in Fig. 7.6.

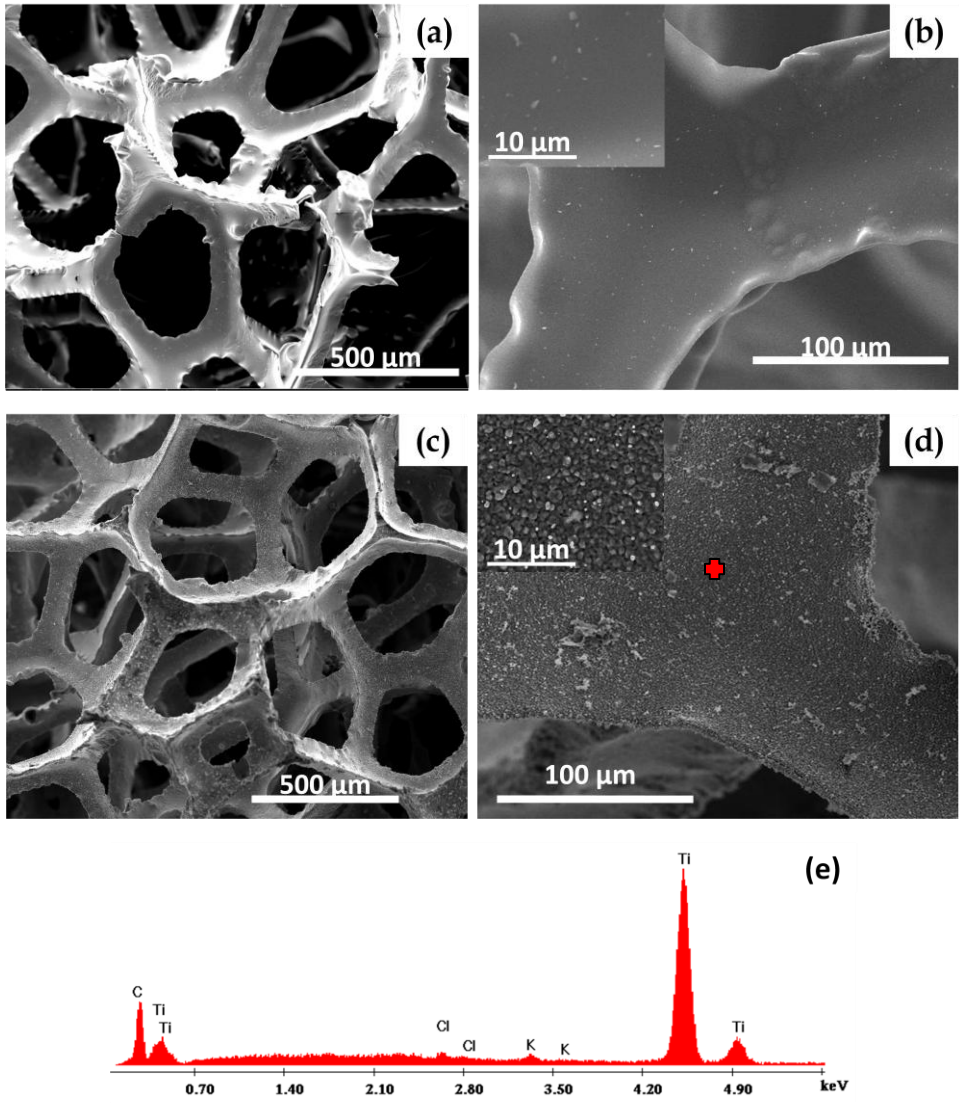

Figure 7.6 SEM images of (a,b) the pristine CF and (c,d) the as-prepared TiC foam at different magnifications. EDS spectra (e) obtained from point scanning on the selected area (noted by red mark on the image (d)) of the reacted foam.

The cell walls in the pristine carbon foam appeared to be smooth (Fig. 7.6b) while those in the as-prepared TiC foam were rougher (Fig. 7.6d). Similarly to the observations in the cases of TiC nanosheet and TiC coated graphite nanosheet preparation, the rougher surface of cell walls observed in the present case was

also attributable to the formation of nanocrystals as shown by the inset in Fig. 7.6d. EDS further confirms that those nanocrystals were TiC (Fig. 7.6e). In addition, the cell networks in the prepared TiC foams displayed a feature of crack-free as well as uniform *in situ* reaction of titanium and carbon. The struts were also hole- and crack-free. Besides, the pores were clear of any unwanted phases such as impurities and/or membranes. Such a structure would be beneficial to the better liquid or gas filtrations due to its high liquid/gas permeability. In the case of using the conventional replica technique, the synthesised foams usually consisted of thin membranes covering the pores [18, 19, 130, 232], leading to increased density of the produced material and decreased permeability of fluids and gases through the blocked pores. For these reasons, when the replica technique was used, an extra process (pyrolysis) was usually required to burn out those covering membranes. Also, a high processing temperature (1100-1600 °C) was normally required, which could result in shrinked products [18]. Another problem with the replica technique was that porous materials prepared often contained surface cracks due to non-uniform coating of the polymeric foams, especially at the edges of the struts, by the ceramic slurries [232, 233]. The MSS developed with the present work does not suffer from these disadvantages. In addition, with MSS, pore sizes of the final porous products could be well controlled, which was difficult to be achieved with other conventional techniques such as the pore forming agent technique.

7.3.3 Influence of reaction temperature on the cell structures

The macro-photographs and scanning electron micrographs of TiC foams resulted from 4 h of firing at 950 and 1000 °C are shown in Figs. 7.7 and 7.8, respectively. The reactions in both cases were incomplete.

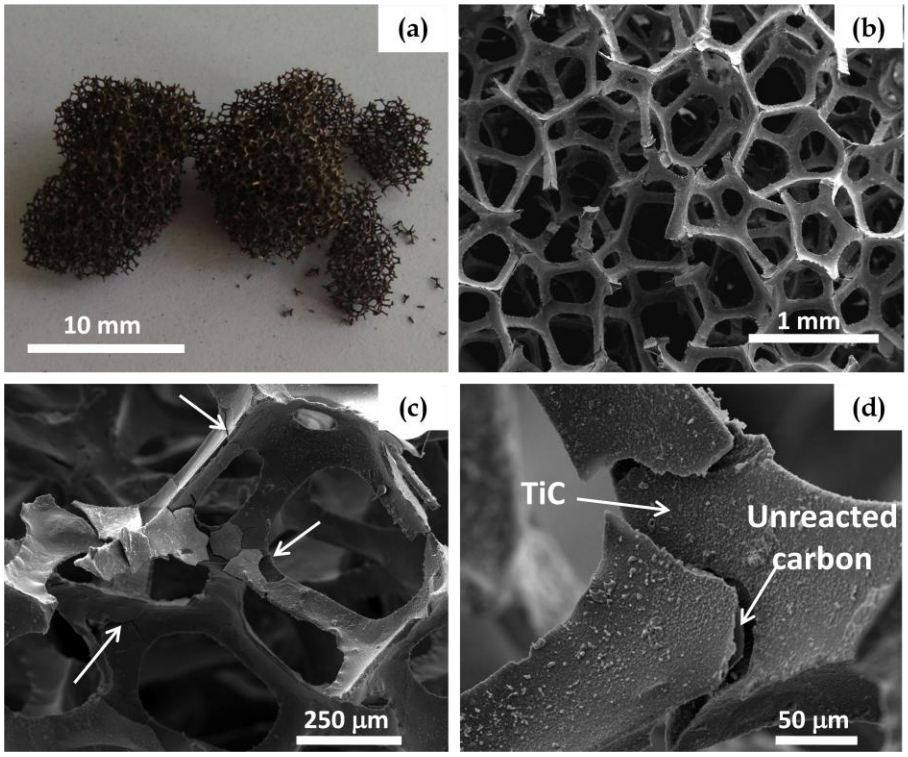

Figure 7.7 (a) Macro-photograph and (b,c,d) SEM images of the reacted TiC foam at different magnifications, respectively, heating for 4 h at 950 °C.

As shown in Fig. 7.7a, after reaction at 950 °C, the foam was split into small pieces indicating the severe destruction of cell-networks in this case. Upon heating at 1000 °C, the destruction was still obvious (indicated by the white arrows in Fig. 7.8a) but the extent was lower than that in the case at 950 °C. On further increasing the temperature to 1050 °C, the reaction was completed, and the resultant foam maintained a perfect open-cell network structure (Fig. 7.5) similar to that of the original CF (Fig. 7.4). These results confirmed that the extent of network destruction decreased with increasing the temperature and the original porous structure could be retained if the reaction was completed. This indicated that the synthesis temperature influenced significantly the cracking and breaking of the cell structures. This was considered to be related to the

thermal stress arising from the mismatch in the thermal expansion coefficients (CTE) of TiC and unreacted carbon. CTE of the vitreous carbon foam at 100-1000 °C is 3.2 × 10^{-6} $°C^{-1}$ (provided by the supplier) while that of TiC at 1000 °C is 8.31±0.68 x 10^{-6} $°C^{-1}$ [234]. Such a big difference in the CTE values could result in great thermal stress during the cooling process, which led to cracking and breaking of the cell-linking networks (Figs. 7.7 and 7.8). It is considered that cracks started at the interfacial region of the two phases and/or at the cell-connections as indicated by the white arrows in Figs. 7.7d and 7.8d. After firing at 950 and 1000 °C, the formed TiC layer was peeled off, revealing clearly the unreacted layer of original CF (Fig. 7.7c-d). This observation additionally confirmed that template growth mechanism had governed the TiC formation.

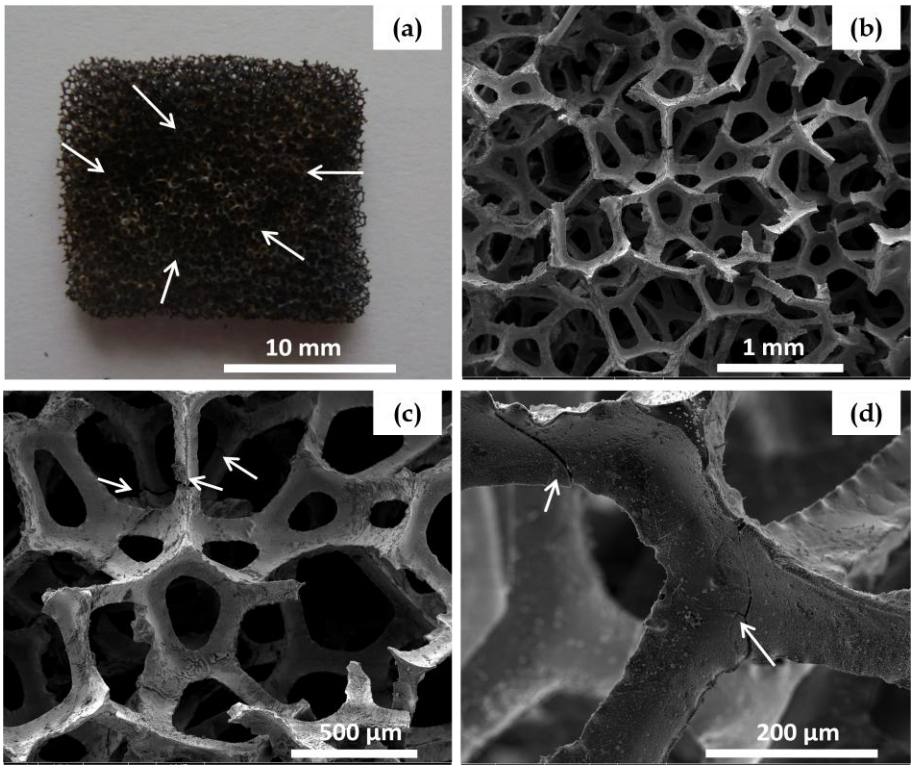

Figure 7.8 (a) Macro-photograph and (b,c,d) SEM images of the reacted TiC foams at different magnifications, respectively, heating for 4 h at 1000 °C.

7.3.4 Density and pore size distribution

Table 7.2 shows density values of the foams resultant from firing at each temperature, along with that of the as-received carbon foams.

Table 7.2: Densities of the as-received CF and the as-prepared TiC foams.

Materials	*Heating temperature (°C)*	*Phases presented in XRD curves*	*Density (g/cm^3)*
Pristine CF	-	C	0.052
Reacted foam	950	TiC, C, Ti	0.082
Reacted foam	1000	TiC, C, Ti	0.155
Reacted foam	1050	TiC	0.194

The averaged density of as-received CF is 0.052 g/cm^3 which is in good consistance with the density value provided by the supplier (0.05 g/cm^3). It is noticed that, after reaction, density of the as-prepared foams increased from 0.052 g/cm^3 at room temperature to 0.082, 0.155, and 0.194 g/cm^3 at 950, 1000 and 1050 °C, respectively. This is attributed to the increasing in TiC phase and decreasing in carbon phase with the temperature. The density value became maximum (0.194 g/cm^3) when the foam was composed of only TiC phase (resultant from firing at 1050 °C). This corresponds to 96.04% porosity in the final structure (based on the theoretical density of TiC 4.93 g/cm^3 as taken from the literatures [235, 236]). This is close to that of the carbon template (96.50%) reported by the supplier. Clearly, by using the MSS technique developed here, TiC foams with well-defined open-cell structure and desired porosity volume could be readily prepared.

As shown in Figs. 7.4b and 7.5b, the foams exhibited approximately spherical cells and pores. Furthermore, the pore windows of the as-prepared TiC foam (Fig.

7.6c) were free of any other impurities or membranes which could cause pore-size reduction. Therefore, it could be considered that the increased density of as-prepared foams with temperature was mainly caused by the increased amount of TiC in the samples.

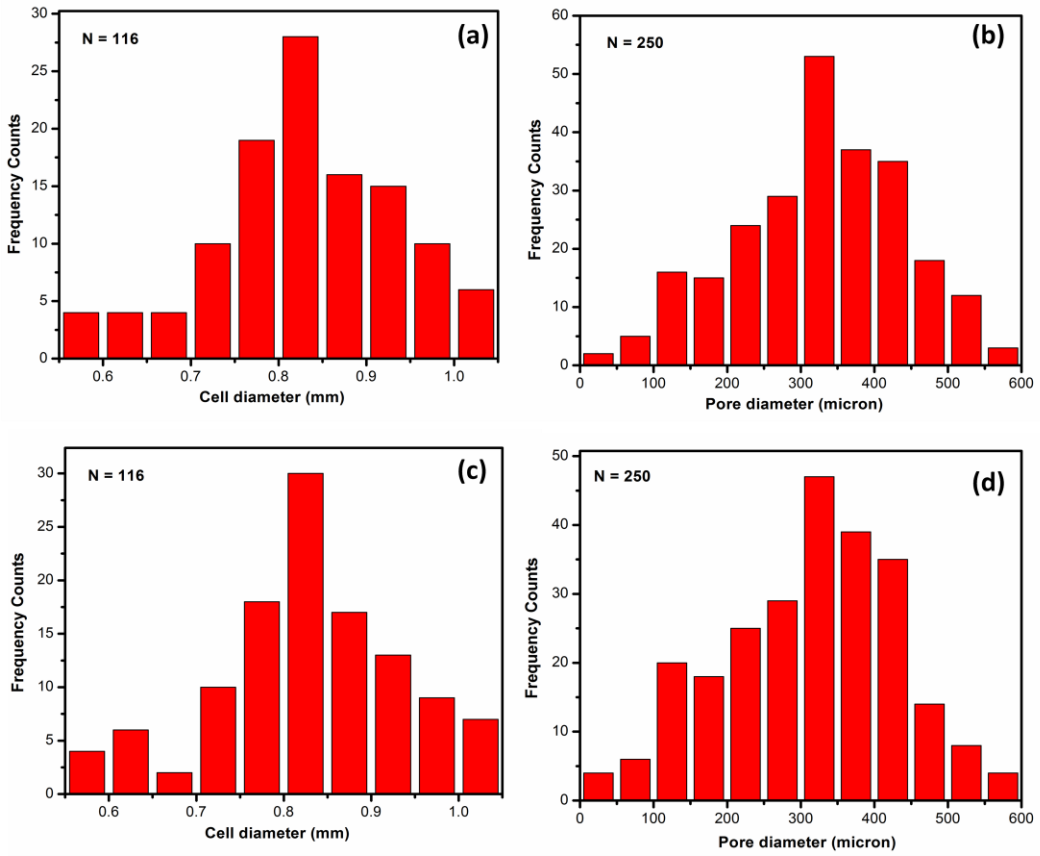

Figure 7.9 Cell and pore size distributions of (a and b, respectively) the pristine carbon and (c and d, respectively) the as-prepared TiC foams.

Figure 7.9 shows cell and pore size distributions of the as-received CF in comparison with those of the as-prepared TiC foams. The mean cell diameter of the original CF and the synthesised TiC foam were identical at 0.85 mm and their cell distributions were in the same range of 0.5-1.05 mm (Figs. 7.9a and 7.9c). Both materials exhibited similar pore size distributions (Figs. 7.9b and 7.9d) with

the mean pore diameter of 300-400 μm and a distribution range of 30-600 μm. These results indicated that TiC foams with a well-defined open-cell structure could be readily formed via the MSS route developed with this work.

7.4 Reaction mechanism

Because the resultant foams preserved well shapes and sizes of the original CF, a similar template growth mechanism to that suggested in the case of MSS of TiC nanosheets (Chapter 6) can be proposed. Clearly, in this present case, CF had fuctioned as both carbon source and reaction templates. At the test temperatures, Ti partially dissolved in the KCl melt [224-226] and then diffused onto the surfaces of CF and subsequently reacted to form in-situ TiC. As shown in Fig. 7.10, TiC layer was initially generated at the surfaces of CF. With increasing temperature, the TiC layer became thicker, while the unreacted carbon phase became less. Due to the enhanced reaction rate at 1050 °C, the entire conversion from the original CF to TiC foam was finally achieved.

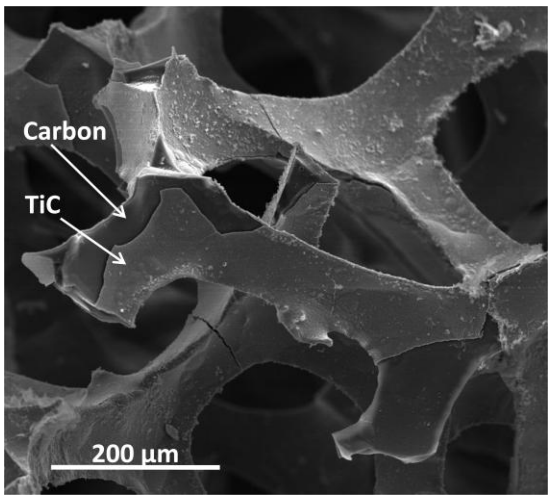

Figure 7.10 TiC coating layer occasionally peeled off from the remaining unreacted CF-template in the sample after 4 h of firing at 950 °C in Ar.

7.5 Conclusions

Open cellular TiC foams with a well defined structure of three dimensionally interconnected TiC networks were prepared at 1050 °C for 4 h via the direct reaction of metallic titanium with carbon foam template in KCl. The as-prepared TiC foams possessed low density of 0.194 g/cm^3 and high porosity of 96 % with an average pore size of 300-400 μm and pore size distribution of 30-600 μm. The cell-structure and pore sizes of the as-prepared foam were well defined by the original CF at 1050 °C indicating the template growth formation mechanism. The cell-networks in the samples fired at 950 °C were heavily destroyed, consequently cracking and breaking features of the cell-networks along with surface peeling of the formed TiC layer were observed. This could be attributed to the mismatch in thermal expansion coefficients of carbon and TiC coexisting in the same cell structure. The destruction extent, however, decreased with increasing the temperature and became no evident in the completely reacted samples at 1050 °C. Many drawbacks suffered by most of the conventional synthesis techniques, e.g. high processing temperature, low porosity volume, difficulty in controlling the desired final pore size and structure, complicated operating process, and high production cost can be avoided by using the MSS technique developed with the present work.

Chapter Eight

General Conclusions and Suggestions for Future

8.1 General Conclusions

This study has confirmed that molten salt synthesis (MSS) is a highly effective technique in the synthesis of novel non-oxide ceramic materials at relatively low temperatures. In the case of ZrC, temperatures used to synthesise submicron and nano-sized ZrC particles could be reduced respectively to as low as 950 °C and 850 °C, which were much lower than those used by most of the conventional techniques previously reported. Furthermore, in the case of ZrB_2 synthesis, the temperature was also 100-500 °C lower than those used by previously reported techniques, in particular, by the carbothermal reduction synthesis which is currently applied for the commercial production. In addition to the reduction in the synthesis temperature, the as-prepared ZrB_2 and ZrC particles were highly pure and well-dispersed even though they were nanosized ones. This is different from that in the case of using the sol-gel technique. When the sol-gel technique is used, the final nanosized product powders often suffer from heavy

agglomeration. Besides, the salts used in the MSS process are recyclable making it a cost-effective and promising technique for industrial production. Additionally, boride and carbide materials with well controllable morphologies can be extensively synthesised via MSS method by using various types of carbon (or boron) source and metallic (or oxide) source.

Despite of the advantages of MSS stated above, when a molten salt mediated magnesiothermic reduction process was used to synthesise ZrB_2 and ZrC powders, evaporationg loss of Mg occurred and so its excessive addition was required to complete the reactions. In addition, due to use of Mg as a reducing agent, post firing acid leaching had to be carried out to remove the by-product MgO.

Furthermore, by taking advantage of template growth mechanism, sizes and shapes of the final products could be well defined by those of the less soluble reactant in the reaction system. Based on this, novel TiC nanosheets (TNS) and TiC-coated graphite nanosheets (TCNS), which were considered to be difficult to be prepared via a conventional route due to intrinsically non-layered structure of TiC, were succssesfully synthesised by using graphite nanosheets (GNS) as both carbon source and reaction templates and via their reaction with metallic Ti in KCl. This strategy could be similarly used to prepare 2D-nanostructures or graphene-like structures of other types of carbides with non-layered crystalline structures. In addition, the strategy was extendedly used to synthesise macroporous TiC foams with a well-defined microstructure by using carbon foam as a carbon source and template. The resultant TiC foams retained well interconnected 3D-cell networks of the original carbon foams, suggesting that a porous ceramic with desired pore sizes could be readily designed and prepared by using an appropriate porous template material, showing much more

flexibility and controllability than in the case of using the additive-gas forming agent technique. The resultant pores were clear of undesired impurities and/or membranes, providing an enhanced peameability for fluids or gases through the unblocked pores. Furthermore, the cell-networks were free of surface cracks and holes. Differently from this, in the case of using the conventional replica technique, surface-cracks in the cell-networks and thin membranes covering the pores were often seen in the synthesised foams, leading to lowered mechanical strength and decreased permeability of fluids and gases through the blocked pores, along with increased density of the produced material and hence a limitation in further applications of the porous product. In addition, the synthesis temperature required by the MSS technique developed with this work for preparing the TiC foams was 1050 °C, significantly lower than that (>1450 °C) used by most of the other techniques.

As described and discussed in previous chapters (Chapter 4-7), the template growth mechanism had governed the synthesis processes of the 4 types of nonoxide products. The general reaction mechanism involved in the synthesis can be summarised as follows. Reference to the SEM analysis in all studied cases, the resultant products to a large extent preserved well the original shapes and sizes of their corresponding template precursors (ZrO_2, CB, GNS, and CF). Therefore, ZrO_2 powder (CB or GNS or CF) not only acted as zirconium (or carbon) source but also functioned as a reaction template for boride (or carbide) growth in the melt. Whereas, boron (B) (zirconium (Zr) or titanium (Ti)) partially dissolved in the molten salt and diffused into the surfaces of the ZrO_2 template (CB or GNS or CF) to react and in-situ form a thin layer of the product ZrB_2 (ZrC or TiC) on the surfaces of the template. The formed product layer prevented dissolution of the core material, ZrO_2 (CB or GNS or CF) in the melt while B (Zr or Ti) dissolved continuously in the given melt. The reaction proceeded

incessantly, along with the increase in product layer and the reduction in the template material, with time until the completion of the reaction and hence the obtained product preserved well shapes and sizes of its template material.

8.2 Suggestions for future work

For future work, the following suggestions include some points among many aspects of the MSS method and characterisation of novel boride and carbide materials that are of interest.

1) Since the template growth mechanism dominates the boride formation process and ZrO_2 particles act as the reaction templates, nanosized ZrB_2 particles could be synthesised by simply using nanosized ZrO_2 particles.
2) In the case of ZrB_2, the synthesis temperature could be further reduced via further optimising the processing parameters, e.g., by increasing the dwell time (4 or 6 h).
3) Because ZrB_2 is effectively fabricated here, other transition metal diborides such as TiB_2, NbB_2 and HfB_2 should be able to be produced accordingly with a variety of particle sizes via using different transition metal sources.
4) In both cases of the ZrB_2 and ZrC synthesis, the synthesis temperature and/or holding time could be optimised by using finer ZrO_2 particles (instead of submicron size), along with well mixed batch by ball-milling prior to heat treatment.
5) In the case of ZrC synthesis, future work is still required to further clarify the relevant mechanisms, for example, using submicrosized carbon black instead to react with the nanosized ZrO_2 to investigate particle size effect of the starting carbon black and ZrO_2 on the ZrC formation and its morphology, in comparison with the results gained from chapter five.

6) Examination of mechanical, thermal, chemical and electrical properties of the resultant TNS, TCNS and TiC foams needs to be carried out.
7) The sintering behaviour of the prepared nonoxide particles should be investigated and the physicochemical properties of the resultant bulk materials should be tested.
8) Other types of carbide materials with interesting 2D-nanostructure or their foam counterparts with 3D-interconnected networks could be further fabricated using the present technique.

References

[1] A. L. Chamberlain, *et al.*, "High-strength zirconium diboride-based ceramics," *Journal of the American Ceramic Society,* vol. 87, pp. 1170-1172, 2004.

[2] W. G. Fahrenholtz, *et al.*, "Refractory diborides of zirconium and hafnium," *Journal of the American Ceramic Society,* vol. 90, pp. 1347-1364, 2007.

[3] S. K. Mishra , *et al.*, "Sintering studies on ultrafine ZrB_2 powder produced by a self-propagating high-temperature synthesis process," *Journal of Materials Research,* vol. 15, pp. 2499-2504, 2000.

[4] J. J. Melendez-Martınez, *et al.*, "Characterisation and high temperature mechanical properties of zirconium boride-based materials," *Journal of the European Ceramic Society,* vol. 22, pp. 2543-2549, 2002.

[5] F. Monteverde, *et al.*, "Processing and properties of zirconium diboride-based composites," *Journal of the European Ceramic Society,* vol. 22, pp. 279-288, 2002.

[6] J. F. Justin and A. Jankowiak, "Ultra high temperature ceramics: densification, properties and thermal stability," *Journal of Aerospacelab,* pp. 1-11, 2011.

[7] C. Yan, *et al.*, "Synthesis of zirconium carbide powders using chitosan as carbon source," *Ceramics International,* vol. 39, pp. 3409-3412, 2013.

[8] S. Wei, *et al.*, "Thermodynamic analysis and growth of zirconium carbide by chemical vapor deposition," *Physics Procedia,* vol. 46, pp. 88-101, 2013.

[9] M. M. Opeka, *et al.*, "Mechanical, thermal, and oxidation properties of refractory hafnium and zirconium compounds," *Journal of the European Ceramic Society,* vol. 19, pp. 2405-2414, 1999.

[10] K. Minato, *et al.*, "Fission product release from ZrC-coated fuel particles during postirradiation heating at 1600 °C," *Journal of Nuclear Materials,* vol. 224, pp. 85-92, 1995.

[11] G. H. Reynolds, *et al.*, "Irradiation behavior of experimental fuel particles containing chemically vapor deposited zirconium carbide coatings," *Journal of Nuclear Materials,* vol. 62, pp. 9-16, 1976.

[12] D. Strzęciwilk, *et al.*, "Microstructure of TiC crystals obtained from high temperature nickel solution," *Journal of Alloys and Compounds,* vol. 350, pp. 256-263, 2003.

[13] M. S. Song, *et al.*, "Study of formation behavior of TiC ceramic obtained by self-propagating high-temperature synthesis from Al–Ti–C elemental powders," *International Journal of Refractory Metals and Hard Materials,* vol. 27, pp. 584-589, 2009.

[14] A. K. Khanra, *et al.*, "Double SHS of ZrB_2 powder," *Journal of Materials Processing Technology,* vol. 202, pp. 386-390, 2008.

[15] X. Su, *et al.*, "A simple method for preparing graphene nano-sheets at low temperature," *Advanced Powder Technology,* vol. 24, pp. 317-323, 2013.

[16] M. J. Allen, *et al.*, "Honeycomb carbon: A review of graphene," *Chemical Reviews,* vol. 110, pp. 132-145, 2010.

[17] W. Du, *et al.*, "From graphite to graphene: direct liquid-phase exfoliation of graphite to produce single- and few-layered pristine graphene," *Journal of Materials Chemistry A,* vol. 1, pp. 10592-10606, 2013.

[18] M. R. Nangrejo, *et al.*, "Preparation of silicon carbide–silicon nitride composite foams from pre-ceramic polymers," *Journal of the European Ceramic Society,* vol. 20, pp. 1777-1785, 2000.

[19] M. R. Nangrejo, *et al.*, "The structure of ceramic foams produced using polymeric precursors," *Journal of Materials Science Letters,* vol. 19, pp. 787-789, 2000.

[20] U. T. Gonzenbach, *et al.*, "Macroporous ceramics from particle-stabilized wet foams," *Journal of the American Ceramic Society,* vol. 90, pp. 16-22, 2007.

[21] Y. Katoh, *et al.*, "Properties of zirconium carbide for nuclear fuel applications," *Journal of Nuclear Materials,* vol. 441, pp. 718-742, 2013.

[22] K. Minato, *et al.*, "Deterioration of ZrC-coated fuel particle caused by failure of pyrolytic carbon layer," *Journal of Nuclear Materials,* vol. 252, pp. 13-21, 1998.

[23] Q. Tong, *et al.*, "Resistance to ablation of pitch-derived ZrC/C composites," *Carbon,* vol. 42, pp. 2495-2500, 2004.

[24] A. Arya and E. A. Carter, "Structure, bonding, and adhesion at the ZrC(100)/Fe(110) interface from first principles," *Surface Science,* vol. 560, pp. 103-120, 2004.

[25] J. Nie, *et al.*, "Influence of trace boron on the morphology of titanium carbide in an Al–Ti–C–B master alloy," *Journal of Alloys and Compounds,* vol. 491, pp. 113-117, 2010.

[26] R. Koc, "Kinetics and phase evolution during carbothermal synthesis of titanium carbide from ultrafine titania/carbon mixture," *Journal of Materials Science,* vol. 33, pp. 1049-1055, 1998.

[27] S. Iijima, "Helical microtubules of graphitic carbon," *Nature* vol. 354, pp. 56-58, 1991.

[28] X. Yuan, *et al.*, "Preparation of titanium carbide nanowires for application in electromagnetic wave absorption," *Journal of Alloys and Compounds,* vol. 596, pp. 132-139, 2014.

[29] Y. Qin and M. Hu, "Characterization and field emission characteristics of carbon nanotubes modified by titanium carbide," *Applied Surface Science,* vol. 254, pp. 3313-3317, 2008.

[30] X. Yuan, *et al.*, "Synthesis of TiC nanowires on porous $ZrSiO_4$ substrate and their field emission properties," *Vacuum,* vol. 99, pp. 294-297, 2014.

[31] M. Futamoto, *et al.*, "Study on titanium carbide field emitters by field-ion microscopy, field-electron emission microscopy, Auger electron spectroscopy, and atom-probe field-ion microscopy," *Surface Science,* vol. 120, pp. 90-102, 1982.

[32] Y.-K. Kim, *et al.*, "Electron-emission properties of titanium carbide-coated carbon nanotubes grown on a nano-sized tungsten tip," *Thin Solid Films,* vol. 517, pp. 1156-1160, 2008.

[33] Y. Yao, *et al.*, "Highly conductive, mechanically robust, and electrochemically inactive TiC/C nanofiber scaffold for high-performance silicon anode batteries," *ACS nano,* vol. 5, pp. 8346-8351, 2011.

[34] P. Kannan, *et al.*, "Nitrogen doped graphene nanosheet supported platinum nanoparticles as high performance electrochemical homocysteine biosensors," *Journal of Materials Chemistry B,* vol. 1, pp. 4655-4666, 2013.

[35] P. Tang, *et al.*, "Graphene-like molybdenum disulfide and its application in optoelectronic devices," *Wuli Huaxue Xuebao/ Acta Physico - Chimica Sinica,* vol. 29, pp. 667-677, 2013.

[36] Q. Peng and S. De, "Outstanding mechanical properties of monolayer MoS2 and its application in elastic energy storage," *Physical Chemistry Chemical Physics,* vol. 15, pp. 19427-19437, 2013.

[37] Y. Liu, *et al.*, "Sandwich-structured graphene-like MoS_2/C microspheres for rechargeable Mg batteries," *Journal of Materials Chemistry A,* vol. 1, pp. 5822-5826, 2013.

[38] A. H. M. A. Wasey, *et al.*, "H -BN monolayer on the Ni(111) surface: A potential catalyst for oxidation," *ACS Applied Materials and Interfaces,* vol. 5, pp. 10404-10408, 2013.

[39] F. Müller and S. Grandthyll, "Monolayer formation of hexagonal boron nitride on Ag(001)," *Surface Science,* vol. 617, pp. 207-210, 2013.

[40] S. Ji, *et al.*, "Exfoliated MoS_2 nanosheets as efficient catalysts for electrochemical hydrogen evolution," *Electrochimica Acta,* vol. 109, pp. 269-275, 2013.

[41] Z. Wu, *et al.*, "Novel hexagonal MoS_2 nanoplates formed by solid-state assembly of nanosheets," *Journal of Crystal Growth,* vol. 312, pp. 1973-1976, 2010.

[42] S. R. Qi, *et al.*, "Synthesis of titanium carbide nanowires," *Journal of Crystal Growth,* vol. 219, pp. 485-488, 2000.

[43] I. R. Shein and A. L. Ivanovskii, "Graphene-like nanocarbides and nanonitrides of d metals (MXenes): synthesis, properties and simulation," *Micro & Nano Letters, IET,* vol. 8, pp. 59-62, 2013.

[44] Z. M. Sun, "Progress in research and development on MAX phases: A family of layered ternary compounds," *International Materials Reviews,* vol. 56, pp. 143-166, 2011.

[45] M. Naguib, *et al.*, "Two-dimensional nanocrystals produced by exfoliation of Ti_3AlC_2," *Advanced Materials,* vol. 23, pp. 4248-4253, 2011.

[46] Z. Zhang, *et al.*, "Two-dimensional tetragonal TiC monolayer sheet and nanoribbons," *Journal of the American Chemical Society,* vol. 134, pp. 19326-19329, 2012.

[47] P. Song, *et al.*, "Irradiation resistance properties studies on helium ions irradiated MAX phase Ti_3AlC_2," *Nuclear Instruments and Methods in Physics Research Section B: Beam Interactions with Materials and Atoms*.

[48] A. Abdulkadhim, *et al.*, "MAX phase formation by intercalation upon annealing of TiCx/Al ($0.4 \leq x \leq 1$) bilayer thin films," *Acta Materialia,* vol. 59, pp. 6168-6175, 2011.

[49] M. A. El Saeed, *et al.*, "Optimization of the Ti_3SiC_2 MAX phase synthesis," *International Journal of Refractory Metals and Hard Materials,* vol. 35, pp. 127-131, 2012.

[50] J. Etzkorn, *et al.*, "Ti_2GaC, Ti_4GaC_3 and Cr_2GaC—Synthesis, crystal growth and structure analysis of Ga-containing MAX-phases $M_{n+1}GaC_n$ with M=Ti, Cr and n=1, 3," *Journal of Solid State Chemistry,* vol. 182, pp. 995-1002, 2009.

[51] M. Naguib, *et al.*, "Two-dimensional transition metal carbides," *ACS nano,* vol. 6, pp. 1322-1331, 2012.

[52] I. R. Shein and A. L. Ivanovskii, "Graphene-like titanium carbides and nitrides $Ti_{n+1}C_n$, $Ti_{n+1}N_n$ (n=1, 2, and 3) from de-intercalated MAX phases: First-principles probing of their structural, electronic properties and relative stability," *Computational Materials Science,* vol. 65, pp. 104-114, 2012.

[53] B. Yang, *et al.*, "Synthesis of hexagonal-prism-like ZrB_2 by a sol–gel route," *Powder Technology, 2014*.

[54] C. Subramanian, *et al.*, "Synthesis and consolidation of titanium diboride," *International Journal of Refractory Metals and Hard Materials,* vol. 25, pp. 345-350, 2007.

[55] A. K. Khanra, *et al.*, "Performance of ZrB_2–Cu composite as an EDM electrode," *Journal of Materials Processing Technology,* vol. 183, pp. 122-126, 2007.

[56] H. M. Zaw, *et al.*, "Formation of a new EDM electrode material using sintering techniques," *Journal of Materials Processing Technology,* vol. 89–90, pp. 182-186, 1999.

[57] A. L. Chamberlain, *et al.*, "Pressureless sintering of zirconium diboride," *Journal of the American Ceramic Society,* vol. 89, pp. 450-456, 2006.

[58] W.-W. Wu, *et al.*, "Microstructure and mechanical properties of ZrB_2–SiC–BN composites fabricated by reactive hot pressing and reactive spark plasma sintering," *Scripta Materialia,* vol. 68, pp. 889-892, 2013.

[59] X. Zhang, *et al.*, "Modification and validation of the thermal shock parameter for ceramic matrix composites under water quenching condition," *Materials & Design,* vol. 30, pp. 4552-4556, 2009.

[60] L. S. Sigl, *et al.*, "On the toughness of brittle materials reinforced with a ductile phase," *Acta Metallurgica,* vol. 36, pp. 945-953, 1988.

[61] X. Sun, *et al.*, "ZrB_2-ceramic toughened by refractory metal Nb prepared by hot-pressing," *Materials & Design,* vol. 31, pp. 4427-4431, 2010.

[62] H.-Y. Qiu, *et al.*, "ZrB_2 powders prepared by boro/carbothermal reduction of ZrO2: The effects of carbon source and reaction atmosphere," *Powder Technology,* vol. 217, pp. 462-466, 2012.

[63] M. Thompson, *et al.*, "Effect of starting particle size and oxygen content on densification of ZrB_2," *Journal of the American Ceramic Society,* vol. 94, pp. 429-435, 2011.

[64] A. A. Mahday, *et al.*, "Mechanically induced solid state carburization for fabrication of nanocrystalline ZrC refractory material powders," *Journal of Alloys and Compounds,* vol. 299, pp. 244-253, 2000.

[65] Ö. Balcı, *et al.*, "Carbothermal production of ZrB_2–ZrO_2 ceramic powders from ZrO_2–B_2O_3/B system by high-energy ball milling and annealing assisted process," *Ceramics International,* vol. 38, pp. 2201-2207, 2012.

[66] R. Koc and J. S. Folmer, "Carbothermal synthesis of titanium carbide using ultrafine titania powders," *Journal of Materials Science,* vol. 32, pp. 3101-3111, 1997.

[67] A. Maitre and P. Lefort, "Solid state reaction of zirconia with carbon," *Solid State Ionics,* vol. 104, pp. 109-122, 1997.

[68] L. B. Nezhevenko, *et al.*, "Sintering of zirconium and niobium carbides with carbon additions," *Soviet Powder Metallurgy and Metal Ceramics,* vol. 19, pp. 535-539, 1980.

[69] A. K. Khanra, *et al.*, "Carbothermal synthesis of zirconium diboride (ZrB_2) whiskers," *Advances in Applied Ceramics,* vol. 106, pp. 155-160, 2007.

[70] E.-Y. Jung, *et al.*, "Synthesis of ZrB_2 powders by carbothermal and borothermal reduction," *Journal of Alloys and Compounds,* vol. 538, pp. 164-168, 2012.

[71] W. Sen, *et al.*, "Preparation of TiC powders by carbothermal reduction method in vacuum," *Transactions of Nonferrous Metals Society of China,* vol. 21, pp. 185-190, 2011.

[72] M. Ali and P. Basu, "Mechanochemical synthesis of nano-structured TiC from TiO_2 powders," *Journal of Alloys and Compounds,* vol. 500, pp. 220-223, 2010.

[73] S. K. Mishra, *et al.*, "Defect structures in zirconium diboride powder prepared by self-propagating high-temperature synthesis," *Materials Science and Engineering: A,* vol. 364, pp. 249-255, 2004.

[74] H. E. Çamurlu and F. Maglia, "Preparation of nano-size ZrB_2 powder by self-propagating high-temperature synthesis," *Journal of the European Ceramic Society,* vol. 29, pp. 1501-1506, 2009.

[75] A. K. Khanra, *et al.*, "Self-propagating-high-temperature synthesis (SHS) of ultrafine ZrB_2 powder," *Journal of Materials Science Letters,* vol. 22, pp. 1189-1191, 2003.

[76] M. X. Zhang, *et al.*, "Fabrication of ZrC particles and its formation mechanism by self-propagating high-temperature synthesis from Fe–Zr–C elemental powders," *Journal of Alloys and Compounds,* vol. 509, pp. 8120-8125, 2011.

[77] M. Song, *et al.*, "Reaction synthesis of nano-scale ZrC particulates by self-propagating high-temperature synthesis from Al–Zr–C powder mixtures," *ISIJ International,* vol. 48, pp. 1026–1029, 2008.

[78] H. H. Nersisyan, *et al.*, "Self-propagating high-temperature synthesis of nano-sized titanium carbide powder," *J. Mater. Res.*, vol. 17, pp. 2859-2864, 2002.

[79] S. Jin, *et al.*, "Self-propagating high-temperature synthesis of nano-TiCx particles with different shapes by using carbon nano-tube as C source," *Nanoscale Research Letters,* vol. 6, pp. 1-7, 2011.

[80] B. Akgün, *et al.*, "Mechanochemical and volume combustion synthesis of ZrB_2," *International Journal of Refractory Metals and Hard Materials,* vol. 29, pp. 601-607, 2011.

[81] M. B. Rahaei, *et al.*, "Mechanochemical synthesis of nano TiC powder by mechanical milling of titanium and graphite powders," *Powder Technology,* vol. 217, pp. 369-376, 2012.

[82] D.-W. Lee, *et al.*, "Synthesis of ultrafine ZrC powders by novel reduction process," *Materials Transactions,* vol. 51, pp. 2266-2268, 2010.

[83] V. Sundaram, *et al.*, "Reaction path in the magnesium thermite reaction to synthesise titanium diboride," *Journal of Materials Research,* vol. 12, pp. 2657-2664, 1997.

[84] E. Bilgi, *et al.*, "Formation of TiB_2 by volume combustion and mechanochemical process," *Materials Research Bulletin,* vol. 43, pp. 873-881, 2008.

[85] N. Setoudeh and N. J. Welham, "Formation of zirconium diboride (ZrB_2) by room temperature mechanochemical reaction between ZrO_2, B_2O_3 and Mg," *Journal of Alloys and Compounds,* vol. 420, pp. 225-228, 2006.

[86] A. K. Khanra, "Reaction chemistry during self-propagating high-temperature synthesis (SHS) of H_3BO_3–ZrO_2–Mg system," *Materials Research Bulletin,* vol. 42, pp. 2224-2229, 2007.

[87] H. Kobayashi, *et al.*, "Low-temperature synthesis of ZrC powder by cyclic reaction of Mg in ZrO_2–Mg–CH_4," *Journal of the American Ceramic Society,* vol. 76, pp. 2389-2392, 1993.

[88] H. Preiss, *et al.*, "Studies on the carbothermal preparation of titanium carbide from different gel precursors," *Journal of the European Ceramic Society,* vol. 19, pp. 195-206, 1999.

[89] H. Wu, *et al.*, "Pyrolysis synthesis and microstructure of zirconium carbide from new preceramic polymers," *Ceramics International,* vol. 40, pp. 5967-5972, 2014.

[90] Y. Zhang, *et al.*, "Morphology evolution of ZrB_2 nanoparticles synthesized by sol–gel method," *Journal of Solid State Chemistry,* vol. 184, pp. 2047-2052, 2011.

[91] Y. Yan, *et al.*, "Carbothermal synthesis of ultra-fine zirconium carbide powders using inorganic precursors via sol–gel method," *Journal of Sol-Gel Science and Technology,* vol. 44, pp. 81-85, 2007.

[92] R. Li, *et al.*, "Synthesis of ZrB_2 nanoparticles by sol-gel method," *Journal of Sol-Gel Science and Technology,* vol. 58, pp. 580-585, 2011.

[93] H. Wang, *et al.*, "Synthesis and characterization of a novel precursor-derived ZrC/ZrB_2 ultra-high-temperature ceramic composite," *Applied Organometallic Chemistry,* vol. 27, pp. 79-84, 2013.

[94] C. Xie, *et al.*, "Synthesis and microstructure of zirconium diboride formed from polymeric precursor pyrolysis," *Journal of the American Ceramic Society,* vol. 95, pp. 866-869, 2012.

[95] G.Y. Ji, *et al.*, "Effects of sol network modifiers on preparation, morphology and phase composition of zirconium diboride nano-powders by novel sol-gel technology," *Key Eng. Matter.,* vol. 544, pp. 139-143, 2013.

[96] H. Ji, *et al.*, "Low-temperature synthesis of ZrB_2 nano-powders using a sorbitol modified sol–gel processing route," *Advanced Powder Technology,* 2014.

[97] C. Yan, *et al.*, "Carbothermal synthesis of submicrometer zirconium carbide from polyzirconoxane and phenolic resin by the facile one-pot reaction," *Journal of the American Ceramic Society,* vol. 95, pp. 3366-3369, 2012.

[98] C. Ang, *et al.*, "Synthesis and evolution of zirconium carbide via sol–gel route: features of nanoparticle oxide–carbon reactions," *Journal of the American Ceramic Society,* vol. 96, pp. 1099-1106, 2013.

[99] M. Dollé, *et al.*, "Synthesis of nanosized zirconium carbide by a sol–gel route," *Journal of the European Ceramic Society,* vol. 27, pp. 2061-2067, 2007.

[100] V. G. Sevastyanov, *et al.*, "Low-temperature synthesis of nanodispersed titanium, zirconium, and hafnium carbides," *Russian Journal of Inorganic Chemistry,* vol. 56, pp. 661-672, 2011.

[101] N. Chandra, *et al.*, "Synthesis of nano-TiC powder using titanium gel precursor and carbon particles," *Materials Letters,* vol. 63, pp. 1051-1053, 2009.

[102] J. Zhong, *et al.*, "Formation of novel mesoporous TiC microspheres through a sol–gel and carbothermal reduction process," *Journal of the European Ceramic Society,* vol. 32, pp. 3407-3414, 2012.

[103] V. Medri, *et al.*, "Comparison of ZrB2-ZrC-SiC Composites Fabricated by Spark Plasma Sintering and Hot-Pressing," *Advanced Engineering Materials,* vol. 7, pp. 159-163, 2005.

[104] T. Ogawa, *et al.*, "Chemical vapor deposition of ZrC within a spouted bed by bromide process," *Journal of Nuclear Materials,* vol. 97, pp. 104-112, 1981.

[105] Y. Wang, *et al.*, "Deposition mechanism for chemical vapor deposition of zirconium carbide coatings," *Journal of the American Ceramic Society,* vol. 91, pp. 1249-1252, 2008.

[106] K. Ikawa, "Vapor deposition of zirconium carbide-carbon composites by the chloride process," *Journal of the Less Common Metals,* vol. 29, pp. 233-239, 1972.

[107] T. Ogawa, *et al.*, "Effect of gas composition on the deposition of ZrC-C mixtures: the bromide process," *Journal of Materials Science,* vol. 14, pp. 125-132, 1979.

[108] V. G. Samoilenko and L. N. Pereselentseva, "Deposition of zirconium carbide coatings acting as diffusion barriers in composites consisting of a metallic matrix and refractory metal fibers," *Soviet Powder Metallurgy and Metal Ceramics,* vol. 14, pp. 725-728, 1975.

[109] Y.-G. Jung, *et al.*, "Effect of CH_4 and H_2 on CVD of SiC and TiC for possible fabrication of SiC/TiC/C FGM," *Materials Letters,* vol. 30, pp. 339-345, 1997.

[110] Y. Zhu, *et al.*, "Deposition of TiC film on titanium for abrasion resistant implant material by ion-enhanced triode plasma CVD," *Applied Surface Science,* vol. 262, pp. 156-158, 2012.

[111] E. Randich and D. D. Allred, "Chemically vapor-deposited ZrB_2 as a selective solar absorber," *Thin Solid Films,* vol. 83, pp. 393-398, 1981.

[112] S. Motojima, *et al.*, "ZrB_2 coated on copper plate by chemical vapour deposition, and its corrosion and oxidation stabilities," *Thin Solid Films,* vol. 189, pp. 73-79, 1990.

[113] J. F. Pierson, *et al.*, "Low temperature ZrB_2 remote plasma enhanced chemical vapor deposition," *Thin Solid Films,* vol. 359, pp. 68-76, 2000.

[114] F. Carn, *et al.*, "Rational design of macrocellular silica scaffolds obtained by a tunable sol–gel foaming process," *Advanced Materials,* vol. 16, pp. 140-144, 2004.

[115] D.-M. Liu, "Preparation and characterisation of porous hydroxyapatite bioceramic via a slip-casting route," *Ceramics International,* vol. 24, pp. 441-446, 1998.

[116] S. Kato*, et al.*, "Photocatalytic degradation of gaseous sulfur compounds by silver-deposited titanium dioxide," *Applied Catalysis B: Environmental,* vol. 57, pp. 109-115, 2005.

[117] J.-H. Eom*, et al.*, "Processing and properties of macroporous silicon carbide ceramics: A review," *Journal of Asian Ceramic Societies,* vol. 1, pp. 220-242, 2013.

[118] W.E. Lee and W. M. Rainforth, *Ceramic Microstructures: Property Control by Processing* 1994.

[119] K. Ishizaki, *et al.*, *Porous Materials: Process Technology and Applications*. London: Kluwer Academic Publishers, 1998.

[120] R. Mouazer*, et al.*, "Silicon carbide foams by polyurethane replica technique," *Advanced Engineering Materials,* vol. 7, pp. 1124-1128, 2005.

[121] A. Zampieri*, et al.*, "Zeolite coatings on microcellular ceramic foams: a novel route to microreactor and microseparator devices," *Advanced Materials,* vol. 16, pp. 819-823, 2004.

[122] A. R. Studart*, et al.*, "Processing routes to macroporous ceramics: a review," *Journal of the American Ceramic Society,* vol. 89, pp. 1771-1789, 2006.

[123] H. Peng*, et al.*, "The use of backflushed coalescing microfiltration as a pretreatment for the ultrafiltration of bilge water," *Desalination,* vol. 181, pp. 109-120, 2005.

[124] K. A. Hing, "Bioceramic bone graft substitutes: influence of porosity and chemistry," *International Journal of Applied Ceramic Technology,* vol. 2, pp. 184-199, 2005.

[125] J.-H. Eom, *et al.*, "Processing and properties of polysiloxane-derived porous silicon carbide ceramics using hollow microspheres as templates," *Journal of the European Ceramic Society,* vol. 28, pp. 1029-1035, 2008.

[126] J. H. Eom and Y. W. Kim, "Effect of template size on microstructure and strength of porous silicon carbide ceramics," *Nippon Seramikkusu Kyokai Gakujutsu Ronbunshi/Journal of the Ceramic Society of Japan,* vol. 116, pp. 1159-1163, 2008.

[127] K. E. Pappacena, *et al.*, "Thermal conductivity of porous silicon carbide derived from wood precursors," *Journal of the American Ceramic Society,* vol. 90, pp. 2855-2862, 2007.

[128] J. H. Eom, *et al.*, "Effects of the initial α-SiC content on the microstructure, mechanical properties, and permeability of macroporous silicon carbide ceramics," *Journal of the European Ceramic Society,* vol. 32, pp. 1283-1290, 2012.

[129] Y. Gao, *et al.*, "Novel TiC/Ti open cellular foams prepared by a modified sponge-coating method using high frequency induction heating Process," *Journal of Materials Science and Technology,* vol. 29, pp. 339-343, 2013.

[130] M. R. Nangrejo, *et al.*, "Silicon carbide-titanium carbide composite foams produced using a polymeric precursor," *International Journal of Inorganic Materials,* vol. 3, pp. 37-45, 2001.

[131] B. Matovic, *et al.*, "Preparation of porous silica ceramics using the wood template," *Materials and Manufacturing Processes,* vol. 24, pp. 1109-1113, 2009.

[132] N. Popovska, *et al.*, "Kinetic analysis of the processing of porous biomorphic titanium carbide ceramics by chemical vapor infiltration," *Chemical Vapor Deposition,* vol. 11, pp. 153-158, 2005.

[133] B. Sun, *et al.*, "Porous TiC ceramics derived from wood template," *Journal of Porous Materials,* vol. 9, pp. 275-277, 2002.

[134] N. Popovska, *et al.*, "Processing of porous biomorphic TiC ceramics by chemical vapor infiltration and reaction (Cvi-R) technique," in *28th International Conference on Advanced Ceramics and Composites A: Ceramic Engineering and Science Proceedings*, ed: John Wiley & Sons, Inc., 2008, pp. 535-540.

[135] B. Sun, *et al.*, "Production of morph-genetic TiC/C ceramic," *Materials Letters,* vol. 58, pp. 798-801, 2004.

[136] A. Díaz and S. Hampshire, "Characterisation of porous silicon nitride materials produced with starch," *Journal of the European Ceramic Society,* vol. 24, pp. 413-419, 2004.

[137] J.-F. Yang, *et al.*, "Fabrication and characterisation of porous silicon nitride ceramics using Yb_2O_3 as sintering additive," *Journal of the European Ceramic Society,* vol. 23, pp. 371-378, 2003.

[138] R. M. Khattab, *et al.*, "Preparation and characterization of porous alumina ceramics through starch consolidation casting technique," *Ceramics International,* vol. 38, pp. 4723-4728, 2012.

[139] E. Gregorová and W. Pabst, "Process control and optimized preparation of porous alumina ceramics by starch consolidation casting," *Journal of the European Ceramic Society,* vol. 31, pp. 2073-2081, 2011.

[140] A. C. Pierre, "Porous sol-gel ceramics," *Ceramics International,* vol. 23, pp. 229-238, 1997.

[141] H. R. Ramay and M. Zhang, "Preparation of porous hydroxyapatite scaffolds by combination of the gel-casting and polymer sponge methods," *Biomaterials,* vol. 24, pp. 3293-3302, 2003.

[142] T. Fujiu, *et al.*, "Processing and properties of cellular silica synthesized by foaming sol-gels," *Journal of the American Ceramic Society,* vol. 73, pp. 85-90, 1990.

[143] L. Shi, *et al.*, "Porous titanium carbide ceramics fabricated by coat-mix process," *Scripta Materialia,* vol. 55, pp. 763-765, 2006.

[144] P. Sepulveda, "Gelcasting foams for porous ceramics," *Am. Ceram. Soc. Bull.,* vol. 76 pp. 61-65, 1993.

[145] M. D. M. Innocentini, *et al.*, "Permeability and structure of cellular ceramics: a comparison between two preparation techniques," *Journal of the American Ceramic Society,* vol. 81, pp. 3349-3352, 1998.

[146] P. Colombo and J. Hellmann, "Ceramic foams from preceramic polymers," *Materials Research Innovations,* vol. 6, pp. 260-272, 2002.

[147] P. Sepulveda and J. G. P. Binner, "Processing of cellular ceramics by foaming and in situ polymerisation of organic monomers," *Journal of the European Ceramic Society,* vol. 19, pp. 2059-2066, 1999.

[148] D. G. Lovering and R. J. Gale, *Molten Salt Techniques* vol. 1. New York and London: Plenum Press, 1983.

[149] R. Yang, *et al.*, "Molten salt synthesis of Mo_2C powder using a mechanically milled powder," *Materials Letters,* vol. 61, pp. 4815-4817, 2007.

[150] X. Jiang, *et al.*, "Synthesis of $ZnWO_4$ nano-particles by a molten salt method," *Materials Letters,* vol. 61, pp. 4595-4598, 2007.

[151] S. Zhang, *et al.*, "Molten salt synthesis of magnesium aluminate ($MgAl_2O_4$) spinel powder," *Journal of the American Ceramic Society,* vol. 89, pp. 1724-1726, 2006.

[152] A. Aboujalil, *et al.*, "Molten salt synthesis of the lead titanate $PbTiO_3$, investigation of the reactivity of various titanium and lead salts with molten alkali-metal nitrites," *Journal of Materials Chemistry,* vol. 8, pp. 1601-1606, 1998.

[153] Z. Li, *et al.*, "Molten salt synthesis of zinc aluminate powder," *Journal of the European Ceramic Society,* vol. 27, pp. 3407-3412, 2007.

[154] M. Wakao, *et al.*, "Viscosity measurements of molten LiCl in the temperature range 886–1275 K," *International Journal of Thermophysics,* vol. 12, pp. 223-230, 1991.

[155] T. Ito, *et al.*, "Redetermination of the viscosity of molten NaCl at elevated temperatures," *International Journal of Thermophysics,* vol. 10, pp. 819-831, 1989.

[156] Z. Li, *et al.*, "Low-temperature synthesis of $CaZrO_3$ powder from molten salts," *Journal of the American Ceramic Society,* vol. 90, pp. 364-368, 2007.

[157] T. Kimura, *Molten Salt Synthesis of Ceramic Powders*, 2011.

[158] Z. Li, *et al.*, "Molten salt synthesis of $LaAlO_3$ powder at low temperatures," *Journal of the European Ceramic Society,* vol. 27, pp. 3201-3205, 2007.

[159] D. D. Jayaseelan, *et al.*, "Template formation of magnesium aluminate ($MgAl_2O_4$) spinel microplatelets in molten salt," *Journal of the European Ceramic Society,* vol. 27, pp. 4745-4749, 2007.

[160] X. Li, *et al.*, "A convenient, general synthesis of carbide nanofibres via templated reactions on carbon nanotubes in molten salt media," *Carbon,* vol. 47, pp. 201-208, 2009.

[161] A. W. Hull, "A new method of chemical analysis," *Journal of the American Chemical Society,* vol. 41, pp. 1168-1175, 1919.

[162] A. Clearfield, et al., Ed., *Principls and Applications of Powder Diffraction*. United Kingdom: A John Wiley and Sons, Ltd., 2008,.

[163] L. Chen, *et al.*, "Synthesis of zirconium carbide (ZrC) nanoparticles covered with graphitic "windows" by pulsed plasma in liquid," *RSC Advances,* vol. 1, pp. 1083-1088, 2011.

[164] Wikipedia, "Scanning process and image formation," in *Scanning electron microscope*, ed: http://en.wikipedia.org/wiki/scanning_electron_microscope, 2015.

[165] J. H. Wittke. (2008, 3-Apr-2014). *Types of Signals*. Available: www4.nau.edu/microanalysis/Microprobe-SEM/Signals.html

[166] X. Liu and S. Zhang, "Low-temperature preparation of titanium carbide coatings on graphite flakes from molten salts," *Journal of the American Ceramic Society,* vol. 91, pp. 667-670, 2008.

[167] D. Chescoe and P. J. Goodhew, *The Operation of Transmission and Scanning Electron Microscopes* vol. 20. New York: Oxford Science Publications, 1990.

[168] C. Colliex, "Seeing and measuring with electrons: Transmission electron microscopy today and tomorrow – An introduction," *Comptes Rendus Physique,* vol. 15, pp. 101-109, 2014.

[169] D. B. Williams and C. B. Carter, *Transmission Electron Microscopy: A Textbook for Materials Science*: Springer, 2009.

[170] H. J. Hwang, *et al.*, "Synthesis of β-silicon carbide nanofiber from an exfoliated graphite and amorphous silica," *Materials Chemistry and Physics,* vol. 134, pp. 13-15, 2012.

[171] J. Ye, *et al.*, "Molten salt synthesis and characterization of SiC coated carbon black particles for refractory castable applications," *Journal of the European Ceramic Society,* vol. 33, pp. 2023-2029, 2013.

[172] X. Liu, *et al.*, "Magnesium coated bioresorbable phosphate glass fibres: investigation of the interface between fibre and polyester matrices," *BioMed Research International,* p. 10, 2013.

[173] W.H. Weber and R. Merlin, "Raman scattering in materials sciences," ed Berlin: Springer, 2010.

[174] J. N. Anker, *et al.*, "Biosensing with plasmonic nanosensors," *Nat Mater,* vol. 7, pp. 442-453, 2008.

[175] C.V. Raman and K. S. Krishnan., "A new radiation," *Indian Journal Physics,* vol. 2, pp. 287-298, 1928.

[176] L. A. Lyon, *et al.*, "Raman Spectroscopy," *Analytical Chemistry,* vol. 70, pp. 341-362, 1998.

[177] A. C. Ferrari, *et al.*, "Raman spectrum of graphene and graphene layers," *Physical Review Letters,* vol. 97, p. 187401, 2006.

[178] M. E. Brown, Ed., *Handbook of Thermal Analysis and Calorimetry Principles and Practice* New York: Elsevier Science B.V., 1998.

[179] P. Gabbotte, Ed., *Principles and Application of Thermal Analysis*. Blackwell publishing Ltd., 2007.

[180] M. Brochu, *et al.*, "Pressureless reactive sintering of ZrB2 ceramic," *Journal of the European Ceramic Society,* vol. 29, pp. 1493-1499, 2009.

[181] A. I. Karasev, "Preparation of technical zirconium diboride by the carbothermic reduction of mixtures of zirconium and boron oxides," *Soviet Powder Metallurgy and Metal Ceramics,* vol. 12, pp. 926-929, 1973.

[182] W. M. Guo and G. J. Zhang, "Reaction processes and characterization of ZrB2 powder prepared by boro/carbothermal reduction of ZrO_2 in vacuum," *Journal of the American Ceramic Society,* vol. 92, pp. 264-267, 2009.

[183] G. Sun, *et al.*, "Synthesis of ultra-fine ZrB_2 powder by borothermal reaction under high heating rate," vol. 66, ed, 2009, pp. 77-80.

[184] S. Ran, *et al.*, "ZrB_2 powders synthesis by borothermal reduction," *Journal of the American Ceramic Society,* vol. 93, pp. 1586-1590, 2010.

[185] K. Nishiyama, *et al.*, "Preparation of ultrafine boride powders by metallothermic reduction method," *Journal of Physics: Conference Series,* vol. 176, 2009.

[186] S. K. Mishra, *et al.*, "Microstructure evolution during sintering of self-propagating high-temperature synthesis produced ZrB2 powder," *Journal of Materials Research,* vol. 17, pp. 2809-2814, 2002.

[187] Y. T. Zheng, *et al.*, "Reaction mechanism of self-propagating magnesiothermic reduction of ZrB_2 powders," *Rare Metals,* vol. 32, pp. 408-413, 2013.

[188] S. V. Devyatkin, "Electrosynthesis of zirconium boride from cryolite-alumina melts containing zirconium and boron oxides," *Russian Journal of Electrochemistry,* vol. 37, pp. 1308-1311, 2001.

[189] H. Zhang and F. Li, "Preparation and microstructure evolution of diboride ultrafine powder by sol-gel and microwave carbothermal reduction method," *Journal of Sol-Gel Science and Technology,* vol. 45, pp. 205-211, 2008.

[190] L. Chen, *et al.*, "Preparation and some properties of nanocrystalline ZrB_2 powders," *Scripta Materialia,* vol. 50, pp. 959-961, 2004.

[191] G. Jiang, *et al.*, "Fabrication of B_4C from $Na_2B_4O_7$ + Mg + C by SHS method," *Ceramics International,* vol. 37, pp. 1689-1691, 2011.

[192] R. H. Lamoreaux, *et al.*, "High temperature evaporation of oxide II: Oxides of Be, Mg, Ca, Sr, Ba, B, Al, Ga, In, Tl, Si, Ge, Sn, Pb, Zn, Cd, and Hg "," *Phys.Chem.,* vol. 16, pp. 419-433, 1987.

[193] P. Peshev and G. Bliznakov, "On the borothermic preparation of titanium, zirconium and hafnium diborides," *Journal of the Less Common Metals,* vol. 14, pp. 23-32, 1968.

[194] R. Li, *et al.*, "Nanocarbon-dependent synthesis of ZrB_2 in a binary ZrO_2 and boron system," *Journal of Alloys and Compounds,* vol. 509, pp. 8581-8583, 2011.

[195] A. L. Ortiz, *et al.*, "A study of the oxidation of ZrB_2 powders during high-energy ball-milling in air," *Ceramics International,* vol. 38, pp. 2857-2863, 2012.

[196] H. Yuan, *et al.*, "In situ synthesis and sintering of ZrB_2 porous ceramics by the spark plasma sintering–reactive synthesis (SPS–RS) method,"

International Journal of Refractory Metals and Hard Materials, vol. 34, pp. 3-7, 2012.

[197] J. W. Gao*, et al.*, "Effects of $Na_2B_4O_7$ on the elimination of iron from aluminum melt," *Scripta Materialia,* vol. 57, pp. 197-200, 2007.

[198] S. Guo*, et al.*, "Synthesis of zirconium diboride platelets from mechanically activated $ZrCl_4$ and B powder mixture," *Ceramics International,* vol. 38, pp. 5195-5200, 2012.

[199] J. D. V. Norman and J. J. Egan, "The magnesium-magnesium chlorie system. A chronopotentiometric study1", *The Journal of Physical Chemistry,* vol. 67, pp. 2460-2462, 1963.

[200] R. S. Sethi, "Electrocoating from molten salts," *Journal of Applied Electrochemistry,* vol. 9, pp. 411-426, 1979.

[201] G. M. Haarberg*, et al.*, "Metal deposition from chloride melts: I. Rates of diffusion in solvent melt," *Electrochimica Acta,* vol. 76, pp. 256-261, 2012.

[202] R. V. Kurbatov*, et al.*, "Phase equilibria in M_2O-MgO-B_2O_3 (M = Na, Rb) systems," *Russian Journal of Inorganic Chemistry,* vol. 55, pp. 274-279, 2010.

[203] J. Li*, et al.*, "Preparation of ZrC by self-propagating high-temperature synthesis," *Ceramics International,* vol. 36, pp. 1681-1686, 2010.

[204] A. Chu*, et al.*, "Carbothermal synthesis of ZrC powders using a combustion synthesis precursor," *International Journal of Refractory Metals and Hard Materials,* vol. 36, pp. 204-210, 2013.

[205] D. S. Coleman and P. D. A. Lacy, "The phase equilibrium diagram for the KCl-NaCl system," *Materials Research Bulletin,* vol. 2, pp. 935-938, 1967.

[206] J. J. Thomas*, et al.*, "Kinetics and activation energy of magnesium oxide hydration," *Journal of the American Ceramic Society,* 2013.

[207] M. S. Song*, et al.*, "In situ fabrication of ZrC powder obtained by self-propagating high-temperature synthesis from Al–Zr–C elemental

powders," *International Journal of Refractory Metals and Hard Materials,* vol. 29, pp. 392-396, 2011.

[208] L. Wang, *et al.*, "Solid-state reaction synthesis of ZrC from zirconium oxide at low temperature," *International Journal of Refractory Metals and Hard Materials,* vol. 38, pp. 134-136, 2013.

[209] N. Bertram, *et al.*, "Nanoplatelets made from MoS_2 and WS_2," *Chemical Physics Letters,* vol. 418, pp. 36-39, 2006.

[210] K. S. Novoselov, *et al.*, "Two-dimensional atomic crystals," *Proceedings of the National Academy of Sciences of the United States of America,* vol. 102, pp. 10451-10453, July 26, 2005 2005.

[211] H. Wiśniewska-Weinert, "Exfoliation based technology of large scale manufacturing molybdenum disulphide graphene-like nanoparticle mixtures," *Archives of Civil and Mechanical Engineering,* vol. 13, pp. 144-149, 2013.

[212] H.-P. Huang and J.-J. Zhu, "Preparation of novel carbon-based nanomaterial of graphene and its applications electrochemistry," *Chinese Journal of Analytical Chemistry,* vol. 39, pp. 963-971, 2011.

[213] C. Soldano, *et al.*, "Production, properties and potential of graphene," *Carbon,* vol. 48, pp. 2127-2150, 2010.

[214] Q. Ouyang, *et al.*, "Graphene/MoS_2 organic glasses: Fabrication and enhanced reverse saturable absorption properties," *Optical Materials,* vol. 35, pp. 2352-2356, 2013.

[215] L. Ma, *et al.*, "One-pot hydrothermal synthesis of MoS_2 nanosheets/C hybrid microspheres," *Ceramics International,* vol. 38, pp. 229-234, 2012.

[216] J. Kiss, *et al.*, "Preparation of a boron nitride single layer on a polycrystalline Rh surface," *Applied Surface Science,* vol. 264, pp. 838-844, 2013.

[217] Y. D. Liu, *et al.*, "Preparation, characterization and photoelectrochemical property of ultrathin MoS_2 nanosheets via hydrothermal intercalation and exfoliation route," *Journal of Alloys and Compounds,* vol. 571, pp. 37-42, 2013.

[218] J. Ding, *et al.*, "Novel synthesis and characterization of titanium carbide coatings on graphite flakes," vol. 634-638, ed, 2013, pp. 3052-3055.

[219] X. Li, *et al.*, "Preparation of a titanium carbide coating on carbon fibre using a molten salt method," *Carbon,* vol. 46, pp. 305-309, 2008.

[220] B. H. Lohse, *et al.*, "Raman spectroscopy as a tool to study TiC formation during controlled ball milling," *Journal of Applied Physics,* vol. 97, 2005.

[221] K. Chen and Z. Bao, "Synthesis and characterization of carbide nanosheets by a template-confined reaction," *Journal of Nanoparticle Research,* vol. 14, 2012.

[222] M. V. Klein, *et al.*, "Raman scattering induced by carbon vacancies in TiCx," *Physical Review B,* vol. 17, pp. 1546-1556, 1978.

[223] G. Wen, *et al.*, "Reaction synthesis of TiB_2-TiC composites with enhanced toughness," *Acta Materialia,* vol. 49, pp. 1463-1470, 2001.

[224] X. Zhu, *et al.*, "The equilibrium between metallic titanium and titanium ions in LiCl-KCl melts," *Journal of Alloys and Compounds*.

[225] W. C. Kreye. and H. H. Kellogg, "The Equilibrium Between Titanium Metal,$TiCl_2$, and $TiCl_3$ in NaCl–KCl Melts," *J. Electrochem. Soc.,* vol. 104, p. 5, 1957.

[226] M. E. Straumanis, *et al.*, "The mechanism of deposition of titanium coatings from fused salt baths," *J. Electrochem. Soc.,* vol. 104, p. 4, 1957.

[227] W. Xie, "Molten salt synthesis and characterisation of novel carbide materials," PhD 150, Faculty of Materials Science and Engineering, The University of Sheffield, Sheffield, England, 2011.

[228] S. J. Powell and J. R. G. Evans, "The structure of ceramic foams prepared from polyurethane-ceramic suspensions," *Materials and Manufacturing Processes,* vol. 10, pp. 757-771, 1995.

[229] W. Zhou, *et al.*, "Combustion synthesis of highly porous ceramics: The TiC-Al2O3 system," *Journal of Materials Science,* vol. 34, pp. 4469-4473, 1999.

[230] N. Popovska, *et al.*, "Paper derived biomorphic porous titanium carbide and titanium oxide ceramics produced by chemical vapor infiltration and reaction (CVI-R)," *Journal of the European Ceramic Society,* vol. 25, pp. 829-836, 2005.

[231] W. Xie, *et al.*, "Novel synthesis and characterization of high quality silicon carbide coatings on carbon fibers," *Journal of the American Ceramic Society,* vol. 95, pp. 1878-1882, 2012.

[232] D. D. Brown and D. J. Green, "Investigation of strut crack formation in open cell alumina ceramics," *Journal of the American Ceramic Society,* vol. 77, pp. 1467-1472, 1994.

[233] V. R. Vedula, *et al.*, "Thermal shock resistance of ceramic foams," *Journal of the American Ceramic Society,* vol. 82, pp. 649-656, 1999.

[234] C. J. Engberg and E. H. Zehms, "Thermal expansion of Al_2O_3, BeO, MgO, B_4C and TiC above 1000 °C," *J. Am. Ceram. Soc.,* vol. 42, pp. 301-305, 2006.

[235] G. M. Song, *et al.*, "Mechanical properties of short carbon fiber-reinforced TiC composites produced by hot pressing," *Materials Science and Engineering: A,* vol. 326, pp. 240-248, 2002.

[236] J. Ma, *et al.*, "Synthesis of nanocrystalline titanium carbide with a new convenient route at low temperature and its thermal stability," *Materials Science and Engineering: B,* vol. 153, pp. 96-99, 2008.